Thèse n° 8790

Efficient geometric integrators for the linear and nonlinear time-dependent Schrödinger equation

Présentée le 25 mars 2022

Faculté des sciences de base
Laboratoire de chimie physique théorique
Programme doctoral en chimie et génie chimique

pour l'obtention du grade de Docteur ès Sciences

par

Julien ROULET

Acceptée sur proposition du jury

Prof. T. Rizzo, président du jury
Prof. J. Vanicek, directeur de thèse
Prof. V. Engel, rapporteur
Prof. K. Houfek, rapporteur
Dr S. Bonella, rapporteuse

École
polytechnique
fédérale
de Lausanne

2022

Pour Claudine…

Acknowledgements

This thesis became a reality with many people's valuable help and kind support. I would like to express my deep sense of gratitude to them.

Foremost, I would like to thank my advisor, Prof. Jiří Vaníček, for his guidance, support, patience, and his overwhelming enthusiasm for science. I have learned a lot from him and greatly appreciated working in the LCPT group.

I am grateful to all colleagues I met during my doctoral studies: Aurélien Patoz and Konstantin Karandashev, for their guidance and valuable advice during my Master's project. I thank Seonghoon Choi and Tomislav Begušić, with whom I started the PhD, for their help and the excellent time we spent joking and struggling with programming and science. I am grateful to postdocs Antonio Prlj, Christophe Vaillant, Lipeng Chen, Nikolay Golubev, Sergey Antipov, and Solène Oberli for sharing their scientific knowledge and technical advice. I thank Alan Scheidegger, Eriks Kletnieks, Fabian Kröninger, Roya Moghaddasi Fereidani, and Zhan Tong Zhang for their help in understanding their respective research projects and being amazing colleagues. I would like to thank Sylvie Dentan for always organizing smooth travel to our various conferences and her assistance with all the administrative paperwork.

I am extremely grateful to Leyla Vuong for her kindness, patience, and unconditional love. I thank her for all the amazing moments we shared, travelling, hiking and camping.

Last but not least, I am deeply indebted to my family for their lifelong encouragement: parents Maria and Vincent; siblings Mélina, Thomas, and Kelian; grandparents Jean-Daniel and Claudine.

Lausanne, February 18, 2022 J. R.

Abstract

Many physical and chemical reactions are driven by nonadiabatic processes, which imply the breakdown of the celebrated Born–Oppenheimer approximation. To understand these processes, experimentalists employ spectroscopic techniques. However, the obtained results are difficult to decipher, and accurate molecular quantum dynamics simulations are used to interpret the results.

The second-order split-operator algorithm is one of the most popular numerical methods for simulating the nonadiabatic quantum dynamics because it is explicit, easy to implement, and it preserves many geometric properties of the exact solution. However, the second-order accuracy of this algorithm makes it unaffordable if very accurate results are needed, as tiny time steps are required. To remedy this lack of efficiency, we use composition methods to generate higher-order split-operator algorithms.

Although compositions methods increase the accuracy of the standard split-operator algorithm to arbitrary even orders of convergence, the efficiency of the obtained algorithms is still questioned because the computational cost per time step increases drastically with the order of convergence. Therefore, using one- and three-dimensional models of NaI and pyrazine, respectively, we investigate the convergence, efficiency, and geometric properties of these high-order integrators and find that they are, for accurate simulations, more efficient than the standard split-operator algorithm while still preserving the same geometric properties.

Besides employing these integrators for simulating the nonadiabatic quantum dynamics, we also explore quantum control and, more specifically, local control theory. This technique uses the instantaneous dynamics of the system to compute an electric field, which interacts with the system in order to drive the state in a desired direction. Because the electric field is obtained from the state itself, we demonstrate that this technique translates into a nonlinear time-dependent Schrödinger equation.

Abstract

Although it is geometric and second-order accurate for simple nonlinearities, the standard split-operator algorithm loses its time-reversal symmetry and second-order accuracy when employed for more complicated nonlinear time-dependent Schrödinger equations. One example of the latter is the one appearing in local control theory.

We demonstrate that this lack of generality of the standard split-operator algorithm occurs due to its explicit nature. Thus, we propose two strategies to overcome this issue: First, we completely abandon the split-operator algorithm and present a numerical method based on the implicit midpoint method instead. Second, we make the standard split-operator algorithm implicit, which avoids abandoning the split-operator algorithm altogether. The accuracy and geometric properties of both strategies are then numerically verified using a two-dimensional model of retinal, a molecule whose photochemistry triggers the first event in the biological process of vision. The results demonstrate that both approaches yield second-order methods that preserve all the geometric properties of the exact solution. Because the developed integrators are symmetric, we further improve their accuracy and efficiency using composition methods.

Keywords: nonadiabatic quantum dynamics, geometric integrators, split-operator algorithm, composition methods, quantum control, local control theory, nonlinear time-dependent Schrödinger equation

Résumé

De nombreuses réactions physiques et chimiques sont induites par des processus nonadiabatiques, impliquant la rupture de la célèbre approximation de Born-Oppenheimer. Afin de comprendre ces processus, les expérimentalistes font appel à des techniques spectroscopiques. Puisque les résultats obtenus sont difficiles à déchiffrer, des simulations précises de la dynamique quantique moléculaire sont employées afin d'interpréter ces résultats.

L'algorithme split-operator du second ordre est l'une des méthodes numériques les plus populaires pour simuler la dynamique quantique nonadiabatique. En effet, cet algorithme est explicite, facile à mettre en œuvre et préserve de nombreuses propriétés géométriques de la solution exacte. Cependant, comme il n'est précis qu'au second ordre, il devient rapidement inabordable car des pas de temps minuscules sont nécessaires afin d'obtenir des résultats très précis. Pour remédier à ce manque d'efficacité, nous utilisons des méthodes de composition pour générer des algorithmes split-operator d'ordre supérieur.

Bien que les méthodes de composition améliorent la précision de l'algorithme split-operator jusqu'à des ordres de convergence arbitraires, l'efficacité des algorithmes obtenus est souvent remise en question car le coût de calcul par pas de temps augmente considérablement avec l'ordre de convergence. Par conséquent, en ayant recours à des modèles unidimensionnel de NaI et tridimensionel de la pyrazine, nous étudions la convergence, l'efficacité et les propriétés géométriques de ces intégrateurs d'ordre élevé. D'après les resultats obtenus, nous constatons qu'ils sont, pour des simulations très précises, bien plus efficaces que l'algorithme split-operator standard, et ce, tout en conservant les mêmes propriétés géométriques.

Outre l'utilisation de ces intégrateurs pour simuler la dynamique quantique nonadiabatique, nous explorons également le contrôle quantique et, plus particulièrement, la théorie du contrôle local. Cette technique emploie la dynamique instantanée du système pour produire un champ électrique qui interagit avec le système afin de conduire ce dernier dans une direction souhaitée. Comme le champ électrique est obtenu à partir de l'état lui-même, nous démontrons que cette technique se traduit en une équation de Schrödinger non-linéaire dépendante du temps.

Bien que l'algorithme split-operator standard soit géométrique et précis au second ordre pour les non-linéarités simples, il perd sa symétrie temporelle et sa précision au second ordre lorsqu'il est utilisé pour des équations de Schrödinger non-linéaires plus sophistiquées, comme celle qui apparait dans la théorie du contrôle local.

Nous démontrons que ce manque de généralité de l'algorithme split-operator est dû à sa nature explicite et proposons deux stratégies pour remédier à ce problème. Dans la première approche, nous abandonnons complètement l'algorithme split-operator et présentons à la place une méthode numérique implicite, basée sur la méthode du point médian. Dans la seconde approche, nous rendons l'algorithme split-operator standard implicite, évitant ainsi l'abandon complet de l'algorithme. La précision et les propriétés géométriques des deux stratégies sont ensuite vérifiées numériquement à l'aide d'un modèle bidimensionnel du rétinal, une molécule dont la photochimie déclenche le premier événement du processus biologique de la vision. Les résultats montrent que les deux approches donnent des méthodes de second ordre qui préservent toutes les propriétés géométriques de la solution exacte. Les intégrateurs développés étant symétriques, nous améliorons encore leur précision et leur efficacité en utilisant des méthodes de composition.

Mots-clés : dynamique quantique nonadiabatique, intégrateurs géometriques, méthodes split-operator, méthodes de composition, contrôle quantique, théorie du contrôle local, équation de Schrödinger non-linéaire

Contents

Acknowledgements **i**

Abstract **iii**

List of Figures **xi**

List of Tables **xix**

1 Introduction **1**
- 1.1 The linear time-dependent Schrödinger equation 4
  - 1.1.1 Geometric properties of the exact evolution operator . . . 4
  - 1.1.2 Interaction of a molecule with an electromagnetic field . . 7
  - 1.1.3 Local control theory 8
- 1.2 Numerical methods 9
  - 1.2.1 First-order Euler methods 9
  - 1.2.2 First-order split-operator algorithms 10
  - 1.2.3 Recovery of geometric properties by composed methods . . 10
  - 1.2.4 Adaptation to time-dependent Hamiltonians 11
  - 1.2.5 Dynamic Fourier method 13
- 1.3 Thesis overview 13

2 Efficient high-order integrators for the nonadiabatic dynamics in the diabatic basis **15**
- 2.1 Introduction 16
- 2.2 Theory 18
  - 2.2.1 Symmetric composition schemes for symmetric methods . . 18
  - 2.2.2 Compositions of split-operator algorithms 20
  - 2.2.3 Pruning splitting coefficients 23
  - 2.2.4 Molecular Hamiltonian in the diabatic basis 24

2.2.5 Trapezoidal rule and implicit midpoint method 26
2.3 Numerical examples 27
2.3.1 One-dimensional model of NaI 27
2.3.2 Three-dimensional model of pyrazine 34
2.4 Conclusion 36

3 Geometric high-order integrator for the nonlinear time-dependent Schrödinger equation 39
3.1 Introduction 40
3.2 Nonlinear Schrödinger equation 42
3.2.1 Geometric properties of the exact evolution operator . . . 43
3.2.2 Nonlinear character of local control theory 46
3.3 Geometric integrators for the nonlinear Schrödinger equation . . . 46
3.3.1 Loss of geometric properties by Euler methods 47
3.3.2 Recovery of geometric properties and increasing accuracy by composition 47
3.3.3 Solving the implicit step in a general nonlinear Schrödinger equation 48
3.3.4 Solving the implicit step in local control theory 50
3.3.5 Approximate application of the explicit split-operator algorithm to the nonlinear Schrödinger equation 50
3.4 Numerical examples 52
3.5 Conclusion 61

4 An implicit split-operator algorithm for the nonlinear time-dependent Schrödinger equation 63
4.1 Introduction 63
4.2 Split-operator algorithms for the nonlinear time-dependent Schrödinger equation 64
4.2.1 Recovery of geometric properties and increasing accuracy by composition 64
4.2.2 Solving the implicit propagation 65
4.3 Numerical examples 66
4.4 Conclusion 72

5 Conclusions and outlook 73

A Supporting information for Chapter 2 **77**
A.1 Local error and geometric properties . . . 77
A.1.1 Local error . . . 78
A.1.2 Unitarity, symplecticity, and stability . . . 79
A.1.3 Commutation of the evolution operator with the Hamiltonian and conservation of energy . . . 79
A.1.4 Symmetry and time reversibility . . . 80
A.2 Exponential convergence with grid density . . . 80

B Supporting information for Chapter 3 **83**
B.1 Geometric properties of nonlinear numerical integrators . . . 83
B.1.1 Norm conservation . . . 83
B.1.2 Symmetry and time reversibility . . . 85
B.2 Exponential convergence of the wavefunction with respect to the grid density . . . 86
B.3 Results for the other simulations . . . 88
B.4 Loss of time reversibility due to roundoff errors . . . 96

C The generalized minimal residual method **99**
C.1 Initialization . . . 99
C.2 Arnoldi's method . . . 100
C.3 Forming the solution . . . 100
C.4 Restart . . . 101
C.5 Practical implementation . . . 101

D Supporting information for Chapter 4 **105**
D.1 Geometric properties of various integrators . . . 105
D.1.1 Norm conservation . . . 105
D.1.2 Symmetry and time-reversibility . . . 106
D.2 Results for all the studied methods . . . 107

Bibliography **113**

Curriculum Vitae **123**

List of Figures

2.1 Pictorial representation [104] of the recursive (triple-jump and Suzuki's fractal) and nonrecursive "optimal" composition schemes. 19

2.2 Split-operator algorithms composed by the recursive (triple-jump and Suzuki's fractal) and nonrecursive "optimal" composition schemes shown in Fig. 2.1. In other words, each elementary method $\hat{U}(\gamma_n \Delta t)$ (solid line segment in Fig. 2.1) is replaced by a second-order split-operator algorithm $\hat{U}_{\hat{A}}(\gamma_n \Delta t/2)\hat{U}_{\hat{B}}(\gamma_n \Delta t)\hat{U}_{\hat{A}}(\gamma_n \Delta t/2)$, represented here by a triple of consecutive solid, dotted, and solid line segments. Solid line segments represent $\hat{U}_{\hat{A}}(\gamma_n \Delta t/2)$, whereas the dotted line segments represent $\hat{U}_{\hat{B}}(\gamma_n \Delta t)$. $N_{\hat{O}}$ is the number of actions of $\hat{U}_{\hat{O}}$ on ψ. 21

2.3 Composed split-operator algorithms from Fig. 2.2 after removing zero splitting coefficients and merging adjacent coefficients, i.e., after each two adjacent solid line segments representing $\hat{U}_{\hat{A}}(\gamma_{n+1} \Delta t/2)\hat{U}_{\hat{A}}(\gamma_n \Delta t/2)$ in Fig. 2.2 are merged into a single solid line segment representing $\hat{U}_{\hat{A}}[(\gamma_n + \gamma_{n+1})\Delta t/2]$. 24

2.4 Nonadiabatic dynamics of NaI. Top: Diabatic potential energy surfaces with the initial $[\psi_0^{(2)}(q)]$ and final nuclear wavepacket components $[\psi_{t_f}^{(1)}(q)$ and $\psi_{t_f}^{(2)}(q)]$ in the two diabatic electronic states [the initial ground-state component is not shown because it was zero: $\psi_0^{(1)}(q) = 0$]. Middle: Populations of NaI in the two diabatic states computed with four different second-order methods. Bottom: Populations computed with three different sixth-order compositions of the VTV algorithm. Populations were propagated with a time step $\Delta t = 0.01$ a.u. for the second-order methods and $\Delta t = 82.03125$ a.u. for the sixth-order methods, i.e., much more frequently than the markers suggest. The time step guaranteed wavepacket convergence errors below $\approx 10^{-5}$ in all methods. 28

2.5 Convergence of the molecular wavefunction as a function of the time step. The wavefunction was propagated with the VT algorithm or with the compositions of the VTV algorithm. Gray straight lines indicate various predicted orders of convergence $\mathcal{O}(\Delta t^n)$. Top: all discussed methods, bottom left: methods composed with the triple-jump scheme, bottom right: sixth-order methods. 29

2.6 Convergence error of the phase of the wavepacket as a function of the time step for the triple-jump compositions. Gray straight lines indicate various predicted orders of convergence $\mathcal{O}(\Delta t^n)$. 30

2.7 Efficiency of the VT algorithm and of various compositions of the VTV algorithm shown using the dependence of the convergence error on the CPU time. Top: all methods, bottom left: triple-jump compositions, bottom right: sixth-order methods. The reference wavefunction $\psi_{t_f}^{\mathrm{ref}}$ was chosen as the most accurate point in Fig. 2.5, i.e., the wavefunction obtained using the optimal eighth-order composition with a time step $\Delta t = t_f/2^9$. 31

2.8 Efficiency of the optimal compositions of the trapezoidal rule and of the VTV split-operator algorithm applied to the NaI model. For the trapezoidal rule, only the double precision version of the FFTW3 fast Fourier transform was used, while for the VTV split-operator algorithm, both double and long-double precision versions are compared. The “exact” reference wavefunction $\psi_{t_f}^{\mathrm{ref}}$ is the same as in Fig. 2.7. The result of the elementary second-order trapezoidal rule was extrapolated below the error of $\approx 10^{-7}$ using the line of best fit. As for the fourth-order algorithms, Suzuki’s fractal is considered as the “optimal ”composition scheme. 32

2.9 Conservation of geometric properties by various algorithms: (a) norm, (b) symplectic two-form, (c) molecular energy, and (d)–(e) time reversibility. ϕ_0 is a Gaussian wavepacket with $q_0 = 5.05$ a.u., $p_0 = 2.5$ a.u., and σ_0 identical to that of ψ_0. Time reversibility was measured by the distance of the initial state ψ_0 from a forward-backward propagated state $\tilde{\psi}_0 := \hat{U}(-t)\hat{U}(t)\psi_0$, i.e., the state ψ_0 propagated first forward in time for time t and then backward in time for time t [see Eq. (1.11)]. The NaI model and a time step $\Delta t = t_f/2^7$ a.u. was used in all calculations. 33

2.10 Conservation of molecular energy as a function of the time step in simulations of the nonadiabatic dynamics of NaI. Note that $E_{\Delta t}(t)$ denotes the molecular energy $E_0(t)$ at time t and obtained using a time step Δt. Gray straight lines indicate various orders of convergence $\mathcal{O}(\Delta t^n)$. 34
2.11 Population dynamics of pyrazine obtained using the sixth-order optimal compositions of the trapezoidal rule and VTV algorithm. The same time step $\Delta t = t_f/25600$ was used for both calculations. 35
2.12 Efficiency of the optimal compositions of the trapezoidal rule and VTV split-operator algorithm applied to the three-dimensional pyrazine model. For the trapezoidal rule, only the double precision version of the FFTW3 fast Fourier transform was used, while for the VTV split-operator algorithm, both double and long-double precision versions are compared. As for the fourth-order algorithms, Suzuki's fractal is considered as the "optimal" composition scheme. 36

3.1 Diabatic potential energy surfaces of the model. Orange: Ground electronic state [Eq. (3.34)]. Blue: Excited electronic state [Eq. (3.35)]. 53
3.2 Local control calculations whose goal is increasing either the population $P_2(t)$ of the excited state (left panels, $\lambda = 1.430 \times 10^{-2}$) or the molecular energy $E_0(t)$ (right panels, $\lambda = 1.534 \times 10^{-1}$). As expected, the local control theory applied to these closely related objectives yields very similar results. Top: Excited state population. Middle: Molecular energy. Bottom: Pulse obtained by local control theory. 55
3.3 Convergence of the molecular wavefunction at the final time t_f achieved by the local population control in the presence of nonadiabatic couplings. Top: All studied methods, i.e., explicit and implicit Euler methods, approximate explicit TVT split-operator algorithm, trapezoidal rule, implicit midpoint method and its symmetric compositions. Bottom-left: Methods obtained with the Suzuki composition. Bottom-right: Sixth-order methods obtained with different composition schemes. 56
3.4 Efficiency of the integrators used for the local population control of retinal in the presence of nonadiabatic couplings. Efficiency is measured by plotting the convergence error as a function of the CPU time. Line labels are the same as in Fig. 3.3. 57

3.5 Norm conservation (top) and time reversibility (bottom) of various integrators at the final time t_f as a function of the time step Δt used for the local control of population in the presence of nonadiabatic couplings. Time reversibility is measured by the distance between the initial state ψ_0 and a "forward-backward" propagated state $\tilde{\psi}_0 := \hat{U}(0, t; \psi)\hat{U}(t, 0; \psi)\psi_0$ [see Eq. (3.12)] and line labels are the same as in Fig. 3.3. 59

3.6 Geometric properties of various integrators used for the local population control in the presence of nonadiabatic couplings. Panel (a) shows that only the implicit midpoint and approximate explicit split-operator methods conserve the norm, while panel (b) demonstrates that only the implicit midpoint method and the trapezoidal rule are time-reversible. (Reversibility is measured as in Fig. 3.5). Bottom three panels show that no method conserves (c) the inner product, (d) distance between two states (which would imply stability), or (e) total energy $E_{\text{tot}}(t) := E_0(t) + \langle \hat{\mathbf{V}}_{\text{LCT}}(\psi_t) \rangle_{\psi_t}$ because even the exact evolution operator does not preserve these properties. State ϕ_0 is ψ_0 displaced along the reaction coordinate, i.e., a two-dimensional Gaussian wavepacket of the form (2.16), with parameters $q_0 = (0.1, 0)$, $p_0 = (0, 0)$, and $\sigma_0 = (0.128, 0)$ a.u. The time step $\Delta t = 2^{-2}$ a.u. was used for all calculations and line labels are the same as in Fig. 3.3. Note that only a few points of the Euler methods are visible in some of the plots because the results of the Euler methods leave the range of these plots very rapidly. 60

4.1 Local control simulation whose goal is increasing the molecular energy $E_0(t)$. (a) Molecular energy. (b) Excited state population. (c) Pulse obtained by local control theory. 67

4.2 Convergence of the molecular wavefunction at the final time $t_f = 256$ a.u. achieved by the local energy control. (a) First-order and implicit TVT methods. (b) Methods obtained with the optimal composition (Suzuki's fractal is the optimal fourth-order composition scheme [104]). (c) Sixth-order methods obtained with different composition schemes. 68

4.3 Efficiency of various integrators used for simulating the local energy control of retinal up to the final time $t_f = 256$ a.u. 69

4.4 Time dependence of the geometric properties of the implicit and approximate explicit TVT methods used for simulating the local energy control up to the final time $t_f = 2048$ a.u. (a) Norm of the wavefunction. (b) Time reversibility. (c) Inner product. (d) Distance between two states (conservation of this distance would imply stability). (e) Total energy. Time reversibility is measured by the distance between the initial state ψ_0 and a "forward-backward" propagated state $\tilde{\psi}_0$ [see Fig. 3.5 and Eq. (3.12)]. The state ϕ_0 is the same as the one used in Fig. 3.5 and line labels are the same as in Fig. 4.2. 71

4.5 Norm conservation (a) and time reversibility (b) of various integrators at the final time $t_f = 256$ a.u. as a function of the time step Δt used for the local energy control of retinal. Reversibility is measured as in Fig. 4.4 and line labels are the same as in Fig. 4.2. 72

A.1 Top: Convergence of the initial and final wavepackets with the increasing number of grid points. Bottom: Ratio of the integration error and total convergence error at the final time as a function of the number of grid points. (See Appendix A.2 for details.) The sixth-order optimal composition of the VTV algorithm with time step $\Delta t = t_f/2^7$ was used for the propagation. 81

B.1 Error of the wavefunction at the final time $t_f = 256$ a.u. as a function of the number of grid points. The figure indicates that the numerical grids consisting of $N_1 = 128$ points between $\theta = \pm\pi/2$ a.u. and $N_2 = 64$ points between $q_c = \pm 9.0$ a.u. are converged. All calculations were performed using the approximate explicit TVT split-operator algorithm with time step $\Delta t = 2^{-1}$ a.u. 87

B.2 Error of the wavefunction at the final time $t_f = 2048$ a.u. as a function of the number of grid points. The figure indicates that the numerical grids consisting of $N_1 = 256$ points between $\theta = \pm 3\pi/2$ a.u. and $N_2 = 64$ points between $q_c = \pm 9.0$ a.u. are converged. All calculations were performed using the approximate explicit TVT split-operator algorithm with time step $\Delta t = 2^{-1}$ a.u. 87

B.3 Convergence of the molecular wavefunction at the final time t_f achieved by the local population control in the absence of nonadiabatic couplings. Top: All studied methods, i.e., explicit and implicit Euler methods, approximate explicit TVT split-operator algorithm, trapezoidal rule, implicit midpoint method and its symmetric compositions. Bottom-left: Methods obtained with the Suzuki composition. Bottom-right: Sixth-order methods obtained with different composition schemes. 88

B.4 Same as Fig. B.3, but for energy control with nonadiabatic couplings. 89

B.5 Same as Fig. B.3, but for energy control without nonadiabatic couplings. 89

B.6 Efficiency of the integrators used for the local population control of retinal in the absence of nonadiabatic couplings. Efficiency is measured by plotting the convergence error as a function of the CPU time. 90

B.7 Same as Fig. B.6, but for energy control with nonadiabatic couplings. 90

B.8 Same as Fig. B.6, but for energy control without nonadiabatic couplings. 90

B.9 Norm conservation (top) and time reversibility (bottom) of various integrators at the final time t_f as a function of the time step Δt used for the local population control in the absence of nonadiabatic couplings. Time reversibility is measured by the distance between the initial state ψ_0 and a "forward-backward" propagated state $\tilde{\psi}_0 := \hat{U}(0, t : \psi)\hat{U}(t, 0; \psi)\psi_0$ [Eq. (3.12)]. 91

B.10 Same as Fig B.9, but for energy control in the presence of nonadiabatic couplings. 92

B.11 Same as Fig B.9, but for energy control in the absence of nonadiabatic couplings. 93

B.12 Geometric properties of various integrators used for the local population control in the absence of nonadiabatic couplings. Panel (a) shows that only the implicit midpoint and approximate explicit split-operator methods conserve the norm, while panel (b) demonstrates that only the implicit midpoint method and the trapezoidal rule are time-reversible. (Reversibility is measured as in Fig. B.9). Bottom three panels show that no method conserves (c) the inner product, (d) distance between two states (which would imply stability), or (e) total energy $E_{\mathrm{tot}}(t) := E_0(t) + \langle \hat{\mathbf{V}}_{\mathrm{LCT}}(\psi_t) \rangle_{\psi_t}$ because even the exact evolution operator does not preserve these properties. State ϕ_0 is ψ_0 displaced along the reaction coordinate, i.e., a two-dimensional Gaussian wavepacket of the form (2.16), with parameters $q_0 = (0.1, 0)$, $p_0 = (0, 0)$, and $\sigma_0 = (0.128, 0)$ a.u. The time step $\Delta t = 2^{-2}$ a.u. was used for all calculations and line labels are the same as in Fig. B.3. Note that only a few points of the Euler methods are visible in some of the plots because the results of the Euler methods leave the range of these plots very rapidly. 94
B.13 Same as Fig. B.12, but for energy control with nonadiabatic couplings. 95
B.14 Same as Fig. B.12, but for energy control without nonadiabatic couplings. 96
B.15 Influence of various parameters on the time reversibility of the implicit midpoint method. The three panels show that the time reversibility of the implicit midpoint method deteriorates (a) if the time step Δt is decreased, leading to a faster accumulation of roundoff errors, (b) if the error ε threshold of the nonlinear solver is increased, and (c) if the precision of the floating-point arithmetic is decreased. Note that decreasing the floating-point precision does not have a visible influence on the approximate explicit split-operator algorithm, which is irreversible by construction. Time reversibility is measured as in Fig. B.9. 97

D.1 Convergence of the molecular wavefunction at the final time $t_f = 256$ a.u. achieved by the local energy control. (a) All studied methods, including symmetric compositions of the TVT split-operator algorithm. (b) Methods obtained with the optimal composition (Suzuki's fractal is the optimal fourth-order composition scheme. (c) Sixth-order methods obtained with different composition schemes. 108

D.2 Efficiency of various integrators used for simulating the local energy control of retinal up to the final time $t_f = 256$ a.u. Line labels are the same as in Fig. 4.2. 109

D.3 Time dependence of the geometric properties of the elementary integrators used for simulating the local energy control up to the final time $t_f = 2048$ a.u. (a) Norm of the wavefunction. (b) Time reversibility. (c) Inner product. (d) Distance between two states (which would imply stability). (e) Total energy. Time reversibility is measured by the distance between the initial state ψ_0 and a "forward-backward" propagated state $\tilde{\psi}_0$ [see Fig. 3.5 and Eq. (3.12)]. The state ϕ_0 is the same as the one used in Fig. 3.5 and line labels are the same as in Fig. 4.2. 110

D.4 Norm conservation (a) and time reversibility (b) of various integrators at the final time $t_f = 256$ a.u. as a function of the time step Δt used for the local energy control of retinal. Reversibility is measured as in Fig. D.3 and line labels are the same as in Fig. 4.2. 111

List of Tables

2.1 Geometric properties and computational cost of the first-order and recursively composed second-order split-operator (SO) algorithms. Cost (here before speedup by pruning splitting coefficients) is measured by the number of fast Fourier transforms required per time step (see Sec. 1.2.5). n is the number of recursive compositions and C the total number of composition steps per time step ($C = 3^n$ for the triple jump [121, 122], $C = 5^n$ for Suzuki's fractal [121]). $+$ or $-$ denotes that the geometric property of the exact evolution operator is or is not preserved. 22

2.2 Computational cost and memory requirement of the composed split-operator algorithms before and after pruning (i.e., removing zero coefficients and merging adjacent coefficients) and identifying repeated coefficients. The computational cost is measured by $N_{\hat{A}}+N_{\hat{B}}$, where $N_{\hat{O}}$ is the number of actions of $\hat{U}_{\hat{O}}$ on the wavepacket. The memory requirement before and after pruning is $N_{\hat{A}}+N_{\hat{B}}$, and after identifying repeated coefficients decreases to $N_a^{\mathrm{unq}}+N_b^{\mathrm{unq}}$. 25

1 Introduction

In the Born–Oppenheimer approximation [1, 2], which separates nuclear and electronic motion, independent electronic potential energy surfaces are assumed. However, many important processes in nature [3] can only be described by several coupled Born-Oppenheimer potential energy surfaces [4–7], i.e., by taking into account nonadiabatic effects.

These rapid nonadiabatic processes can be experimentally monitored using pump-probe spectroscopy [8–12], and with the help of new laser technologies, which allows the production of phase and amplitude mediated pulses [13–18], it is possible to not only monitor chemical reactions but also to drive them into a desired outcome [19–21], which we refer to as quantum control. In this vein, several theoretical approaches for the quantum control have been developed. An intuitive way is provided by the pump-dump scheme [22, 23], which employs two time-delayed pulses to guide a wavepacket in a desired reaction channel. The most effective technique for the control is optimal control theory [22, 24–26], which designs a pulse to maximize the overlap between the state at the final time and a selected target state. However, this technique is global in time as it is iterative and requires full forward and backward propagations at each iterative step. Local control theory [25, 27] provides an alternative to the heavy cost associated with optimal control theory. For instance, in local control theory, the control pulse, which drives the system to a desired objective, is designed only from the instantaneous dynamics of the state, and a single propagation is required for achieving the control.

To interpret the results obtained by experimentalists and simulate the quantum control, one needs to solve the time-dependent Schrödinger equation. Various approaches [28] have been developed to solve this equation but they can be separated into two classes. The approximate methods, which rely on semiclassical approximations and the exact methods, which account completely for the quantum nature of the problem. Because the scaling of exact methods increases exponentially with the number of degrees of freedom, they are only applicable to systems with a few degrees of freedom. In contrast, the semiclassical methods can be used to treat systems with numerous degrees of freedom, at the cost of not entirely accounting for the quantum nature of the problem.

To treat high-dimensional systems, several semiclassical methods have been developed, including thawed [29–32] or variational [33, 34] Gaussian approximation, ab initio multiple spawning [35–38] and cloning [39], multiconfigurational Ehrenfest [40, 41], variational multiconfigurational Gaussian [42–44], and methods based on the Herman-Kluk propagator [45, 46]. Note that some of the methods listed above are multi-trajectory and can still be costly because they may require many trajectories to converge. Nevertheless, a nice property of some of these methods is that they need only local potential energy information along the trajectory and thus, are suitable for ab initio dynamics. Indeed, these methods have broad applications, including the description of charge transfer in molecules [47–49] and the computation of absorption spectra [35, 41, 50, 51].

For low-dimensional systems, the starting point is to compute the potential energy surface, i.e., solving the time-independent Schrödinger equation with a suitable electronic structure calculation. Then, before solving the dynamics, the problem is represented in a reduced Hilbert space. Several approaches [28, 52] use a time-independent basis composed of localized pseudospectral or delocalized spectral functions, which reduces into a grid and a matrix representation of the wavefunction and the Hamiltonian, respectively. However, some of these techniques, such as the discrete variable representation [53, 54], require constructing the Hamiltonian, a significant task. Other approaches, such as the multiconfigurational time-dependent Hartree method [55–57], which expands the state using orthogonal time-dependent basis functions, rely on the fact that only a small fraction of the tensor-product Hilbert space is typically accessible during the time of interest. This method has been applied to describe a large variety of problems, including photodissociation [58–60], photoabsorption spectra [61–63], and charge separation in organic photovoltaics [64–66].

However, there are systems in which the full Hilbert space is accessible, and then full grid or time-independent basis sets are preferable. Thus, the dynamic Fourier method [67–69] is an alternative that can access the full Hilbert space, preventing the construction of the Hamiltonian. Similar to the discrete variable representation, this method represents the wavefunction on a grid but only computes the action of the Hamiltonian on the wavefunction. Assuming that the Hamiltonian can be separated into a sum of a term depending only on the nuclear momenta and a term depending only on the nuclear coordinates, the action of each of these terms is obtained by pointwise multiplication in the space in which it is diagonal. The wavefunction representation is then switched between momentum and coordinate space by Fourier transformation.

After space discretization, a suitable numerical method, approximating the exact evolution operator, should be used to propagate the wavefunction. Again, various approaches already exist [70, 71], ranging from finite difference methods, such as the Euler and the second-order differencing methods [68, 71, 72], to polynomial approaches, such as the short iterative Lanczos algorithm [73–75] and Chebyshev method [76]. Another technique, called the split-operator method [67], separates the terms contained in the Hamiltonian and computes their respective exact evolution operator in the representation in which they are diagonal. Next, employing the dynamic Fourier method [67–69], each exact evolution operator propagates the wavefunction separately in the correct representation. Due to its ease of implementation, many important applications have made use of the split-operator algorithm. For example, it has been employed for the description of dissociation of molecules at metal surfaces [77–79], photoionization [80–82] and photodissociation [83–85] processes, as well as various pump-probe spectroscopy experiments [3, 86, 87].

However, the standard versions of the numerical methods mentioned above preserve only some of the geometric properties of the time-dependent Schrödinger equation [88, 89]. Nevertheless, the preservation of these invariants can be important in some situations, and accuracy should not be the only criteria for choosing a propagation method. Therefore, this thesis will focus on geometric integrators [88], which are numerical methods that preserve the geometric properties of the differential equation, such as time-reversal symmetry, symplectic structure, norm, inner product, energy, and stability. The geometric integrators acknowledge that the time-dependent Schrödinger equation is not any general differential equation but is special, and their usage can be likened to using a well-fitting screwdriver instead of a hammer to attach a screw.

Overall, the aim of this thesis is to investigate the accuracy, efficiency, and geometric properties of integrators employed for simulating the nonadiabatic dynamics and its local control in low-dimensional systems. In the context of nonadiabatic dynamics, we present efficient integrators to solve the linear time-dependent Schrödinger equation, whereas for local control theory, we demonstrate later that this technique implies nonlinearity, thus presenting efficient geometric integrators for solving the general nonlinear time-dependent Schrödinger equation.

In this introductory Chapter, we introduce the linear time-dependent Schrödinger equation and define the geometric properties conserved by its exact evolution operator. Next, we describe how light-matter interactions can be considered and present local control theory. After this, we present some standard numerical methods employed to solve the linear time-dependent Schrödinger equation. Finally, a brief overview of the thesis is provided at the end of this Chapter.

1.1 The linear time-dependent Schrödinger equation

The central object of the first part of this thesis is the *linear time-dependent Schrödinger equation*

$$i\hbar\frac{d}{dt}|\psi_t\rangle = \hat{H}_0|\psi_t\rangle, \tag{1.1}$$

which describes the time evolution of the molecular state ψ_t at time t under the influence of a linear time-independent Hamiltonian $\hat{H}_0$.

1.1.1 Geometric properties of the exact evolution operator

With the initial condition ψ_0, the formal solution of Eq. (1.1) is

$$|\psi_t\rangle = \hat{U}(t)|\psi_0\rangle, \qquad t \geq 0, \tag{1.2}$$

where the exact evolution operator $\hat{U}$ is given by

$$\hat{U}(t) := \hat{U}_{\hat{H}_0}(t) \tag{1.3}$$

with $\hat{U}_{\hat{A}}(t) := e^{-i\hat{A}t/\hbar}$ denoting an evolution operator associated with a Hermitian operator $\hat{A}$ and time t. The exact evolution operator possesses many geometric properties. Indeed, it is linear, unitary, symmetric, time-reversible, stable, symplectic, and conserves the norm, energy, and inner product. Because these geometric properties are also desirable when approximating the exact evolution operator with a numerical method, it is relevant to define them clearly.

An evolution operator $\hat{U}$ is said to *preserve the norm* $\|\cdot\| := \langle\cdot|\cdot\rangle^{1/2}$ if

$$\|\hat{U}\psi_t\| = \|\psi_t\| \tag{1.4}$$

for all ψ_t and *preserve the inner product* $\langle\cdot|\cdot\rangle$ if

$$\langle\hat{U}\psi_t|\hat{U}\phi_t\rangle = \langle\psi_t|\hat{U}^\dagger\hat{U}\phi_t\rangle = \langle\psi_t|\phi_t\rangle \tag{1.5}$$

for all ψ_t and ϕ_t, with $\hat{U}^\dagger$ denoting the Hermitian conjugate of $\hat{U}$. For linear operators, these two properties are equivalent because norm conservation implies conservation of the inner product. In contrast, for general, and possibly nonlinear, operators, norm preservation implies neither linearity nor preservation of the inner product [90]. The condition for conservation of the inner product is equivalent to the condition that $\hat{U}^\dagger\hat{U}$ be the identity operator, i.e.,

$$\hat{U}^\dagger = \hat{U}^{-1}, \tag{1.6}$$

for which the evolution operator $\hat{U}$ is said to be *unitary*. Since the Hamiltonian is Hermitian, i.e., $\hat{H}_0^\dagger = \hat{H}_0$, the exact evolution operator (1.3) is unitary due to $\hat{U}(t)^\dagger = e^{i\hat{H}_0^\dagger t/\hbar} = e^{i\hat{H}_0 t/\hbar} = \hat{U}(t)^{-1}$, and consequently, conserves the norm and the inner product.

An operator $\hat{U}$ is said to be *symplectic* if

$$\omega(\hat{U}\psi_t, \hat{U}\phi_t) = \omega(\psi_t, \phi_t), \tag{1.7}$$

where $\omega(\psi, \phi)$ denotes the symplectic two-form, which is a nondegenerate skewsymmetric bilinear form on the Hilbert space. In quantum mechanics, a symplectic two-form can be defined as [89]

$$\omega(\psi, \phi) := -2\hbar \, \mathrm{Im}\langle \psi | \phi \rangle, \tag{1.8}$$

and is naturally conserved if the inner product is. The exact evolution operator (1.3) is therefore symplectic.

An evolution operator $\hat{U}$ is said to *preserve the energy* if $E_0(t) := \langle \hat{H}_0 \rangle_{\hat{U}\psi_t} = \langle \hat{H}_0 \rangle_{\psi_t} = E_0(0)$, where $\langle \hat{A} \rangle_\psi := \langle \psi | \hat{A} | \psi \rangle$ denotes the expectation value of operator $\hat{A}$ in state ψ. This property holds if the evolution operator is unitary and commutes with the Hamiltonian, i.e.,

$$\begin{aligned} \langle \hat{H}_0 \rangle_{\hat{U}\psi_t} &= \langle \hat{U}\psi_t | \hat{H}_0 | \hat{U}\psi_t \rangle \\ &= \langle \psi_t | \hat{U}^\dagger \hat{H}_0 \hat{U} | \psi_t \rangle \\ &= \langle \psi_t | \hat{U}^\dagger \hat{U} \hat{H}_0 | \psi_t \rangle \\ &= \langle \psi_t | \hat{H}_0 | \psi_t \rangle \\ &= \langle \hat{H}_0 \rangle_{\psi_t}. \end{aligned} \tag{1.9}$$

The exact evolution operator (1.3) conserves the energy because it is unitary and commutes with the Hamiltonian since it can be Taylor expanded into powers of $\hat{H}_0$.

An evolution operator $\hat{U}(t)$ is said to be *symmetric* [88, 91] if

$$\hat{U}(t)^* = \hat{U}(t), \tag{1.10}$$

where $\hat{U}(t)^* := \hat{U}(-t)^{-1}$ denotes the adjoint of operator $\hat{U}(t)$. A direct consequence of symmetry is time reversibility, i.e., forward propagation of a state ψ_0 from time 0 to time t, followed by backward propagation from time t to time 0, yields ψ_0 again. Indeed, any symmetric evolution operator $\hat{U}(t)$ is also time-reversible due to

$$\hat{U}(-t)\hat{U}(t)\psi_0 = \hat{U}(-t)\hat{U}(t)^*\psi_0 = \hat{U}(-t)\hat{U}(-t)^{-1}\psi_0 = \psi_0. \tag{1.11}$$

The exact evolution operator (1.3) is symmetric and time-reversible because $\hat{U}(t)^* = e^{-i\hat{H}_0 t/\hbar} = \hat{U}(t)$.

Finally, an evolution operator $\hat{U}(t)$ is said to be *stable* [91–93] if for every $\epsilon > 0$, there exist $\delta(\epsilon) > 0$ such that

$$\|\psi_0 - \phi_0\| < \delta \text{ implies } \|\hat{U}(t)\psi_0 - \hat{U}(t)\phi_0\| < \epsilon \text{ for all } t. \tag{1.12}$$

It is said to be *attracting* [92, 93] if there exists a $\delta > 0$ such that

$$\|\psi_0 - \phi_0\| < \delta \text{ implies } \|\hat{U}(t)\psi_0 - \hat{U}(t)\phi_0\| \to 0 \text{ as } t \to \infty. \tag{1.13}$$

It is said to be *asymptotically stable* if it is both stable and attracting. Due to norm conservation, the exact evolution operator (1.3) is stable but not asymptotically stable because

$$\|\hat{U}(t)\psi_0 - \hat{U}(t)\phi_0\| = \|\psi_0 - \phi_0\|. \tag{1.14}$$

1.1.2 Interaction of a molecule with an electromagnetic field

The interaction of a molecule with an explicit laser field $\vec{E}(t)$ is described by the linear time-dependent Schrödinger equation

$$i\hbar \frac{d}{dt}|\psi_t\rangle = \hat{H}(t)|\psi_t\rangle, \tag{1.15}$$

where the time-dependent Hamiltonian

$$\hat{H}(t) := \hat{H}_0 + \hat{V}_{\text{int}}(t) \tag{1.16}$$

is composed of the molecular Hamiltonian $\hat{H}_0$ and a time-dependent interaction potential $\hat{V}_{\text{int}}(t)$. Within the electric-dipole approximation [94], the interaction potential is given by

$$\hat{V}_{\text{int}}(t) := -\vec{\mu}(\hat{q}) \cdot \vec{E}(t), \tag{1.17}$$

where the vector function $\vec{\mu}(\hat{q})$ of the position operator $\hat{q}$ denotes the electric dipole operator of the system. Direct integration of Eq. (1.15) with the initial condition ψ_{t_0} leads to the formal solution $|\psi_t\rangle = \hat{U}(t, t_0)|\psi_{t_0}\rangle$ with the exact evolution operator given by the time-ordered exponential

$$\hat{U}(t,t_0) := \mathcal{T}\exp\left[-\frac{i}{\hbar}\int_{t_0}^{t} dt'\hat{H}(t')\right], \tag{1.18}$$

where $\mathcal{T}$ denotes the time-ordering operator. Similarly to the evolution operator (1.3), this evolution operator has many important geometric properties: it is linear, unitary, symplectic, symmetric, time-reversible, and stable [88–91]. Because it is unitary, the evolution operator (1.18) conserves the norm as well as the inner product and symplectic structure [90]. However, since the Hamiltonian is time-dependent, the Schrödinger equation (1.15) is a nonautonomous differential equation [88], and consequently, the evolution operator (1.18) does not conserve energy.

1.1.3 Local control theory

Contrary to Eq. (1.17), the electric field used in local control theory [25, 27], called control field and denoted by $\vec{E}_{\mathrm{LCT}}(t)$, is not known explicitly as a function of time. Instead, it is chosen "on the fly" according to the current state ψ_t of the system, in order to increase or decrease the expectation value $\langle\hat{O}\rangle_{\psi_t}$ of a chosen operator $\hat{O}$. More precisely, the control field is computed so that the time derivative of the expectation value,

$$\frac{d\langle\hat{O}\rangle_{\psi_t}}{dt} = \frac{i}{\hbar}\langle[\hat{H}(t),\hat{O}]\rangle_{\psi_t} = \frac{i}{\hbar}\left\{\langle[\hat{H}_0,\hat{O}]\rangle_{\psi_t} - \vec{E}_{\mathrm{LCT}}(t)\cdot\langle[\hat{\vec{\mu}},\hat{O}]\rangle_{\psi_t}\right\}, \tag{1.19}$$

remains [25, 27] positive or negative at all times. If the operator $\hat{O}$ commutes with the system's Hamiltonian $\hat{H}_0$, this goal is achieved by using the field

$$\vec{E}_{\mathrm{LCT}}(t) := \pm\lambda i\langle[\hat{\vec{\mu}},\hat{O}]\rangle^{*}_{\psi_t} = \mp\lambda i\langle[\hat{\vec{\mu}},\hat{O}]\rangle_{\psi_t}, \tag{1.20}$$

where $\lambda > 0$ is a parameter which scales the intensity of the control field and the sign in Eq. (1.20) is chosen according to whether one wants to increase (+) or decrease (−) $\langle\hat{O}\rangle_{\psi_t}$. This claim is proven by inserting the definition (1.20) of $\vec{E}_{\mathrm{LCT}}(t)$ into Eq. (1.19), which yields

$$\frac{d\langle\hat{O}\rangle_{\psi_t}}{dt} = \frac{i}{\hbar}\langle[\hat{H}_0,\hat{O}]\rangle_{\psi_t} \pm \frac{\lambda}{\hbar}\|\langle[\hat{\vec{\mu}},\hat{O}]\rangle_{\psi_t}\|^2 \tag{1.21}$$

for the derivative of the expectation value. This equation confirms that a strictly increasing or strictly decreasing evolution of $\langle \hat{O} \rangle_{\psi_t}$ is guaranteed only if $[\hat{H}_0, \hat{O}] = 0$ [95, 96], largely reducing the choice of operators $\hat{O}$ whose expectation values we can control monotonically. Despite this restriction, local control theory has been successfully used to control various processes such as energy and population transfer [25, 27, 97, 98], dissociation and association dynamics [96, 99–101] direction of rotation in molecular rotors [102], and electron transfer [103].

1.2 Numerical methods

To propagate the state, a numerical method is employed. The basic idea is to decompose the full evolution operator into a number of small time steps Δt. Then, the state $\psi_{t+\Delta t}$ at time $t + \Delta t$ is obtained from the state ψ_t at time t using the relation

$$\psi_{t+\Delta t} = \hat{U}_{\mathrm{appr}}(\Delta t)\psi_t,$$

where $\hat{U}_{\mathrm{appr}}(\Delta t)$ is an approximate evolution operator. By construction, all consistent propagation methods converge to the exact solution in the limit $\Delta t \to 0$.

1.2.1 First-order Euler methods

The simplest methods are the explicit and implicit Euler methods [89, 91] which approximate the exact evolution operator, respectively, as

$$\hat{U}_{\mathrm{expl}}(\Delta t) := 1 - \frac{i}{\hbar}\hat{H}_0 \Delta t, \tag{1.22}$$

and

$$\hat{U}_{\mathrm{impl}}(\Delta t) := \left[1 + \frac{i}{\hbar}\hat{H}_0 \Delta t\right]^{-1}. \tag{1.23}$$

Both methods are only first-order in the time step and, therefore, very inefficient. Moreover, both Euler methods lose the exact evolution operator's norm conservation, symmetry, time reversibility, symplectic structure, and unitarity [104]. Even though they commute with the Hamiltonian, neither method preserves the energy due to their lack of unitarity. Worst still, the explicit Euler method is unstable, whereas the implicit Euler method is asymptotically stable. Nevertheless, they are applicable to both separable and nonseparable Hamiltonian operators.

1.2.2 First-order split-operator algorithms

Until now, we considered general Hamiltonian operators $\hat{H}_0 \equiv H_0(\hat{q}, \hat{p})$, which can be either separable or nonseparable. For split-operator algorithms, we require the Hamiltonian to be separable as

$$\hat{H}_0 = \hat{T} + \hat{V}_0 \equiv T(\hat{p}) + V_0(\hat{q}) \tag{1.24}$$

into a sum of kinetic $\hat{T}$ and potential $\hat{V}_0$ energies, which depend, respectively, only on the momentum $\hat{p}$ and position $\hat{q}$ operators.

Depending on the order of kinetic and potential propagations, the approximate evolution operator is [67, 105]

$$\hat{U}_{\mathrm{TV}}(\Delta t) := \hat{U}_{\hat{T}}(\Delta t)\hat{U}_{\hat{V}_0}(\Delta t) \tag{1.25}$$

in the TV split-operator algorithm and

$$\hat{U}_{\mathrm{VT}}(\Delta t) := \hat{U}_{\hat{V}_0}(\Delta t)\hat{U}_{\hat{T}}(\Delta t) \tag{1.26}$$

in the VT split-operator algorithm. Both $\hat{U}_{\mathrm{TV}}$ and $\hat{U}_{\mathrm{VT}}$ are unitary, symplectic, stable, but only first-order in the time step Δt. Neither method conserves energy because neither evolution operator commutes with the Hamiltonian. Moreover, neither method is symmetric nor time-reversible. These properties are justified in Appendix A and summarized in Table 2.1.

1.2.3 Recovery of geometric properties by composed methods

None of the Euler methods (1.22)–(1.23) are symmetric nor time-reversible. Indeed, they are adjoints of each other, and hence, time-irreversible [104]. Nevertheless, composing two adjoint methods together, each with a time step $\Delta t/2$, yields a second-order accurate symmetric method [89]. Employing such a composition with the implicit and explicit Euler methods yields, depending on the order of composition, either the implicit midpoint method

$$\hat{U}_{\mathrm{mid}}(\Delta t) := \hat{U}_{\mathrm{expl}}(\Delta t/2)\hat{U}_{\mathrm{impl}}(\Delta t/2) \tag{1.27}$$

or the trapezoidal rule [106, 107] (or Crank–Nicolson method)

$$\hat{U}_{\mathrm{trap}}(\Delta t) := \hat{U}_{\mathrm{impl}}(\Delta t/2)\hat{U}_{\mathrm{expl}}(\Delta t/2). \tag{1.28}$$

Both methods are second-order accurate, norm- and energy-preserving, stable, symmetric, and time-reversible regardless of the size of the time step [88, 104]. However, note that the geometric properties of the implicit midpoint and the trapezoidal rule are only preserved if the implicit step (1.23) is solved exactly (or in practice to machine accuracy). In this thesis, we solve this linear system of equations using the generalized minimal residual algorithm [108–110] (see Appendix C for a detailed presentation of this algorithm).

Similarly, because they are also adjoints of each other, the time-irreversible first-order split-operator algorithms (1.25)–(1.26) can be composed together to obtain a symmetric second-order method. Depending on the order of composition, one obtains [111] either the VTV algorithm

$$\hat{U}_{\mathrm{VTV}}(\Delta t) := \hat{U}_{\mathrm{VT}}(\Delta t/2)\hat{U}_{\mathrm{TV}}(\Delta t/2), \tag{1.29}$$

or TVT algorithm

$$\hat{U}_{\mathrm{TVT}}(\Delta t) := \hat{U}_{\mathrm{TV}}(\Delta t/2)\hat{U}_{\mathrm{VT}}(\Delta t/2). \tag{1.30}$$

Both are explicit, unitary, symplectic, stable, symmetric, and time-reversible, regardless of the size of the time step. In contrary to the second-order integrator based on the Euler methods [Eqs. (1.27)–(1.28)], neither the TVT nor VTV split-operator algorithms commute with the Hamiltonian and, therefore, neither method conserves the energy exactly (see Table 2.1 and Appendix A for a summary and the proofs of these geometric properties).

1.2.4 Adaptation to time-dependent Hamiltonians

The first-order explicit and implicit Euler methods can be extended to solve the linear time-dependent Schrödinger equation with time-dependent Hamiltonian (1.15). Indeed, by acknowledging the time dependence of the Hamiltonian, the explicit

(1.22) and implicit (1.23) Euler methods are modified, respectively, as

$$\hat{U}_{\text{expl}}(t+\Delta t, t) := 1 - \frac{i}{\hbar}\hat{H}(t)\Delta t, \tag{1.31}$$

and

$$\hat{U}_{\text{impl}}(t+\Delta t, t) := \left[1 + \frac{i}{\hbar}\hat{H}(t+\Delta t)\Delta t\right]^{-1}. \tag{1.32}$$

Moreover, following the procedure described in Sec. 1.2.3, the Euler methods (1.31)–(1.32) can be composed together to obtain second-order accurate modified versions of the implicit midpoint method

$$\hat{U}_{\text{mid}}(t+\Delta t, t) := \hat{U}_{\text{expl}}(t+\Delta t, t+\Delta t/2)\hat{U}_{\text{impl}}(t+\Delta t/2, t) \tag{1.33}$$

and the trapezoidal rule

$$\hat{U}_{\text{trap}}(t+\Delta t, t) := \hat{U}_{\text{impl}}(t+\Delta t, t+\Delta t/2)\hat{U}_{\text{expl}}(t+\Delta t/2, t). \tag{1.34}$$

Although the trapezoidal rule conserves the norm of a state evolved with a time-independent linear Hamiltonian, it loses this property when the Hamiltonian is time-dependent or nonlinear [104] (which results in an implicit time dependence). In contrast, the implicit midpoint method preserves all the geometric properties of the exact evolution operator (1.18).

Similarly, assuming that the Hamiltonian be separable as $\hat{H}(t) = \hat{T} + \hat{V}_{\text{tot}}(t)$, where $\hat{V}_{\text{tot}}(t) := \hat{V}_0 + \hat{V}_{\text{int}}(t)$ denotes the sum of the potential energy and the interaction potential operators, the first-order split-operator methods can be adapted for time-dependent Hamiltonians as

$$\hat{U}_{\text{TV}}(t+\Delta t, t) := \hat{U}_{\hat{T}}(\Delta t)\hat{U}_{\hat{V}_{\text{tot}}(t)}(\Delta t) \tag{1.35}$$

in the TV split-operator algorithm and as

$$\hat{U}_{\text{VT}}(t+\Delta t, t) := \hat{U}_{\hat{V}_{\text{tot}}(t+\Delta t)}(\Delta t)\hat{U}_{\hat{T}}(\Delta t) \tag{1.36}$$

in the VT split-operator algorithm. The composition of these two adjoint methods leads to modified versions of the VTV

$$\hat{U}_{\text{VTV}}(t+\Delta t, t) := \hat{U}_{\text{VT}}(t+\Delta t, t+\Delta t/2)\hat{U}_{\text{TV}}(t+\Delta t/2, t), \tag{1.37}$$

and TVT

$$\hat{U}_{\mathrm{TVT}}(t+\Delta t,t) := \hat{U}_{\mathrm{TV}}(t+\Delta t,t+\Delta t/2)\hat{U}_{\mathrm{VT}}(t+\Delta t/2,t) \tag{1.38}$$

split-operator algorithms, which are both second-order accurate, geometric, and explicit.

1.2.5 Dynamic Fourier method

To employ the numerical methods presented above, an efficient method for computing $f(\hat{x})\psi_t$, where $f(\hat{x})$ is an arbitrary function of $\hat{x}$ and $\hat{x}$ denotes either the momentum $\hat{p}$ or position $\hat{q}$ operators, is needed. In the dynamic Fourier method [28, 67–69], each action of $f(\hat{x})$ in the state ψ_t is performed in the x-representation, in which $\hat{x}$ is a diagonal operator. Therefore, the representation of ψ_t is changed, as needed, using a Fourier transform, and a simple pointwise multiplication yields the action.

1.3 Thesis overview

We have seen that the exact solution of the linear time-dependent Schrödinger equation (1.1) conserves many geometric properties. However, these geometric properties are usually not preserved by first-order approximate methods. In this regard, we showed that we could obtain second-order implicit methods, preserving all the geometric properties of the exact solution, by composing the first-order explicit and implicit Euler methods together. Similarly, second-order accurate splitting techniques are obtained by composing the two first-order split-operator algorithms. In contrast to the algorithms based on the Euler methods, these second-order split-operator algorithms are only applicable to separable Hamiltonians and do not preserve the energy exactly. However, because the splitting techniques are explicit, they are much more efficient than the algorithms based on the Euler methods.

Since the split-operator algorithms only have a second-order accuracy, using these methods to obtain highly accurate results would be costly. Chapter 2 addresses this issue by employing composition methods to obtain higher-order split-operator integrators which possess the same geometric properties as the original second-order algorithm.

In Chapter 3, we focus on the nonlinear time-dependent Schrödinger equation which appears, as we will demonstrate in that chapter, in local control theory. Additionally, we show that, although the standard split-operator is geometric and second-order accurate for some examples of nonlinear Schrödinger equations, it is not geometric and loses its second-order accuracy in the general case. To remedy this lack of generality, we abandon the split-operator algorithm and present second-order geometric integrators based on the implicit midpoint method for solving general nonlinear time-dependent Schrödinger equations.

Subsequently, Chapter 4 demonstrates that the split-operator algorithm does not need to be abandoned altogether, but only its explicit nature. Therefore, we propose an implicit version of the split-operator algorithm that is geometric and applies to the general nonlinear time-dependent Schrödinger equation.

Finally, Chapter 5 summarizes the main results of the thesis and proposes valuable applications of the developed numerical integrators.

2 Efficient high-order integrators for the nonadiabatic dynamics in the diabatic basis

We have seen in Chapter 1 that the exact nonadiabatic quantum evolution preserves many geometric properties of the molecular Hilbert space. In Ref. [104], numerical integrators of arbitrary-order of accuracy based on the implicit midpoint method (1.27) and the trapezoidal rule (1.28) were developed. These integrators preserve all the geometric properties exactly even in the adiabatic representation, in which the molecular Hamiltonian is not separable into kinetic and potential terms. Here, we focus on the separable Hamiltonian in diabatic representation, where the split-operator algorithm provides a popular alternative because it is explicit and easy to implement, while preserving most geometric invariants. Whereas the standard version has only second-order accuracy, we implemented, in an automated fashion, its recursive symmetric compositions, using the composition methods employed in Ref. [104], and obtained integrators of arbitrary even order that still preserve the geometric properties exactly. Because the automatically generated splitting coefficients are redundant, we reduce the computational cost by pruning these coefficients and lower memory requirements by identifying unique coefficients. The order of convergence and preservation of geometric properties are justified analytically and confirmed numerically on a one-dimensional two-surface model of NaI and a three-dimensional three-surface model of pyrazine. As for efficiency, we find that to reach a convergence error of 10^{-10}, a 600-fold speedup in the case of NaI and a 900-fold speedup in the case of pyrazine are obtained with the higher-order compositions instead of the second-order split-operator algorithm. Additionally, the pyrazine results suggest that the efficiency gain survives in higher dimensions.

The content of this Chapter has been adapted from Ref. [112]. I acknowledge Seonghoon Choi for his help with the code implementation and calculations.

2.1 Introduction

The molecular Hamiltonian used in nonadiabatic simulations is obtained from ab initio electronic structure methods, which typically yield adiabatic potential energy surfaces. However, in the regions of conical intersections [113, 114], the Born-Oppenheimer surfaces, which are nonadiabatically coupled via momentum couplings, become degenerate and the nonadiabatic couplings diverge. To avoid associated problems, it is convenient to use the diabatic representation, in which the divergent momentum couplings are replaced with well-behaved coordinate couplings.

Although exact diabatization is only possible in systems with two electronic states and one nuclear degree of freedom [115], there exist more general, approximate diabatization procedures [116–118], starting with the vibronic coupling Hamiltonian model [119]. Another benefit of the diabatic representation is that it separates the Hamiltonian into a sum of kinetic energy, depending only on nuclear momenta, and potential energy, depending only on nuclear coordinates, which makes it possible to propagate the molecular wavefunction with the split-operator algorithms. The split-operator algorithms are explicit, easy to implement, and, in addition, they are geometric [88, 91] because they conserve exactly many invariants of the exact solution, regardless of the convergence error of the wavefunction itself.

Indeed, the standard, second-order split-operator algorithms (1.29)–(1.30) are unitary, symplectic, stable, symmetric, and time-reversible, regardless of the size of the time step. However, to obtain highly accurate results, the standard algorithms require using a small time step, because they have only second-order accuracy. There exist much more efficient algorithms, such as the short-iterative Lanczos algorithm [73–75], which has an exponential convergence with respect to the time step, and also conserves the norm and energy, but not the inner product (because it is nonlinear) and other geometric properties.

To address the low accuracy of the second-order split-operator algorithms and the nonconservation of geometric properties by other more accurate methods, various higher-order split-operator integrators have been introduced [120–123], some of which allow complex time steps [123–125] or commutators of the kinetic and potential energies in the exponent [126–128], thus reducing the number of splitting steps. Here we explore one type of higher-order integrators, designed for nonadiabatic dynamics in the diabatic basis, which we have implemented using the recursive triple-jump [121, 122] and Suzuki's fractal [121], as well as several non-recursive, "optimal" compositions of the second-order split-operator algorithm. While the recursive compositions permit an automated generation of integrators of arbitrary even order in the time step [88, 91, 121, 122, 129, 130], the efficiency of higher-order algorithms is sometimes questioned because the number of splitting steps grows exponentially with the order of accuracy, and, consequently, so does the computational cost of a single time step. Motivated by this dilemma, we have explored the convergence and efficiency of the higher-order compositions using a one- and three-dimensional systems, concluding that, despite the increasing number of splittings, the higher-order methods become the most efficient if higher accuracy of the solution is required, and that this gain in efficiency survives in higher dimensions. We have also confirmed that all composed methods are unitary, symplectic, stable, symmetric, and time-reversible. A final benefit of the higher-order methods is the simple, abstract, and general implementation of the compositions of the second-order split-operator algorithm; indeed, even this "elementary" method is, as we have seen in Sec. 1.2.3, a composition of the simpler, first-order algorithms (1.25)–(1.26).

One of the only challenges of implementing the split-operator algorithm for nonadiabatic dynamics in the diabatic representation is the exponentiation of the potential energy operator, which is nondiagonal in the electronic degrees of freedom (in contrast to the diagonal kinetic energy operator). We, therefore, explored several methods for the exponentiation of nondiagonal matrices.

The main disadvantage of the split-operator algorithm and its compositions is that their use is, unlike the integrators based on the implicit midpoint method (1.27) and the trapezoidal rule (1.28) developed in Ref. [104], restricted to separable Hamiltonians. To compare them with the integrators from Ref. [104], we cannot use the adiabatic representation, but instead must perform the comparison in the diabatic representation, where the compositions of the explicit split-operator algorithm are, as expected, much more efficient than the more generally applicable compositions [104] of the implicit midpoint method and the trapezoidal rule. Nevertheless, the comparison confirms that, in contrast to the split-operator compositions, the integrators from Ref. [104] conserve also the energy exactly.

The remainder of this Chapter is organized as follows: In Sec. 2.2, we present the symmetric composition methods and describe several strategies for reducing the computational cost and memory requirements by pruning redundant splitting coefficients generated automatically by the symmetric compositions. After briefly discussing the molecular Hamiltonian in diabatic representation, we analyze, in Sec. 2.3, the convergence properties and the conservation of geometric invariants of various methods using a diabatic one-dimensional two-surface model [131] of NaI and a diabatic three-dimensional three-surface model [132] of pyrazine. Section 2.4 concludes this Chapter.

2.2 Theory

2.2.1 Symmetric composition schemes for symmetric methods

Composing any symmetric second-order method (such as those presented in Sec. 1.2.3) with appropriately chosen time steps leads to integrators of arbitrary even order of accuracy [88, 91, 121, 122]. More precisely, there are a natural number M and real numbers γ_n, $n = 1, \ldots, M$, called composition coefficients, such that for any symmetric evolution operator $\hat{U}_{2p}(\Delta t)$ of even order $2p$, composing this symmetric evolution operator with coefficients γ_n yields a symmetric integrator of order $2p + 2$:

$$\hat{U}_{2p+2}(\Delta t) := \hat{U}_{2p}(\gamma_M \Delta t) \cdots \hat{U}_{2p}(\gamma_1 \Delta t). \tag{2.1}$$

The choice of the composition coefficients must satisfy several relations to increase the order of convergence. Indeed, the composition (2.1) must be consistent in order to allow convergence, which is ensured if the composition coefficients satisfy the relation [133]

$$\sum_{n=1}^{M} \gamma_n = 1. \tag{2.2}$$

By acknowledging that the original method $\hat{U}_{2p}$ approximates the exact evolution operator (1.3) as

$$\hat{U}(\Delta t) = \hat{U}_{2p}(\Delta t) + \mathcal{O}(\Delta t^{2p+1}), \tag{2.3}$$

where $\mathcal{O}(\Delta t^{2p+1})$ is the local error of $\hat{U}_{2p}$, the local error of the composition (2.1) is given by $\mathcal{O}[\sum_{n=1}^{M} (\gamma_n \Delta t)^{2p+1}]$. Therefore, the composition coefficients are chosen so that this error vanishes, which is ensured when the composition coefficients satisfy the relation

$$\sum_{n=1}^{M} \gamma_n^{2p+1} = 0. \tag{2.4}$$

Note that this condition only increases the order of convergence of the composition to $2p+1$. By ensuring that the composition coefficients are symmetric, i.e.,

$$\gamma_{M+1-n} = \gamma_n, \tag{2.5}$$

the order of convergence of the composition (2.1) is further increased to $2p+2$ because it can be demonstrated [88] that any symmetric method has an even order of convergence.

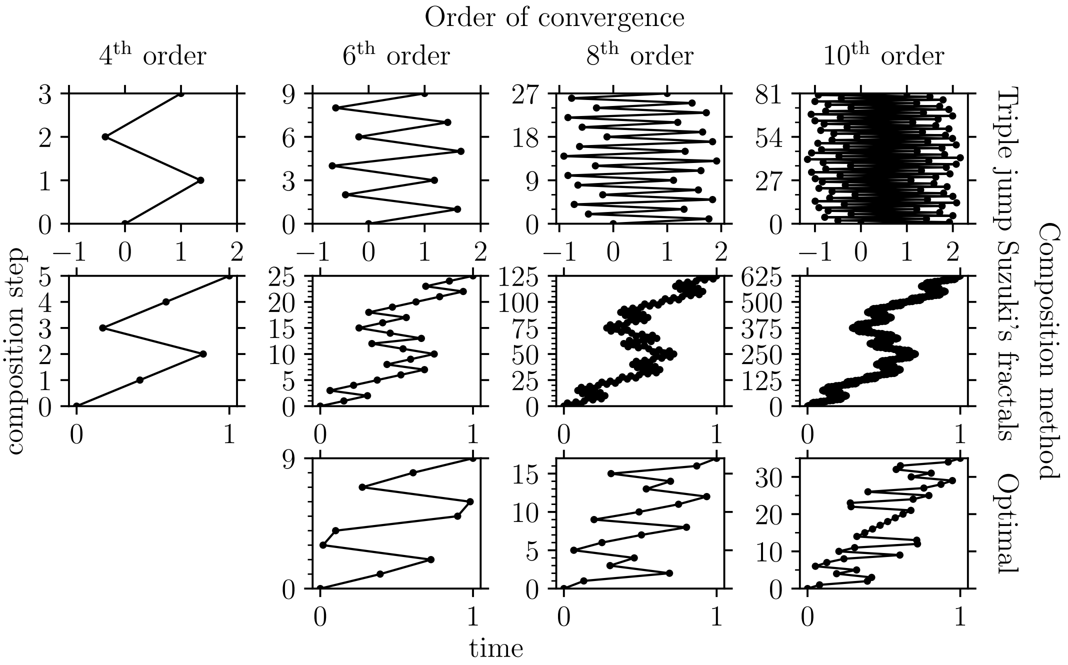

Figure 2.1 – Pictorial representation [104] of the recursive (triple-jump and Suzuki's fractal) and nonrecursive "optimal" composition schemes.

The simplest symmetric composition schemes (see Fig. 2.1) are the triple jump [120–122, 134] with $M = 3$,

$$\gamma_1 = \frac{1}{2 - 2^{1/(p+1)}} = \gamma_3, \qquad \gamma_2 = -\frac{2^{1/(p+1)}}{2 - 2^{1/(p+1)}}, \tag{2.6}$$

and Suzuki's fractal [121] with $M = 5$,

$$\gamma_1 = \gamma_2 = \frac{1}{4 - 4^{1/(p+1)}} = \gamma_4 = \gamma_5, \qquad \gamma_3 = -\frac{4^{1/(p+1)}}{4 - 4^{1/(p+1)}}. \tag{2.7}$$

Note that from Eqs. (2.6)–(2.7), a composed method of order p requires $(5/3)^{\frac{p}{2}-1}$ more composition steps if it is obtained using Suzuki's fractal rather than with the triple jump composition. Therefore, for a single time step, the pth-order method obtained with Suzuki's fractal is also $(5/3)^{\frac{p}{2}-1}$ slower than the method of the same order obtained with the triple jump composition. However, the leading order error coefficient of a pth-order method obtained with Suzuki's fractals is smaller than its analogous method obtained with the triple-jump composition because the magnitude of the composition coefficients are smaller in Suzuki's fractals. Consequently, to reach the same final error at the end of a simulation, larger time steps can be employed with integrators obtained from Suzuki's fractal compared to those based on the triple jump. For specific orders of convergence, more efficient non-recursive composition schemes exist and will be referred to as "optimal." These were implemented according to Kahan and Li [133], who obtained, by minimizing $\max_n |\gamma_n|$, composition methods for the sixth ($M = 9$) and eighth ($M = 17$) orders and according to Sofroniou and Spaletta [135], who found, by minimizing $\sum_{n=1}^{M} |\gamma_n|$, a composition scheme ($M = 35$) for the tenth order.

2.2.2 Compositions of split-operator algorithms

The split-operator algorithm is applicable if the Hamiltonian can be written as a sum

$$\hat{H} = \hat{A} + \hat{B} \tag{2.8}$$

of operators $\hat{A}$ and $\hat{B}$ with evolution operators, $\hat{U}_{\hat{A}}(t)$ and $\hat{U}_{\hat{B}}(t)$, whose actions on ψ_t can be evaluated exactly. Note that in Eq. (2.8), $\hat{H}$ represents a general separable Hamiltonian, which is not necessary $\hat{H}_0$ but can also be time-dependent $[\hat{H}(t)]$ or even nonlinear $[\hat{H}(\psi_t)]$. If the Hamiltonian is of the form (2.8), a general split-operator evolution operator can be expressed as

$$\hat{U}^{\mathrm{SO}}_{\hat{A}+\hat{B}}(\Delta t) = \hat{U}_{\hat{B}}(b_N \Delta t)\hat{U}_{\hat{A}}(a_N \Delta t) \cdots \hat{U}_{\hat{B}}(b_1 \Delta t)\hat{U}_{\hat{A}}(a_1 \Delta t),$$

where N is the number of splitting steps, and a_j and b_j are the splitting coefficients associated with the operators $\hat{A}$ and $\hat{B}$. These coefficients in general satisfy the identity $\sum_{j=1}^{N} a_j = \sum_{j=1}^{N} b_j = 1$, and are $a_1 = b_1 = 1$ for the first-order TV and VT algorithms [Eqs. (1.26)–(1.25)] and

$$a_1 = a_2 = \frac{1}{2}, \qquad b_1 = 1, \qquad b_2 = 0 \tag{2.9}$$

for the second-order VTV or TVT algorithms [Eqs. (1.29)–(1.30)].

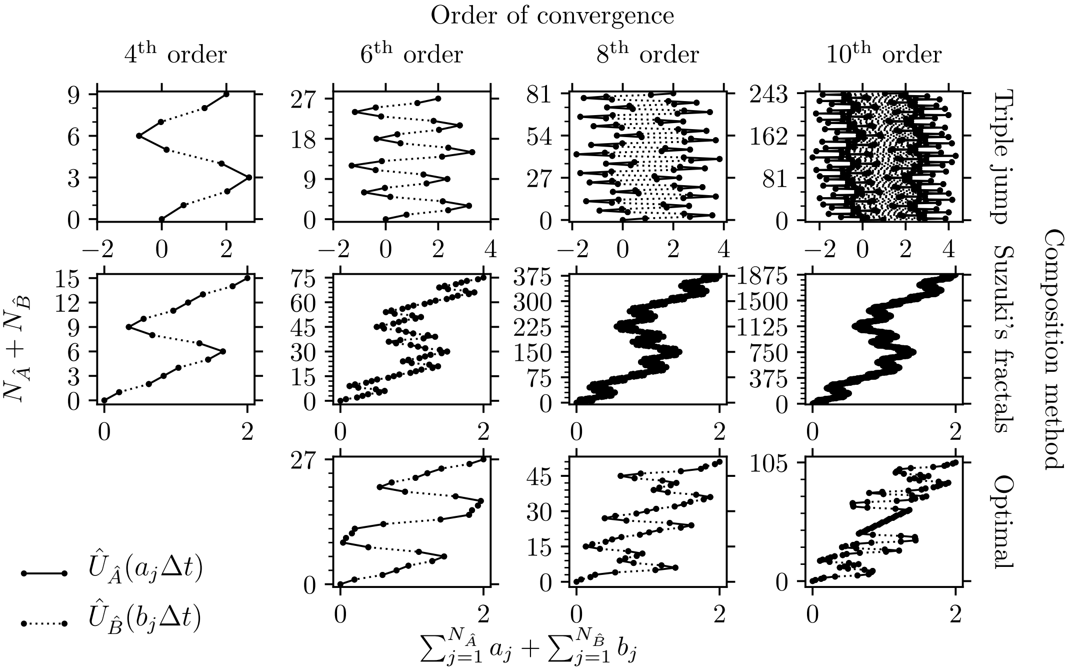

Figure 2.2 – Split-operator algorithms composed by the recursive (triple-jump and Suzuki's fractal) and nonrecursive "optimal" composition schemes shown in Fig. 2.1. In other words, each elementary method $\hat{U}(\gamma_n \Delta t)$ (solid line segment in Fig. 2.1) is replaced by a second-order split-operator algorithm $\hat{U}_{\hat{A}}(\gamma_n \Delta t/2)\hat{U}_{\hat{B}}(\gamma_n \Delta t)\hat{U}_{\hat{A}}(\gamma_n \Delta t/2)$, represented here by a triple of consecutive solid, dotted, and solid line segments. Solid line segments represent $\hat{U}_{\hat{A}}(\gamma_n \Delta t/2)$, whereas the dotted line segments represent $\hat{U}_{\hat{B}}(\gamma_n \Delta t)$. $N_{\hat{O}}$ is the number of actions of $\hat{U}_{\hat{O}}$ on ψ.

Because the second-order split-operator algorithm is symmetric, it can be composed by any of the composition schemes discussed in Sec. 2.2.1. For example, the splitting coefficients of a fourth-order method are

$$\begin{aligned}
a_1 = a_2 &= \frac{1}{2(2-2^{1/3})}, \qquad a_3 = -\frac{2^{1/3}}{2(2-2^{1/3})},\\
b_1 &= \frac{1}{2-2^{1/3}}, \qquad b_3 = -\frac{2^{1/3}}{2-2^{1/3}}, \qquad b_2 = b_6 = 0
\end{aligned} \tag{2.10}$$

with $N = 6$ if the triple-jump composition scheme [Eq. (2.6)] is used, and

$$\begin{aligned}
a_1 = a_2 = a_3 = a_4 &= \frac{1}{2(4-4^{1/3})}, \quad a_5 = -\frac{4^{1/3}}{2(4-4^{1/3})},\\
b_1 = b_3 &= \frac{1}{4-4^{1/3}}, \quad b_2 = b_4 = b_{10} = 0, \quad b_5 = -\frac{4^{1/3}}{4-4^{1/3}}
\end{aligned} \tag{2.11}$$

with $N = 10$ if Suzuki's fractal [Eq. (2.7)] is used instead. The remaining coefficients are obtained from symmetry as

$$a_{N-j+1} = a_j, \quad b_{N-j} = b_j. \tag{2.12}$$

Both composition procedures can be applied recursively to obtain higher-order split-operator algorithms. These as well as the optimally composed algorithms of up to the tenth order are represented pictorially in Fig. 2.2.

Table 2.1 – Geometric properties and computational cost of the first-order and recursively composed second-order split-operator (SO) algorithms. Cost (here before speedup by pruning splitting coefficients) is measured by the number of fast Fourier transforms required per time step (see Sec. 1.2.5). n is the number of recursive compositions and C the total number of composition steps per time step ($C = 3^n$ for the triple jump [121, 122], $C = 5^n$ for Suzuki's fractal [121]). + or − denotes that the geometric property of the exact evolution operator is or is not preserved.

Method	Order	Unitary	Symplectic	Commutes with $\hat{H}$	Energy cons.	Symmetric	Time-reversible	Stable	Cost
1st order SO	1	+	+	−	−	−	−	+	2
2nd order SO	$2(n+1)$	+	+	−	−	+	+	+	$2C$

All compositions of the second-order VTV or TVT split-operator algorithms are unitary, symplectic, and stable; all symmetric compositions are symmetric and, therefore, time-reversible. These geometric properties are summarized in Table 2.1 and justified in Appendix A.1.

2.2.3 Pruning splitting coefficients

Many b_j coefficients of the higher-order integrators obtained by recursive composition of the second-order split-operator algorithm are zero [for an example, see Eqs. (2.10) and (2.11)]. The computational cost can be reduced by "pruning," i.e., removing the splitting steps corresponding to $b_j = 0$ and merging the consecutive actions of $\hat{U}_{\hat{A}}(a_j \Delta t)$ and $\hat{U}_{\hat{A}}(a_{j+1} \Delta t)$. If $b_j = 0$ and $j \neq N$, the splitting coefficients are modified as

$$\begin{aligned}
&\tilde{b}_k = b_{k+1}, \quad \text{for} \quad j \leq k \leq N-1, \\
&\tilde{a}_j = a_j + a_{j+1}, \\
&\tilde{a}_k = a_{k+1}, \quad \text{for} \quad j+1 \leq k \leq N-1, \\
&\tilde{N} = N-1,
\end{aligned} \tag{2.13}$$

in order to merge the j^{th} and $(j+1)^{\text{th}}$ steps. The composed methods after the merge are exhibited in Fig. 2.3 and the reduction in the number N of splitting steps, which measures the computational cost, is summarized in Table 2.2.

For a time-independent separable Hamiltonian, one can either precompute and store the evolution operators, $\hat{U}_{\hat{A}}(a_j \Delta t)$ and $\hat{U}_{\hat{B}}(b_j \Delta t)$, or compute them on the fly. The former approach is more memory intensive than the latter, which does not store any evolution operators, but the computational cost is reduced since the evolution operators are only computed once at initialization. To alleviate the memory requirement of the former approach, one can exploit the repetition of certain splitting coefficients, which is obvious from Eqs. (2.10)–(2.11) and Fig. 2.3. If either $\hat{A}$ or $\hat{B}$ is time-dependent, it is always beneficial to compute the corresponding evolution operator pertaining to the time-dependent operator on the fly because no reduction in computational cost is possible by precomputing the evolution operators.

The effort spent in searching for repeated coefficients is reduced if the symmetries of the composition scheme and of the elementary method are exploited [see Eq. (2.12)]. The repeated coefficients are then identified from only half of the original coefficients a_j and b_j.

Once identified, only the unique evolution operators $\hat{U}_{\hat{A}}(a_j^{\text{unq}} \Delta t)$ and $\hat{U}_{\hat{B}}(b_j^{\text{unq}} \Delta t)$ are stored in arrays of lengths N_a^{unq} and N_b^{unq}, together with the information when

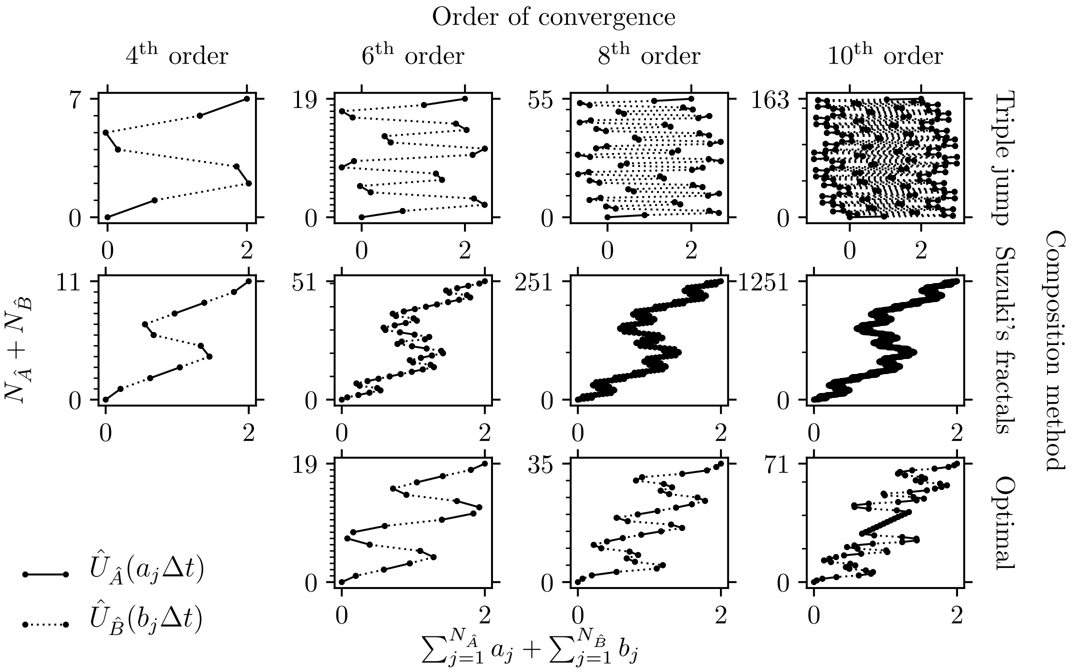

Figure 2.3 – Composed split-operator algorithms from Fig. 2.2 after removing zero splitting coefficients and merging adjacent coefficients, i.e., after each two adjacent solid line segments representing $\hat{U}_{\hat{A}}(\gamma_{n+1}\Delta t/2)\hat{U}_{\hat{A}}(\gamma_n \Delta t/2)$ in Fig. 2.2 are merged into a single solid line segment representing $\hat{U}_{\hat{A}}[(\gamma_n + \gamma_{n+1})\Delta t/2]$.

to apply them, stored in integer arrays I^a and I^b of length N, containing the indices in unique coefficient arrays, i.e.,

$$1 \leq I^a_j \leq N^{\text{unq}}_a, \qquad 1 \leq I^b_j \leq N^{\text{unq}}_b. \tag{2.14}$$

Exploiting the repeated coefficients, the number of stored evolution operators reduces from $2N$ to $N^{\text{unq}}_a + N^{\text{unq}}_b$ (see Table 2.2).

2.2.4 Molecular Hamiltonian in the diabatic basis

The molecular Hamiltonian in the diabatic basis can be expressed as

$$\hat{\mathbf{H}}_0 = \frac{1}{2}\hat{p}^T \cdot m^{-1} \cdot \hat{p}\,\mathbf{1} + \mathbf{V}_0(\hat{q}), \tag{2.15}$$

where m is the diagonal $D \times D$ nuclear mass matrix, D the number of nuclear degrees of freedom, and $\mathbf{V}_0$ the potential energy. In Eq. (2.15), the dot symbol

Table 2.2 – Computational cost and memory requirement of the composed split-operator algorithms before and after pruning (i.e., removing zero coefficients and merging adjacent coefficients) and identifying repeated coefficients. The computational cost is measured by $N_{\hat{A}} + N_{\hat{B}}$, where $N_{\hat{O}}$ is the number of actions of $\hat{U}_{\hat{O}}$ on the wavepacket. The memory requirement before and after pruning is $N_{\hat{A}} + N_{\hat{B}}$, and after identifying repeated coefficients decreases to $N_a^{\text{unq}} + N_b^{\text{unq}}$.

Composition method	Order	$N_{\hat{A}} + N_{\hat{B}}$ before merge [1]	$N_{\hat{A}} + N_{\hat{B}}$ after merge [2]	N_a^{unq}	N_b^{unq}
Elementary methods	1	2	2	1	1
	2	3	3	1	1
Triple jump	4	9	7	2	2
	6	27	19	4	4
	8	81	55	8	8
	10	243	163	16	16
Suzuki's fractal	4	15	11	3	2
	6	75	51	6	4
	8	375	251	12	8
	10	1875	1251	24	16
Optimal	6	27	19	5	5
	8	51	35	9	9
	10	105	71	18	18

[1] $N_{\hat{A}} = 2N_{\hat{B}}$ for order ≥ 2.
[2] $N_{\hat{A}} = N_{\hat{B}} + 1$ for order ≥ 2.

$(\cdot)$ denotes the matrix product in nuclear D-dimensional vector space, the hat symbol $(\hat{\ })$ represents a nuclear operator, and the bold font indicates an electronic operator, i.e., an $S \times S$ matrix, where S is the number of included electronic states. Using the dynamic Fourier method (Sec. 1.2.5), each evaluation of the action of the pair $\hat{\mathbf{U}}_{\hat{\mathbf{V}}_0}(\Delta t)$ and $\hat{\mathbf{U}}_{\hat{\mathbf{T}}}(\Delta t)$ on a molecular wavepacket $\boldsymbol{\psi}(t)$, which now becomes an S-component vector of nuclear wavepackets (one on each surface), involves two changes of the wavepacket's representation. In the numerical examples below, the Fourier transform was performed using the Fastest Fourier Transform in the West 3 (FFTW3) library [136]. Although its accuracy is sufficient for most applications, small deviations from unitarity, which were due to the high number of repeated application of the forward and backward Fourier transforms, affected the most converged calculations. To reduce the nonunitarity, we used the long-double instead of the default double precision version of FFTW3. The above-mentioned nonunitarity of the solution, partially due to the numerical implementation of the fast Fourier transform algorithm, was made worse by the matrix exponential required for evaluating the potential evolution operator $\hat{\mathbf{U}}_{\hat{\mathbf{V}}_\mathbf{0}}(\Delta t)$, which contains offdiagonal couplings between the electronic states. Although we tried different approaches for matrix exponentiation, including Padé approximants [137, 138] and exponentiating a diagonal matrix obtained with the QR decomposition [137, 139] or with the Jacobi method [137], none of the three methods was better than the others in reducing the nonunitarity. Since both in the NaI and pyrazine models, only 2 × 2 matrices are relevant, and since for such matrices, the Jacobi method yields already after one iteration the analytically exact result for the exponential, we used the Jacobi method for all results in Sec. 2.3. Note, however, that the other two methods (based on Padé approximants or QR decomposition), while not exact in the two models used in these examples, converge, in general, faster than the Jacobi method, and are, therefore, preferred in systems with more than two coupled electronic states.

2.2.5 Trapezoidal rule and implicit midpoint method

In addition to nonconservation of energy, the main disadvantage of the split-operator algorithms is that they can be applied to nonadiabatic dynamics only in the diabatic representation. Yet, there exist closely related, arbitrary-order geometric integrators, discussed in Ref. [104], which, in addition, conserve energy and are applicable both in the diabatic and adiabatic representations. These integrators are, like the higher-order split-operator algorithms, based on recursive symmetric composition (see Sec. 2.2.1) of the second-order trapezoidal rule or the implicit midpoint method, which were presented in Sec. 1.2.3. Due to the presence of implicit steps, the trapezoidal rule, implicit midpoint method as well as their compositions require solving large, although sparse, linear systems iteratively [104], and, as a result, in the diabatic representation are expected to be significantly less efficient than the explicit split-operator algorithms of the same order of accuracy. More details about these higher-order integrators can be found in Ref. [104], which discusses their geometric properties and studies their efficiency in applications to nonadiabatic quantum dynamics in the adiabatic representation, in which the molecular Hamiltonian is nonseparable.

2.3 Numerical examples

To test the geometric and convergence properties of the split-operator algorithms presented in Secs. 1.2.2, 1.2.3, and 2.2.1, we used these integrators to simulate the nonadiabatic quantum dynamics in a one- and three-dimensional systems.

2.3.1 One-dimensional model of NaI

Motivated by the experiment of Mokhtari *et. al.* [3], we used a one-dimensional two-surface diabatic model [131] of the NaI molecule. We assumed that the initial state was, before the electronic excitation, the ground vibrational eigenstate of a harmonic fit to the ground-state potential energy surface at equilibrium geometry. Therefore, the initial state is a one-dimensional Gaussian wavepacket of the form

$$\psi_0(x) = \prod_{j=1}^{D} (\sigma_{0,j}^2 \pi)^{-1/4} \exp[i p_{0,j}(x_j - q_{0,j})/\hbar - (x_j - q_{0,j})^2/2\sigma_{0,j}^2], \tag{2.16}$$

with $D = 1$, space coordinate $x = q$, initial position $q_{0,1} = 4.9889$ a.u., momentum $p_{0,1} = 0$ a.u. and width $\sigma_{0,1} = 0.110436$ a.u. This initial state was then excited to the excited-state potential energy surface by employing the sudden approximation, which assumes the simultaneous validity of the time-dependent perturbation theory and Condon and ultrashort pulse approximations during the excitation process. Then, the nonadiabatic dynamics was simulated by solving the time-dependent Schrödinger equation up to the final time $t_f = 10500$ a.u., which ensured that the wavepacket traverses the crossing of the two electronic states. For all the simulations, we employed a uniform grid with 2048 points between $q = 3.8$ a.u. and $q = 47.0$ a.u. which assured that the wavepacket at the final time t_f was converged (see Fig. A.1 in Appendix A.2).

The top panel of Fig. 2.4 shows the two diabatic potential energy surfaces as well as the initial wavepacket at $t = 0$ and the ground- and excited-state components of the final wavepacket at the final time $t_f = 10500$ a.u. The population dynamics of NaI, displayed in the middle and bottom panels of Fig. 2.4, shows that after passing

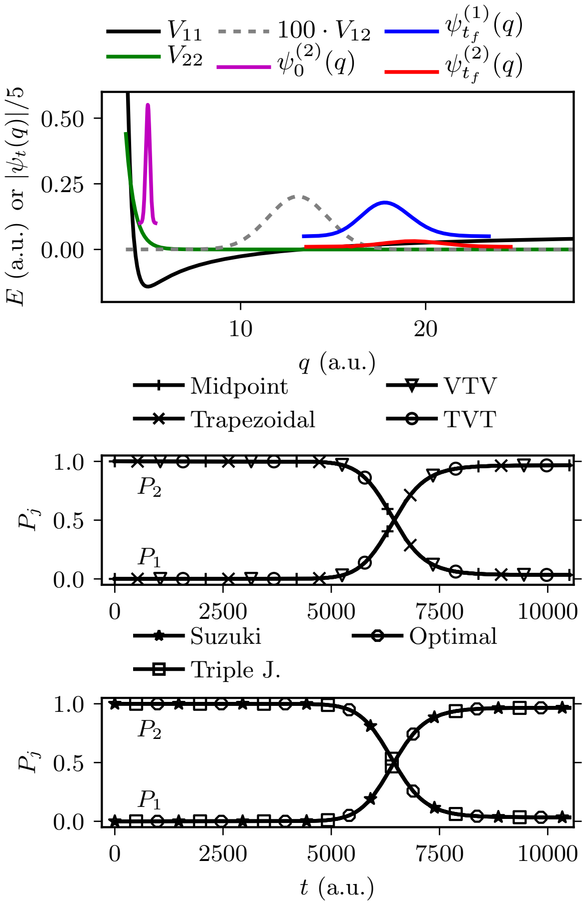

Figure 2.4 – Nonadiabatic dynamics of NaI. Top: Diabatic potential energy surfaces with the initial [$\psi_0^{(2)}(q)$] and final nuclear wavepacket components [$\psi_{t_f}^{(1)}(q)$ and $\psi_{t_f}^{(2)}(q)$] in the two diabatic electronic states [the initial ground-state component is not shown because it was zero: $\psi_0^{(1)}(q) = 0$]. Middle: Populations of NaI in the two diabatic states computed with four different second-order methods. Bottom: Populations computed with three different sixth-order compositions of the VTV algorithm. Populations were propagated with a time step $\Delta t = 0.01$ a.u. for the second-order methods and $\Delta t = 82.03125$ a.u. for the sixth-order methods, i.e., much more frequently than the markers suggest. The time step guaranteed wavepacket convergence errors below $\approx 10^{-5}$ in all methods.

the crossing, most of the population jumps to the other diabatic state, while a small fraction remains in the original, dissociative diabatic state. The converged populations obtained with the VTV and TVT split-operator algorithms agree, on the scale visible in the middle panel, with each other and also with the results of the implicit midpoint (1.27) and trapezoidal rule (1.28). Moreover, the results of the triple-jump, Suzuki's fractal, and optimal compositions of the second-order VTV algorithm agree with each other (bottom panel).

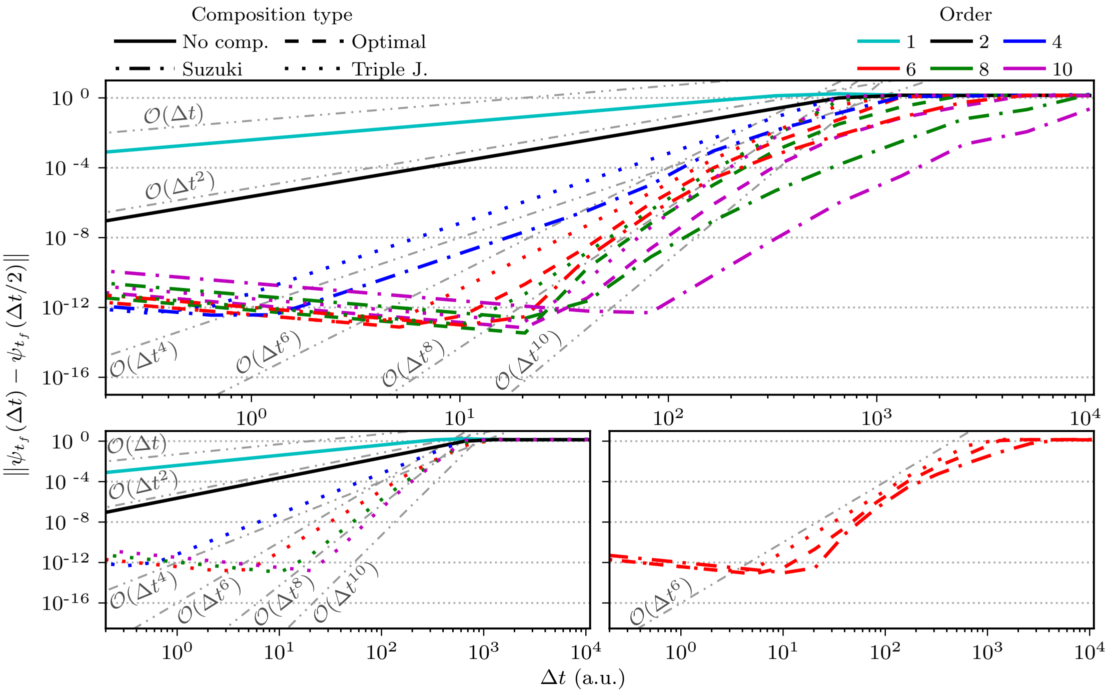

Figure 2.5 – Convergence of the molecular wavefunction as a function of the time step. The wavefunction was propagated with the VT algorithm or with the compositions of the VTV algorithm. Gray straight lines indicate various predicted orders of convergence $\mathcal{O}(\Delta t^n)$. Top: all discussed methods, bottom left: methods composed with the triple-jump scheme, bottom right: sixth-order methods.

For a quantitative comparison of various algorithms, it is necessary to compare their convergence errors at the final time t_f, which we measure, as a function of the time step Δt, by employing the L_2-norm error

$$\left\|\psi_{t_f}(\Delta t) - \psi_{t_f}(\Delta t/2)\right\|, \tag{2.17}$$

where $\psi_{t_f}(\tau)$ represents the wavepacket propagated to the final time t_f with a time step τ. This error is shown in Fig. 2.5, which confirms, for each algorithm, the asymptotic order of convergence predicted in Secs. 1.2.2, 1.2.3, and 2.2.1. For clarity, in this and all remaining figures, only the VT algorithm and compositions of the VTV algorithm are compared because the corresponding results of the TV algorithm and compositions of the TVT algorithms behave similarly. The top panel of Fig. 2.5 compares all methods, whereas the bottom left-hand panel compares only the different orders of the triple-jump composition and the bottom right-hand panel compares only different composition schemes with the sixth-order convergence. The prefactor of the error is the largest for the triple-jump [121, 122], intermediate for the optimal [133], and smallest for Suzuki's fractal composition [121], as previously obtained in Ref. [104]. The figure also shows that for the smallest time steps, the error starts to increase again. This is due to the accumulating numerical error of the fast Fourier transform, which eventually outweighs the error due to time discretization. As a result, the predicted asymptotic order of convergence cannot be observed for some methods because it is only reached for very small time steps.

While the probability density has a classical analogue, the phase of the wavefunction is a purely quantum property. As a consequence, an accurate evaluation of the phase is very important in the calculation of electronic spectra and in other situations, where quantum effects play a role. To investigate the convergence of the phase as a function of the time step, we used the phase of the wavefunction at the maximum of the probability density, i.e., $|\varphi(\Delta t) - \varphi(\Delta t/2)|$, where $\varphi(\Delta t) := \arg[\psi_{t_f}(q_{\max}, \Delta t)]$ and $q_{\max} := \arg\max_q[|\psi_{t_f}(q, \Delta t)|]$ is the position for which the amplitude of the wavefunction at the final time t_f, obtained using a time step Δt, achieves its maximum. Figure 2.6 displays the convergence of the error of the phase for the triple-jump compositions, and confirms that the order of convergence is the same as for the wavefunction itself (bottom left-hand panel of Fig. 2.5).

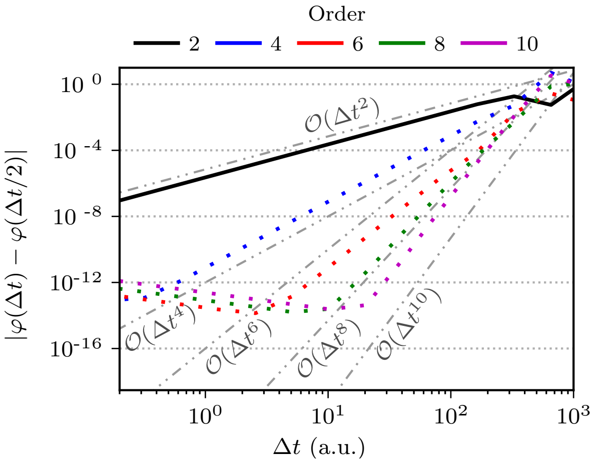

Figure 2.6 – Convergence error of the phase of the wavepacket as a function of the time step for the triple-jump compositions. Gray straight lines indicate various predicted orders of convergence $\mathcal{O}(\Delta t^n)$.

Because the number of composition steps depends on the composition scheme and

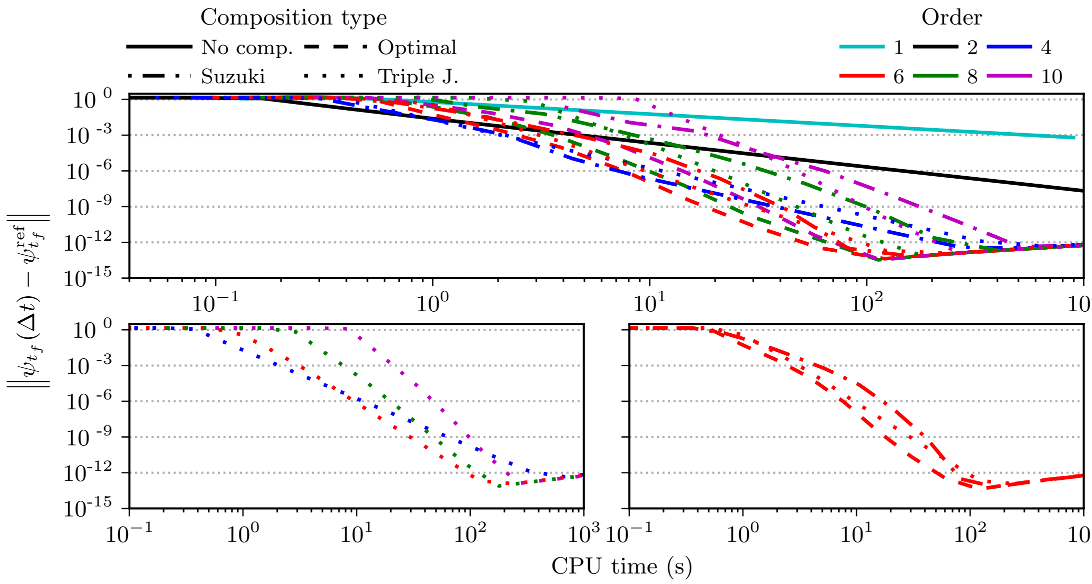

Figure 2.7 – Efficiency of the VT algorithm and of various compositions of the VTV algorithm shown using the dependence of the convergence error on the CPU time. Top: all methods, bottom left: triple-jump compositions, bottom right: sixth-order methods. The reference wavefunction $\psi_{t_f}^{\mathrm{ref}}$ was chosen as the most accurate point in Fig. 2.5, i.e., the wavefunction obtained using the optimal eighth-order composition with a time step $\Delta t = t_f/2^9$.

increases with the order, the efficiency of an algorithm is not determined solely by the convergence error for a given time step Δt. It is, therefore, essential to compare directly the efficiency of the different algorithms. Figure 2.7 displays the wavefunction convergence error of each algorithm as a function of the computational cost, which we measure as the central processing unit (CPU) time. Comparison of the compositions of the VTV split-operator algorithm in the top panel of Fig. 2.7 shows that the fourth-order Suzuki composition already takes less CPU time to achieve convergence error 10^{-2} than does the elementary VTV algorithm. To reach errors below 10^{-2}, it is more efficient to use some of the fourth or higher-order integrators. Remarkably, the CPU time required to reach an error of 10^{-10} is roughly 600 times longer for the basic VTV algorithm than for its optimal sixth-order composition. The bottom right-hand panel of Fig. 2.7 confirms the prediction that the optimal compositions are the most efficient among composition methods of the same order.

Convergence curves in Figs. 2.5–2.7 were obtained using the long-double precision

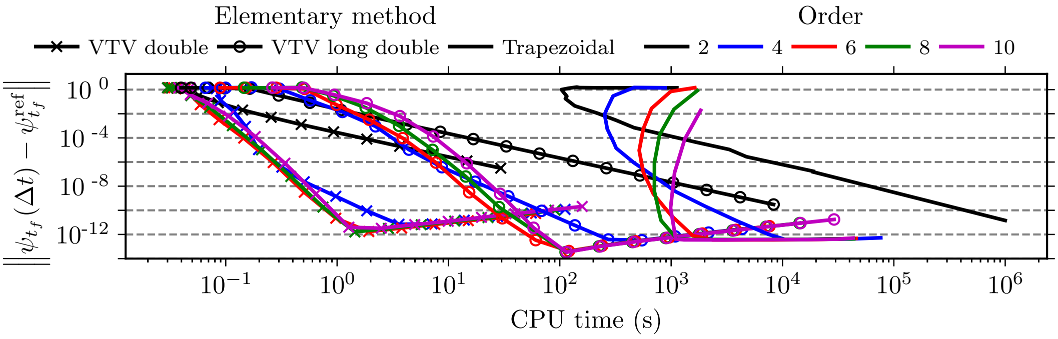

Figure 2.8 – Efficiency of the optimal compositions of the trapezoidal rule and of the VTV split-operator algorithm applied to the NaI model. For the trapezoidal rule, only the double precision version of the FFTW3 fast Fourier transform was used, while for the VTV split-operator algorithm, both double and long-double precision versions are compared. The "exact" reference wavefunction $\psi_{t_f}^{\mathrm{ref}}$ is the same as in Fig. 2.7. The result of the elementary second-order trapezoidal rule was extrapolated below the error of $\approx 10^{-7}$ using the line of best fit. As for the fourth-order algorithms, Suzuki's fractal is considered as the "optimal "composition scheme.

for the FFTW3 algorithm, which lowered the error accumulation resulting from the nonunitarity of the FFTW3 Fourier transform. If high accuracy is not desired, the double precision of the FFTW3 algorithm can be used instead, resulting in much more efficient higher-order algorithms. This is shown for the NaI model in Fig. 2.8, which compares the efficiency of the optimal compositions of the VTV algorithm evaluated either with the double or long-double implementation of the FFTW3, and also with the corresponding compositions of the trapezoidal rule (1.28) (for which the double precision of FFTW3 was sufficient). Even the more expensive, long-double precision calculation with the compositions of VTV algorithm are faster than the corresponding double precision calculations with the trapezoidal rule, which requires an expensive iterative solution of a system of linear equations. In particular, the sixth-order optimal composition of the VTV algorithm reaches a convergence error of 10^{-10} forty times faster than the same composition of the trapezoidal rule (see Fig. 2.8) and 30000 times faster than the elementary trapezoidal rule (see Figs. 2.7 and 2.8).

Note that the dependence of CPU time on the error in Fig. 2.8 is not monotonous for the compositions of the trapezoidal rule because the convergence of the numerical solution to the system of linear equations required more iterations for larger time steps; as a result, both the error and CPU time increased for time steps larger than a certain critical value.

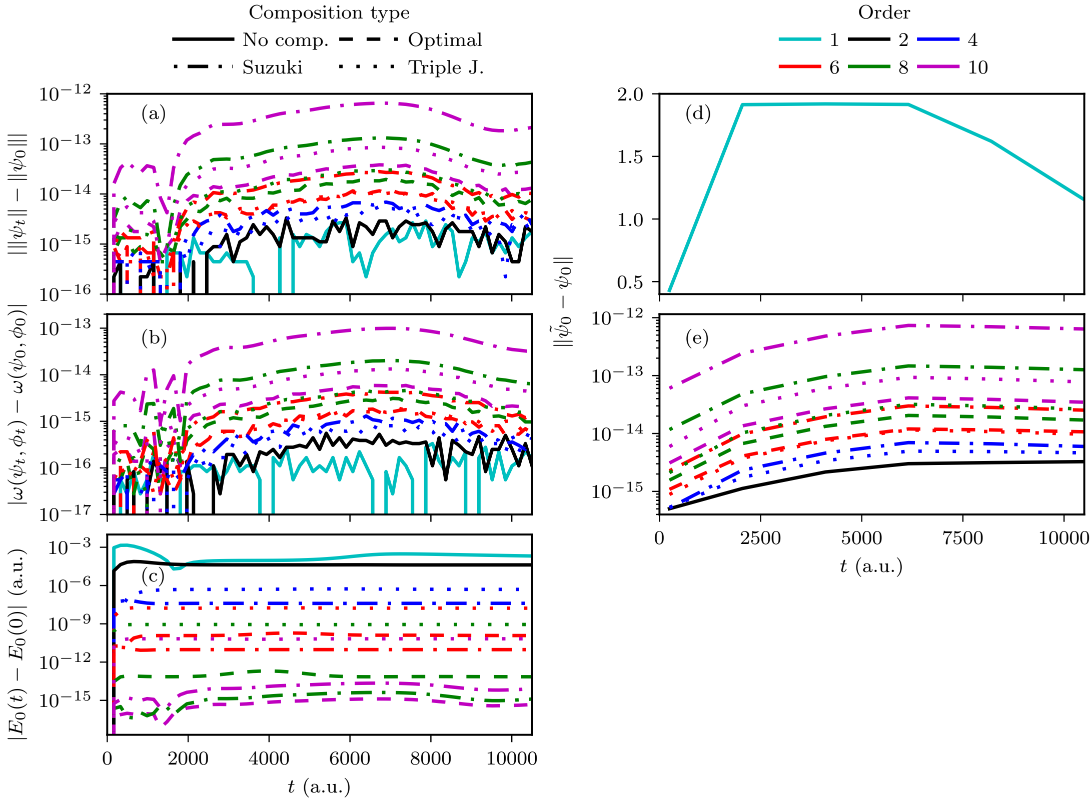

Figure 2.9 – Conservation of geometric properties by various algorithms: (a) norm, (b) symplectic two-form, (c) molecular energy, and (d)–(e) time reversibility. ϕ_0 is a Gaussian wavepacket with $q_0 = 5.05$ a.u., $p_0 = 2.5$ a.u., and σ_0 identical to that of ψ_0. Time reversibility was measured by the distance of the initial state ψ_0 from a forward-backward propagated state $\tilde{\psi}_0 := \hat{U}(-t)\hat{U}(t)\psi_0$, i.e., the state ψ_0 propagated first forward in time for time t and then backward in time for time t [see Eq. (1.11)]. The NaI model and a time step $\Delta t = t_f/2^7$ a.u. was used in all calculations.

To check that the increased efficiency of higher-order compositions is not achieved by sacrificing the conservation of geometric invariants, we analyzed, using the NaI model, the conservation of norm, symplectic two-form, molecular energy, and time reversibility. Conservation of the norm and symplectic two-form, and nonconservation of molecular energy by all split-operator algorithms is demonstrated in panels (a)–(c) of Fig. 2.9. The tiny residual errors ($< 10^{-12}$ in all cases) result from accumulated numerical errors of FFTW3 and matrix exponentiation (see Sec. 2.2.4). Panels (d) and (e) confirm, on one hand, that the first-order split-operator algorithm is not time-reversible, and, on the other hand, that the second-order VTV algorithm together with all its compositions are exactly time-reversible; the tiny residual errors are again due to accumulated numerical errors of the fast Fourier transform and matrix exponentiation.

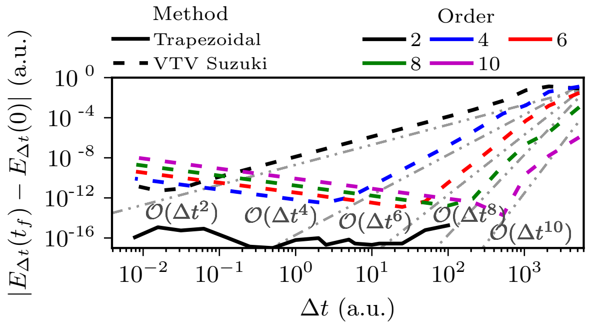

Figure 2.10 – Conservation of molecular energy as a function of the time step in simulations of the nonadiabatic dynamics of NaI. Note that $E_{\Delta t}(t)$ denotes the molecular energy $E_0(t)$ at time t and obtained using a time step Δt. Gray straight lines indicate various orders of convergence $\mathcal{O}(\Delta t^n)$.

The nonconservation of energy by the split-operator algorithms is further inspected in Fig. 2.10, showing the error of energy as a function of the time step. For the Suzuki's fractal compositions of the VTV algorithm, the energy is only conserved approximately; its conservation follows the order of convergence of the integrator, as indicated by the gray lines. In contrast, the trapezoidal rule conserves the energy to machine accuracy, regardless of the size of the time step.

2.3.2 Three-dimensional model of pyrazine

To investigate how the dimensionality of the system affects the efficiency of various algorithms, we also performed analogous simulations of a three-dimensional three-surface vibronic coupling model of pyrazine. The model, which includes only the normal modes Q_1, Q_{6a}, and Q_{10a}, was constructed by following the procedure from Ref. [132] with the experimental values from Ref. [140] for the vertical excitation energies. Thirty-two equidistant grid points between $x_i = -7$ a.u. and $x_i = 7$ a.u. were included for each vibrational mode. Therefore, the total number of grid points was increased to 32768. The initial three-dimensional Gaussian wavepacket was obtained as the vibrational ground state of the ground-state potential energy surface [Eq. (2.16), with $D = 3$, $x = (Q_1, Q_{6a}, Q_{10a})$ as well as $q_{0,j} = 0$, $p_{0,j} = 0$ and $\sigma_{0,j} = 1$ a.u. for $j = 1, 2, 3$]. Using the sudden approximation, employed also for the NaI model, this initial wavepacket was then promoted to the second excited electronic state and the nonadiabatic quantum dynamics performed until a final time $t_f = 10000$ a.u. The population dynamics, shown in Fig 2.11, indicates significant nonadiabatic transitions between the two excited states, while the ground surface remains unpopulated. Moreover, on the scale visible in the figure, the population dynamics obtained with sixth-order optimal compositions of the VTV algorithm and of the trapezoidal rule agree with each other.

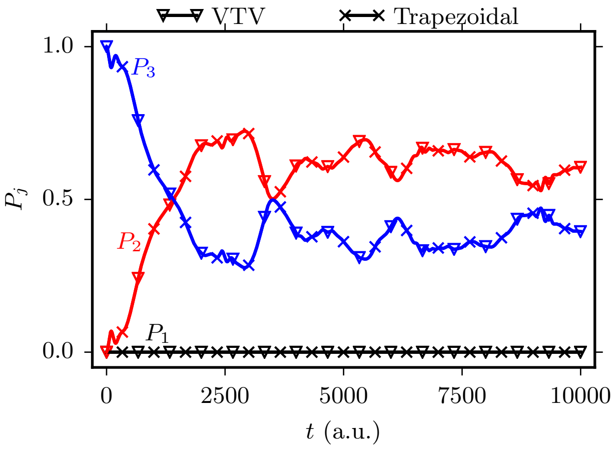

Figure 2.11 – Population dynamics of pyrazine obtained using the sixth-order optimal compositions of the trapezoidal rule and VTV algorithm. The same time step $\Delta t = t_f/25600$ was used for both calculations.

Figure 2.12 compares the efficiency of different (yet always optimal) compositions of the VTV algorithm and trapezoidal rule. Higher-order integrators become more efficient already for convergence errors below 10^{-2} for compositions of the VTV algorithms and, remarkably, already for errors below 10^{-1} for compositions of the trapezoidal rule. In particular, to reach an error of 10^{-10}, a 900-fold speedup over the second-order VTV algorithm and a 300-fold speedup over the second-order trapezoidal rule are achieved by using their tenth-order optimal compositions. These results suggest that increasing the number of dimensions is either beneficial or, at the very least, not detrimental to the gain in efficiency from using the higher-order integrators. As in Fig. 2.8, the compositions of the VTV algorithms are much more efficient than the compositions of the trapezoidal rule, but this was expected, because the Hamiltonian (2.15) is separable. One must remember that the main purpose of the compositions of the trapezoidal rule is for nonseparable Hamiltonians, where the split-operator algorithms cannot be used at all.

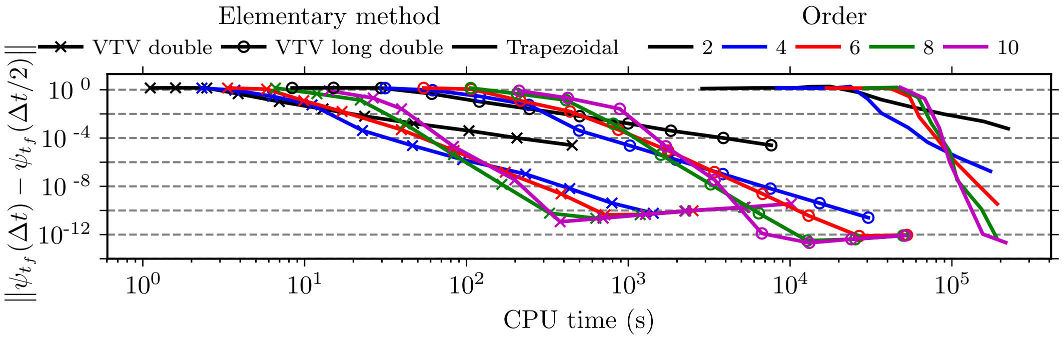

Figure 2.12 – Efficiency of the optimal compositions of the trapezoidal rule and VTV split-operator algorithm applied to the three-dimensional pyrazine model. For the trapezoidal rule, only the double precision version of the FFTW3 fast Fourier transform was used, while for the VTV split-operator algorithm, both double and long-double precision versions are compared. As for the fourth-order algorithms, Suzuki's fractal is considered as the "optimal" composition scheme.

2.4 Conclusion

We have described geometric integrators for nonadiabatic quantum dynamics in the diabatic representation, in which the Hamiltonian is separable into a kinetic term, depending only on momentum, and potential term, depending only on position. These integrators are based on recursive symmetric composition of the standard, second-order split-operator algorithm, and as a result, are explicit, unconditionally stable and exactly unitary, symplectic, symmetric, and time-reversible. Unlike the original split-operator algorithm, which is only second-order, its recursive symmetric compositions can achieve accuracy of an arbitrary even order in the time step. These properties were justified analytically and demonstrated numerically on a diabatic two-surface model of NaI photodissociation. Indeed, the higher-order integrators sped up calculations by several orders of magnitude when higher accuracy was required. For example, the CPU time required to achieve a convergence error of 10^{-10} was reduced by a factor of 600 when the optimal sixth-order composition was used instead of the elementary second-order split-operator algorithm. The gain in efficiency due to the higher-order integrators was also confirmed by the nonadiabatic simulations in a diabatic three-dimensional three-surface model of pyrazine. Although other efficient propagation methods, such as Chebyshev [76] or short iterative Lanczos schemes [73, 74], might have comparable efficiency in this and other typical chemical systems, in contrast to the integrators presented here, those methods do not preserve time reversibility and several other geometric properties of the exact solution.

3 Geometric high-order integrator for the nonlinear time-dependent Schrödinger equation

The explicit split-operator algorithm has been extensively used for solving both linear and nonlinear time-dependent Schrödinger equations. When applied to the nonlinear Gross–Pitaevskii equation, the method remains time-reversible, norm-conserving, and retains its second-order accuracy in the time step. However, this algorithm is not suitable for all types of nonlinear Schrödinger equations. Indeed, we demonstrate that local control theory, a technique for the quantum control of a molecular state, translates into a nonlinear Schrödinger equation with a more general nonlinearity, for which the explicit split-operator algorithm loses time reversibility and efficiency (because it has only first-order accuracy). Similarly, the trapezoidal rule, while time-reversible, does not conserve the norm of the state propagated by a nonlinear Schrödinger equation. To overcome these issues, we present high-order geometric integrators suitable for general time-dependent nonlinear Schrödinger equations and applicable to nonseparable Hamiltonians. Based on the symmetric compositions of the implicit midpoint method, these integrators are both norm-conserving and time-reversible. Beyond this, the geometric properties of the integrators are proven analytically and demonstrated numerically on the local control of a two-dimensional model of retinal. For highly accurate calculations, the higher-order integrators are more efficient. For example, for a wavefunction error of 10^{-9}, using the eighth-order algorithm yields a 48-fold speedup over the second-order implicit midpoint method and trapezoidal rule, and a 400000-fold speedup over the explicit split-operator algorithm.

The content of this Chapter has been adapted from Ref. [141].

3.1 Introduction

By definition, nonlinear time-dependent Schrödinger equations contain Hamiltonians that depend on the quantum state. Such state-dependent effective Hamiltonians appear in many areas of physics and chemistry. Examples include the approximations generated by the Dirac–Frenkel variational principle [89, 142–144], such as the multiconfigurational time-dependent Hartree method [55, 58, 145], variational Gaussian approximation [33, 34], and variational multiconfigurational Gaussian method [43, 146]. Furthermore, such examples appear in methods based on local expansion of the potential, such as the thawed Gaussian approximation [29, 50, 147], Hagedorn wavepacket method [34, 148, 149], or single Hessian approximation [150, 151]. Additionally, many numerical methods for solving the linear Schrödinger equation, such as the short-iterative Lanczos algorithm [71, 73, 74], can be interpreted as exact solutions of an effective nonlinear time-dependent Schrödinger equation. Probably the best known nonlinear Schrödinger equations, however, are approximate equations for Bose–Einstein condensates [152, 153], in which the Hamiltonian depends on the probability density of the quantum state.

The dynamics of a Bose–Einstein condensate is often modeled by solving the celebrated Gross–Pitaevskii equation with a cubic nonlinearity [154–158]. To solve this equation, several numerical schemes, such as the first-order explicit split-operator algorithms [Eqs. (1.25)–(1.26)] or time and spatial finite difference methods, are employed [159, 160]. These methods are of low accuracy (in time, space, or both) and do not always preserve the geometric properties of the exact solution [161]. For example, the Crank–Nicolson finite difference method is geometric but exhibits only second-order convergence with respect to the spatial discretization. To remedy this, the explicit second-order split-operator algorithm [Eqs. (1.29)–(1.30)], commonly used for the linear time-dependent Schrödinger equation [Eq. (1.15)], provides a great alternative, as it conserves, in some cases, the geometric properties of the exact solution and has spectral accuracy in space. Unfortunately, this algorithm cannot be used for all types of nonlinear time-dependent Schrödinger equations. Indeed, in the case of the Gross–Pitaevskii equation, this algorithm is symmetric and, therefore, time-reversible only because the ordinary differential equation that must be solved when propagating the molecular state with the potential part of the Hamiltonian leaves the nonlinear term invariant in time [159]. We show here that for nonlinear terms of more general form, this algorithm becomes implicit. If this implicit nature is not considered and the explicit version is used, the algorithm loses its time reversibility and efficiency due to its low accuracy, which is only of the first order in the time step.

An example of a situation, where a more general nonlinearity appears, is provided by local control theory. As discussed in Sec. 1.1.3, this technique employs a pulse [Eq. (1.20)] that is computed on the fly, based on the instantaneous molecular state, to increase or decrease an expectation value of a specified operator. Because the time dependence of the pulse is determined exclusively by the molecular state, the time-dependent Schrödinger equation becomes autonomous but nonlinear.

Furthermore, the nonlinear nature of local control theory is often not acknowledged and the standard explicit split-operator algorithm for linear time-dependent Schrödinger equations is used [96, 99–101, 103], instead of its time-reversible, second-order, but implicit alternative. Most previous studies have used local control theory for applications requiring neither high accuracy nor time reversibility. Therefore, these works could rely on this approximate explicit integrator, which, as displayed below, in the context of local control theory, has only first-order accuracy in the time step and is time-irreversible. However, such an algorithm would be very inefficient for highly accurate calculations, and could not be used at all if exact time reversibility were important. Because this failure of the explicit splitting algorithm in local control theory is generic, while its success in the Gross–Pitaevskii equation is rather an exception, it is desirable to develop efficient high-order geometric integrators suitable for a general nonlinear time-dependent Schrödinger equation.

In Chapter 2, we presented high-order time-reversible geometric integrators for the nonadiabatic quantum dynamics driven by the linear time-dependent Schrödinger equation. In this Chapter, we extend this approach to the general nonlinear Schrödinger equation, to address the slow convergence and time irreversibility of the explicit split-operator algorithm.

The remainder of this Chapter is organized as follows: In Sec. 3.2, we define the nonlinear time-dependent Schrödinger equation, discuss its geometric properties, and explain how local control theory leads to a nonlinear Schrödinger equation. In Sec. 3.3, after demonstrating the loss of geometric properties by Euler methods, we describe how these geometric properties are recovered and how accuracy is increased to an arbitrary even order by symmetrically composing both implicit and explicit

Euler methods. Then, we describe a general procedure to perform the implicit propagation and derive explicit expressions for the case of local control theory. Furthermore, we show the derivation of the approximate explicit split-operator algorithm for the nonlinear Schrödinger equation and explain how this algorithm loses time reversibility. Finally, in Sec. 3.4 we numerically verify the convergence and geometric properties of the integrators by controlling, using local control theory, either the population or energy transfer in a two-state two-dimensional model of retinal [162].

3.2 Nonlinear Schrödinger equation

The *nonlinear time-dependent Schrödinger equation* is the differential equation

$$i\hbar\frac{d}{dt}|\psi_t\rangle = \hat{H}(\psi_t)|\psi_t\rangle, \tag{3.1}$$

describing the time evolution of the state ψ_t driven by the nonlinear Hamiltonian operator $\hat{H}(\psi_t)$, which depends on the state of the system. This dependence on ψ_t is what distinguishes the equation from the linear Schrödinger equation (1.1). As the notation in Eq. (3.1) suggests, we shall always assume that while the operator $\hat{H} : \psi \mapsto \hat{H}(\psi)\psi$ is nonlinear, for each ψ the operator $\hat{H}(\psi) : \phi \mapsto \hat{H}(\psi)\phi$ is linear. We will also assume that $\hat{H}(\psi)$ has real expectation values $\langle\hat{H}(\psi)\rangle_\phi$ in any state ϕ, which for a linear operator implies that it is Hermitian, i.e., $\hat{H}(\psi)^\dagger = \hat{H}(\psi)$, or, more precisely, that for every ψ, ϕ, χ,

$$\langle\phi|\hat{H}(\psi)\chi\rangle = \langle\hat{H}(\psi)\phi|\chi\rangle. \tag{3.2}$$

A paradigm of a nonlinear Schrödinger equation is the Gross–Pitaevskii equation [154, 155, 158], which is expressed as

$$i\hbar\partial_t\psi_t(q) = -\frac{\hbar^2}{2m}\nabla^2\psi_t(q) + V(q)\psi_t(q) + C|\psi_t(q)|^2\psi_t(q)$$

in position representation, where the real coefficient C is positive for a repulsive interaction and negative for an attractive interaction. This equation has a cubic nonlinearity and is useful, e.g., for approximate modeling of the dynamics of a

Bose–Einstein condensate [161]. Many other examples are provided by the Dirac–Frenkel variational principle [142, 143], which approximates the exact solution of a linear Schrödinger equation with general Hamiltonian $\hat{H}$ by an optimal solution of a predefined, restricted form within a certain subset (called the approximation manifold) of the Hilbert space. This optimal solution ψ_t satisfies the equation

$$\langle \delta\psi_t | (i\hbar d/dt - \hat{H}) | \psi_t \rangle = 0, \tag{3.3}$$

where $\delta\psi_t$ is an arbitrary variation in the approximation manifold. Equation (3.3) is equivalent to the nonlinear Eq. (3.1) with an effective state-dependent Hamiltonian

$$\hat{H}(\psi_t) = \hat{P}(\psi_t)\hat{H},$$

where $\hat{P}(\psi_t)$ is the projection operator on the tangent space to the approximation manifold at the point ψ_t [34, 89]. (Note that in the very special case, where the projector does not depend on ψ_t, the resulting Schrödinger equation remains linear. This happens in the Galerkin method, in which ψ_t is expanded in a finite, time-independent basis and the approximation manifold is a vector space [89]).

3.2.1 Geometric properties of the exact evolution operator

With initial condition ψ_{t_0} and assuming that $t \geq t_0$, Eq. (3.1) has the formal solution $|\psi_t\rangle = \hat{U}(t, t_0; \psi)|\psi_{t_0}\rangle$ with the exact evolution operator given by

$$\hat{U}(t, t_0; \psi) := \mathcal{T} \exp\left[-\frac{i}{\hbar}\int_{t_0}^{t} dt' \hat{H}(\psi_{t'})\right], \tag{3.4}$$

where the dependence of $\hat{U}$ on ψ was added as an argument to emphasize the nonlinear character of Eq. (3.1). Expression (3.4) is obtained by solving the differential equation

$$i\hbar\frac{\partial}{\partial t}\hat{U}(t, t_0; \psi) = \hat{H}(\psi_t)\hat{U}(t, t_0; \psi)$$

with initial condition $\hat{U}(t_0, t_0; \psi) = 1$. The Hermitian adjoint of $\hat{U}(t, t_0; \psi)$ is the operator

$$\hat{U}(t, t_0; \psi)^{\dagger} = \bar{\mathcal{T}} \exp\left[\frac{i}{\hbar}\int_{t_0}^{t} dt' \hat{H}(\psi_{t'})\right] = \hat{U}(t, t_0; \psi)^{-1}, \tag{3.5}$$

where $\bar{\mathcal{T}}$ denotes the reverse time-ordering operator.

Compared to the linear case, the nonlinearity of the Hamiltonian leads to the loss of some geometric properties, even if Eq. (3.1) is solved exactly. Indeed, since the Hamiltonian is nonlinear, the exact evolution operator is also nonlinear.

Therefore, the exact evolution operator does not preserve the inner product because

$$\begin{aligned}\langle\psi_t|\phi_t\rangle &= \langle\hat{U}(t,t_0;\psi)\psi_{t_0}|\hat{U}(t,t_0;\phi)\phi_{t_0}\rangle \\ &= \langle\psi_{t_0}|\hat{U}(t,t_0;\psi)^\dagger\hat{U}(t,t_0;\phi)\phi_{t_0}\rangle \\ &= \langle\psi_{t_0}|\hat{U}(t,t_0;\psi)^{-1}\hat{U}(t,t_0;\phi)\phi_{t_0}\rangle \\ &\neq \langle\psi_{t_0}|\phi_{t_0}\rangle \end{aligned} \tag{3.6}$$

if $\psi_{t_0} \neq \phi_{t_0}$, where we used the property (3.5) of the Hermitian adjoint of $\hat{U}$ to obtain the third line. The exact nonlinear evolution operator is, therefore, not symplectic.

The nonlinear evolution does not conserve the total energy $E_{\text{tot}}(t) := \langle\hat{H}(\psi_t)\rangle_{\psi_t}$ since

$$\begin{aligned}\frac{dE_{\text{tot}}(t)}{dt} &= \langle\dot{\psi}_t|\hat{H}(\psi_t)|\psi_t\rangle + \langle\psi_t|\frac{d}{dt}\hat{H}(\psi_t)|\psi_t\rangle \\ &\quad + \langle\psi_t|\hat{H}(\psi_t)|\dot{\psi}_t\rangle \\ &= \langle d\hat{H}(\psi_t)/dt\rangle_{\psi_t} \neq 0,\end{aligned} \tag{3.7}$$

where the first and third terms in the intermediate step cancel each other because ψ_t satisfies the nonlinear Schrödinger equation (3.1). Note, however, that in special cases, such as the Gross–Pitaevskii equation, there exist modified energy functionals that are conserved [161].

The exact nonlinear evolution operator $\hat{U} \equiv \hat{U}(t,t_0;\psi)$ conserves the norm because

$$\begin{aligned}\|\psi_t\|^2 = \|\hat{U}\psi_{t_0}\|^2 &= \langle\hat{U}\psi_{t_0}|\hat{U}\psi_{t_0}\rangle \\ &= \langle\psi_{t_0}|\hat{U}^\dagger\hat{U}\psi_{t_0}\rangle = \langle\psi_{t_0}|\psi_{t_0}\rangle = \|\psi_{t_0}\|^2,\end{aligned} \tag{3.8}$$

where we used relation (3.5).

Similar to the linear case, the adjoint $\hat{U}(t,t_0;\psi)^*$ of $\hat{U}(t,t_0;\psi)$ is defined as the inverse of the evolution operator taken with a reversed time flow:

$$\hat{U}(t,t_0;\psi)^* := \hat{U}(t_0,t;\psi)^{-1}. \tag{3.9}$$

For the operator (3.4), the reverse evolution operator is given by the anti-time-ordered exponential

$$\hat{U}(t_0,t;\psi) := \bar{\mathcal{T}}\exp\left[-\frac{i}{\hbar}\int_t^{t_0} dt'\hat{H}(\psi_{t'})\right] \tag{3.10}$$

and, therefore, the adjoint is

$$\begin{aligned}\hat{U}(t,t_0;\psi)^* &= \left\{\bar{\mathcal{T}}\exp\left[-\frac{i}{\hbar}\int_t^{t_0} dt'\hat{H}(\psi_{t'})\right]\right\}^{-1}\\ &= \mathcal{T}\exp\left[\frac{i}{\hbar}\int_t^{t_0} dt'\hat{H}(\psi_{t'})\right]\\ &= \mathcal{T}\exp\left[-\frac{i}{\hbar}\int_{t_0}^{t} dt'\hat{H}(\psi_{t'})\right] = \hat{U}(t,t_0;\psi).\end{aligned} \tag{3.11}$$

Because it is equal to its adjoint, the previous equation shows that the exact evolution operator (3.4) is symmetric. Furthermore, it is also time-reversible because, due to symmetry, a forward propagation of an initial state followed by a backward propagation recovers the same initial state, i.e.,

$$\begin{aligned}&\hat{U}(t_0,t;\psi)\hat{U}(t,t_0;\psi)\psi_{t_0}\\ &= \hat{U}(t_0,t;\psi)^*\hat{U}(t,t_0;\psi)\psi_{t_0}\\ &= \hat{U}(t,t_0;\psi)^{-1}\hat{U}(t,t_0;\psi)\psi_{t_0} = \psi_{t_0}.\end{aligned} \tag{3.12}$$

Although the exact evolution conserves the norm, because it does not conserve the inner product, we cannot, in general, say anything about preserving the distance:

$$\begin{aligned}\|\psi_t-\phi_t\|^2 &= \|\psi_t\|^2+\|\phi_t\|^2-2\,\mathrm{Re}\langle\psi_t|\phi_t\rangle\\ &= \|\psi_{t_0}\|^2+\|\phi_{t_0}\|^2-2\,\mathrm{Re}\langle\psi_t|\phi_t\rangle\\ &= \|\psi_{t_0}-\phi_{t_0}\|^2+2\,\mathrm{Re}\left(\langle\psi_{t_0}|\phi_{t_0}\rangle-\langle\psi_t|\phi_t\rangle\right)\\ &\neq \|\psi_{t_0}-\phi_{t_0}\|^2.\end{aligned} \tag{3.13}$$

Moreover, since the sign of the real part of the difference of the inner products can be arbitrary, we cannot deduce anything about stability.

3.2.2 Nonlinear character of local control theory

We now show that the local coherent control of the time evolution of a quantum system with an electric field provides another example of a nonlinear Schrödinger equation. We have seen in Sec. 1.1.3 that the control field (1.20) is computed on the fly according to the current state of the system. This suggests that the control field can be either viewed as a function of time or a function of the molecular state [i.e., $\vec{E}_{\text{LCT}}(t) \equiv \vec{E}_{\text{LCT}}(\psi_t)$ in Eq. (1.20)]. More precisely, the control field does not depend on time explicitly but only implicitly through the dependence on ψ_t. Therefore, the time-dependent Schrödinger equation changes from a nonautonomous linear to an autonomous nonlinear differential equation [88]. By acknowledging this nonlinear character, the interaction potential from Eq. (1.17) becomes

$$\hat{V}_{\text{LCT}}(\psi_t) := -\hat{\vec{\mu}} \cdot \vec{E}_{\text{LCT}}(\psi_t) \tag{3.14}$$

and Eq. (1.15) becomes an example of a nonlinear time-dependent Schrödinger equation (3.1) with Hamiltonian operator $\hat{H}(\psi) := \hat{H}_0 + \hat{V}_{\text{LCT}}(\psi)$.

3.3 Geometric integrators for the nonlinear Schrödinger equation

Numerical propagation methods for solving the nonlinear equation (3.1) obtain the state at time $t + \Delta t$ from the state at time t by using the relation

$$|\psi_{t+\Delta t}\rangle = \hat{U}_{\text{appr}}(t + \Delta t, t; \psi)|\psi_t\rangle, \tag{3.15}$$

where $\hat{U}_{\text{appr}}(t + \Delta t, t; \psi)$ is an approximate nonlinear evolution operator depending on ψ. As the exact operator, these approximate evolution operators $\hat{U}_{\text{appr}}(t + \Delta t, t; \psi)$ are, therefore, nonlinear and conserve neither the inner product nor the symplectic form. Moreover, nothing can be said about their stability in general. However, some integrators may lose even the remaining geometric properties of the exact evolution: norm conservation, symmetry, and time reversibility. In this section, we simply state the properties that are lost by different methods; detailed proofs are provided in Appendix B.1.

3.3.1 Loss of geometric properties by Euler methods

The Euler methods (1.22)–(1.23), which were presented for the linear case in Sec. 1.2.1, can be adapted for solving a nonlinear time-dependent Schrödinger equation. In that situation, they approximate the exact evolution operator as

$$\hat{U}_{\text{expl}}(t+\Delta t, t; \psi_t) := 1 - \frac{i}{\hbar}\hat{H}(\psi_t)\Delta t, \tag{3.16}$$

$$\hat{U}_{\text{impl}}(t+\Delta t, t; \psi_{t+\Delta t}) := \left[1 + \frac{i}{\hbar}\hat{H}(\psi_{t+\Delta t})\Delta t\right]^{-1}. \tag{3.17}$$

As in the linear case, both methods are only first-order in the time step and, therefore, very inefficient. Moreover, both methods lose the norm preservation, symmetry, and time reversibility of the exact evolution operator.

3.3.2 Recovery of geometric properties and increasing accuracy by composition

As described in Sec. 1.2.3, composing the implicit and explicit Euler methods yields either the implicit midpoint or the trapezoidal rule, depending on the order of composition. In the nonlinear setting, employing such compositions modifies the implicit midpoint method (1.27) to

$$\begin{aligned}&\hat{U}_{\text{mid}}(t+\Delta t, t; \psi_{t+\Delta t/2})\\ &\qquad := \hat{U}_{\text{expl}}(t+\Delta t, t+\Delta t/2; \psi_{t+\Delta t/2})\hat{U}_{\text{impl}}(t+\Delta t/2, t; \psi_{t+\Delta t/2}),\end{aligned} \tag{3.18}$$

and the trapezoidal rule (1.28) to

$$\hat{U}_{\text{trap}}(t+\Delta t, t; \psi) := \hat{U}_{\text{impl}}(t+\Delta t, t+\Delta t/2; \psi_{t+\Delta t})\hat{U}_{\text{expl}}(t+\Delta t/2, t; \psi_t). \tag{3.19}$$

As in the linear case, both methods are second-order, symmetric, and time-reversible regardless of the size of the time step [88, 104]. However, only the implicit midpoint method is time-reversible at all time steps.

Because they are symmetric, both methods can be further composed, using the symmetric composition schemes [88, 89, 104, 121, 122, 133, 135] described in Sec. 2.2.1, to obtain integrators of arbitrary even order of accuracy in the time step. Indeed, Eq. (2.1) can be modified to

$$\hat{U}_{p+2}(t+\Delta t, t;\psi) := \hat{U}_p(t+\xi_M\Delta t, t+\xi_{M-1}\Delta t;\psi)\cdots\hat{U}_p(t+\xi_1\Delta t, t;\psi), \quad (3.20)$$

in order to generate a symmetric nonlinear method $\hat{U}_{p+2}$ of order $p+2$ from a symmetric nonlinear method $\hat{U}_p$ of order p. In Eq. (3.20), $\xi_n := \sum_{j=1}^{n}\gamma_j$ denotes the sum of the first n real composition coefficients γ_j, which satisfy the relations for symmetry, consistency, and order increase, given in Sec. 2.2.1.

3.3.3 Solving the implicit step in a general nonlinear Schrödinger equation

Similarly to the linear case, the implicit Euler method requires an implicit propagation. However, because its integrator [Eq. (3.17)] depends on the result of the propagation, $\psi_{t+\Delta t}$ is obtained by solving the nonlinear system

$$\hat{U}_{\text{impl}}(t+\Delta t, t;\psi_{t+\Delta t})^{-1}|\psi_{t+\Delta t}\rangle = |\psi_t\rangle, \quad (3.21)$$

which can be written as $f(\psi_{t+\Delta t}) = 0$ with the nonlinear functional

$$\begin{aligned} f(\psi) :&= \hat{U}_{\text{impl}}(\psi)^{-1}\psi - \psi_t \\ &= \left[\hat{1} + \frac{i}{\hbar}\hat{H}(\psi)\Delta t\right]\psi - \psi_t. \end{aligned} \quad (3.22)$$

A nonlinear system $f(\psi) = 0$ can be solved with the iterative Newton–Raphson method, which computes, until convergence is obtained, the solution $\psi^{(k+1)}$ at iteration $k+1$ from $\psi^{(k)}$ using the relation

$$\psi^{(k+1)} = \psi^{(k)} - \hat{J}(\psi^{(k)})^{-1}f(\psi^{(k)}), \quad (3.23)$$

where $\hat{J} := \frac{\delta}{\delta\psi}f(\psi)$ is the Jacobian of the nonlinear functional $f(\psi)$.

If the initial guess $\psi^{(0)}$ is close enough to the exact solution of the implicit propagation, the Newton–Raphson iteration (3.23) is a contraction mapping and by the fixed-point theorem is guaranteed to converge. We use as the initial guess the result of propagating ψ_t with the explicit Euler method [Eq. (3.16)]. Note that this initial guess is sufficiently close to the implicit solution only if the time step is small. If the time step is too large, the difference between the explicit and implicit propagations becomes too large for the algorithm to converge and no solution can be obtained.

Equation (3.23) requires computing the inverse of the Jacobian which is an expensive task. It is preferable to avoid this inversion by computing each iteration as

$$\psi^{(k+1)} = \psi^{(k)} + \delta\psi^{(k)} \tag{3.24}$$

where $\delta\psi^{(k)}$ solves the linear system

$$\hat{J}(\psi^{(k)})\delta\psi^{(k)} = -f(\psi^{(k)}). \tag{3.25}$$

We solve this linear system by the generalized minimal residual method [109, 110, 163], an iterative method based on the Arnoldi process [164, 165] (see Appendix C for a detailed presentation of this algorithm).

The procedure presented for solving the implicit propagation is applicable to any nonlinear system whose Jacobian is known analytically. Therefore, the integrators proposed in Secs. 3.3.1 and 3.3.2 can be employed for solving any nonlinear time-dependent Schrödinger equation of the form of Eq. (3.1), i.e., with a Hamiltonian $\hat{H}(\psi_t)$ depending on the state of the system.

To sum up, each implicit propagation step, given by the evolution operator (3.17), is performed as follows:

1. Compute the initial guess $\psi^{(0)}$ using the explicit Euler method [see Eq. (3.16)]. Choose an error threshold ε and a maximum iteration number m.
2. For $k = 0, 1, \ldots, m-1$, Do:
3. Compute $\delta\psi^{(k)}$ by solving the linear system shown in Eq. (3.25).
4. Compute a new approximate solution $\psi^{(k+1)}$ using Eq. (3.24).
5. If $\|f(\psi^{(k+1)})\| \leq \varepsilon$, take $\psi^{(k+1)}$ as the solution of the implicit step.
6. End Do. The algorithm fails when $k = m$ and no approximate solution has been found.

3.3.4 Solving the implicit step in local control theory

In the specific case of local control theory, the inverse of the implicit Euler method is

$$\hat{U}_{\mathrm{LCT,impl}}(\psi)^{-1} = \hat{1} + \frac{i}{\hbar}\Delta t[\hat{H}_0 + \hat{V}_{\mathrm{LCT}}(\psi)], \tag{3.26}$$

and the Jacobian of the nonlinear functional (3.22) is given by

$$\begin{aligned}
\hat{J}(\psi) &= \frac{\delta}{\delta\psi}\left[\hat{U}_{\mathrm{LCT,impl}}(\psi)^{-1}\right]\psi + \hat{U}_{\mathrm{LCT,impl}}(\psi)^{-1}\hat{1} \\
&= \frac{i}{\hbar}\Delta t\frac{\delta}{\delta\psi}\left[\hat{V}_{\mathrm{LCT}}(\psi)\right]\psi + \hat{U}_{\mathrm{LCT,impl}}(\psi)^{-1} \\
&= \frac{i}{\hbar}\Delta t\hat{V}_{\mathrm{LCT}}(\psi) + \hat{1} + \frac{i}{\hbar}\Delta t\left[\hat{H}_0 + \hat{V}_{\mathrm{LCT}}(\psi)\right] \\
&= \hat{1} + \frac{i}{\hbar}\Delta t[\hat{H}_0 + 2\hat{V}_{\mathrm{LCT}}(\psi)].
\end{aligned} \tag{3.27}$$

Note that to obtain the third row of Eq. (3.27), we used $\frac{\delta}{\delta\psi}[\hat{V}_{\mathrm{LCT}}(\psi)]\psi = \hat{V}_{\mathrm{LCT}}(\psi)$, where the generalized complex derivative [166] of the interaction potential is given by the bra vector

$$\frac{\delta}{\delta\psi}\hat{V}_{\mathrm{LCT}}(\psi) = -\hat{\vec{\mu}}\cdot\frac{\delta}{\delta\psi}\vec{E}_{\mathrm{LCT}}(\psi) = \mp\lambda i\hat{\vec{\mu}}\cdot\langle\psi|[\hat{\vec{\mu}},\hat{O}]. \tag{3.28}$$

3.3.5 Approximate application of the explicit split-operator algorithm to the nonlinear Schrödinger equation

The algorithms that we described above apply to Hamiltonians that are not only nonlinear but also nonseparable. If the time-dependent Schrödinger equation is linear and its Hamiltonian is separable, the midpoint method (1.27) remains implicit, but the split-operator algorithms and their compositions yield, as we have seen in Chapter 2, explicit high-order integrators satisfying most geometric properties (except for the conservation of energy). In the case of local control theory, if $\hat{H}_0$ is separable [Eq. (1.24)], so is the total Hamiltonian, which can be written as $\hat{H}(\psi) = \hat{T} + \hat{V}_{\mathrm{tot}}(\psi)$, where $\hat{V}_{\mathrm{tot}}(\psi) := \hat{V}_0 + \hat{V}_{\mathrm{LCT}}(\psi)$ is the sum of the system's and interaction potential energy operators. It is, therefore, tempting to use the split-operator algorithm, with the hope of obtaining an efficient explicit integrator.

More generally, let us assume that the Hamiltonian operator in the general nonlinear Schrödinger equation (3.1) can be separated as

$$\hat{H}(\psi) = T(\hat{p}) + V_{\mathrm{tot}}(\hat{q}, \psi).$$

Then, the VT (1.26) and TV (1.25) split-operator algorithms are adapted to the nonlinear case, which yields the explicit TV

$$\hat{U}_{\mathrm{TV}}(t + \Delta t, t; \psi_t) := \hat{U}_{\hat{T}}(\Delta t)\hat{U}_{\hat{V}_{\mathrm{tot}}(\psi_t)}(\Delta t), \tag{3.29}$$

and implicit VT

$$\hat{U}_{\mathrm{VT}}(t + \Delta t, t; \psi_{t+\Delta t}) := \hat{U}_{\hat{V}_{\mathrm{tot}}(\psi_{t+\Delta t})}(\Delta t)\hat{U}_{\hat{T}}(\Delta t) \tag{3.30}$$

split-operator algorithms. As in the linear case, these integrators are norm-conserving but only first-order accurate and time-irreversible. From their definitions (3.29) and (3.30), it follows immediately that the TV and VT algorithms are adjoints of each other and require, respectively, explicit and implicit propagations. By composing these two adjoints together, one obtains the modified TVT or VTV split-operator algorithms, which will be discussed in further detail in Chapter 4. Both TVT and VTV algorithms are norm-conserving, symmetric, and time-reversible. However, these geometric properties are only acquired if the implicit part, i.e., the propagation with the VT algorithm (3.30) is performed exactly. This procedure requires solving a nonlinear system, which can be performed using the Newton–Raphson method, as described in Sec. 3.3.3. This, however, implies abandoning the explicit nature of the split-operator algorithm, which is one of its main advantages over implicit methods for solving linear Schrödinger equations.

The nonlinearity of Eq. (3.1) is often not acknowledged. As a consequence, the implicit character of Eq. (3.30) is not taken into account and explicit alternatives are used. For example, instead of using $\psi_{t+\Delta t}$ in the VT algorithm (i.e., performing the implicit propagation exactly), the state $\psi_{t,\hat{T}\Delta t} := e^{-i\hat{T}\Delta t/\hbar}\psi_t$ obtained after the kinetic propagation is often used to perform the potential propagation. After composition with the TV algorithm, it yields the approximate explicit TVT split-operator algorithm

$$\begin{aligned}\hat{U}_{\text{expl TVT}}&(t+\Delta t; t, \psi_{t,\hat{T}\Delta t/2}) \\ &:= \hat{U}_{\text{TV}}(t+\Delta t; t+\Delta t/2, \psi_{t,\hat{T}\Delta t/2}) \\ &\qquad \times \hat{U}_{\text{VT}}(t+\Delta t/2; t, \psi_{t,\hat{T}\Delta t/2}). \end{aligned} \tag{3.31}$$

Because this approximate explicit integrator depends on $\psi_{t,\hat{T}\Delta t/2}$ instead of $\psi_{t+\Delta t/2}$, it is not time-reversible and achieves only first-order accuracy (see Appendix B.1 for proofs of the geometric properties). Indeed, any explicit version of the TVT or VTV algorithm will be first-order accurate and time-irreversible due to ignoring the implicit character of the VT algorithm. Nevertheless, the explicit algorithms can be used for performing practical local control theory calculations in typical situations, which do not require high accuracy [96, 99–101, 103].

3.4 Numerical examples

We tested the general integrators for the nonlinear Schrödinger equation, presented in Sec. 3.3, by using them for the local control of a two-dimensional two-state diabatic model of retinal taken from Ref. [162]. The model describes the *cis-trans* photo-induced isomerization of retinal—an ultrafast reaction mediated by a conical intersection which is the first event occurring in the biological process of vision. The two vibrational modes of the model are the reaction coordinate θ, an angle describing the torsional motion of the retinal molecule, and a vibronically active coupling mode q_c. In the diabatic representation, the Hamiltonian of the system in the absence of the field,

$$\hat{\mathbf{H}}_0 = \hat{T}\mathbf{1} + \begin{pmatrix} V_{11}(\hat{q}_c, \hat{\theta}) & V_{12}(\hat{q}_c) \\ V_{21}(\hat{q}_c) & V_{22}(\hat{q}_c, \hat{\theta}) \end{pmatrix}, \tag{3.32}$$

is separable into a sum of the kinetic energy operator

$$\hat{T} = -\frac{1}{2}\omega\frac{\partial^2}{\partial q_c^2} - \frac{1}{2}m^{-1}\frac{\partial^2}{\partial \theta^2} \tag{3.33}$$

and potential energy operator with components

$$V_{11}(q_c,\theta) = \frac{1}{2}\omega q_c^2 + \frac{1}{2}W_1\left[1-\cos(\theta)\right], \tag{3.34}$$

$$V_{22}(q_c,\theta) = \frac{1}{2}\omega q_c^2 + \chi_2 q_c + E_2 - \frac{1}{2}W_2\left[1-\cos(\theta)\right], \tag{3.35}$$

$$V_{12}(q_c) = V_{21}(q_c) = \xi q_c. \tag{3.36}$$

Here (all parameters are in eV units), $\omega = 0.19$ is the vibrational frequency of the coupling mode, $m^{-1} = 4.84 \cdot 10^{-4}$ is the inverse mass of the reaction coordinate, $W_1 = 3.6$ and $W_2 = 1.09$ determine the depth of the well in the reaction coordinate for the ground and excited electronic states, respectively, $\chi_2 = 0.1$ is the gradient of the linear perturbation in the excited electronic state, $E_2 = 2.48$ determines the maximum of the excited electronic state in the reaction coordinate, and $\xi = 0.19$ is the gradient of the linear coupling between the two electronic states. The two diabatic potential energy surfaces (3.34) and (3.35) are displayed in Fig. 3.1.

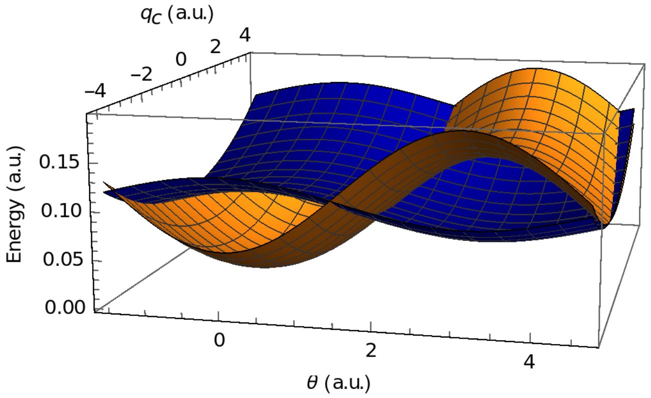

Figure 3.1 – Diabatic potential energy surfaces of the model. Orange: Ground electronic state [Eq. (3.34)]. Blue: Excited electronic state [Eq. (3.35)].

In the simulations, the reaction and coupling coordinates are represented on regular grids consisting of 128 points between $\theta = \pm\pi/2$ a.u. and 64 points between $q_c = \pm 9$ a.u. Figure B.1 of Appendix B confirms that this grid is sufficient by showing that the grid representation of the wavepacket is converged even at the final time t_f. We assume the coordinate independence of the electric dipole moment operator (Condon approximation) and, therefore, can write $\hat{\vec{\boldsymbol{\mu}}} = \vec{\boldsymbol{\mu}}\hat{1} = \vec{\epsilon}\boldsymbol{\mu}\hat{1}$, where $\vec{\epsilon}$ is a constant unit vector in the direction of $\vec{\boldsymbol{\mu}}$. In this case, the control field is aligned with $\vec{\boldsymbol{\mu}}$ and we can write it as $\vec{E}_{\mathrm{LCT}} = \vec{\epsilon}E_{\mathrm{LCT}}$. As a consequence, we can drop the vector symbol $\vec{}$ from $\hat{\vec{\boldsymbol{\mu}}}$ and $\vec{E}_{\mathrm{LCT}}$ in Eqs. (1.20) and (3.14) and consider only the analogous scalar equations satisfied by $\hat{\boldsymbol{\mu}}$ and E_{LCT}. In addition, we assume the electric dipole moment operator to have unit transition elements ($\hat{\mu}_{12} = \hat{\mu}_{21} = \hat{\mu} = 1$ a.u.) and zero diagonal elements ($\hat{\mu}_{11} = \hat{\mu}_{22} = 0$). The calculations presented below aim to simulate the photo-excitation step of the photo-isomerization of the retinal molecule. We therefore use as initial state ψ_0 the ground vibrational state of the harmonic fit of the ground potential energy surface [i.e., a two-dimensional Gaussian wavepacket of the form (2.16), with $D = 2$, space coordinate $x = (q_c, \theta)$, $q_0 = p_0 = (0, 0)$, and $\sigma_0 = (0.128, 1)$ a.u.] with initial populations $P_1(0) = 0.999$ and $P_2(0) = 0.001$ of the ground and excited electronic states, respectively. The tiny initial seed population of the excited state is essential for the control because it ensures that Eq. (1.20) does not stay zero at all times.

Two ways of populating the excited state based on local control theory were investigated: the former used as the target observable the population of the excited state described by the projection operator onto the excited state (i.e., $\hat{\mathbf{O}} = \hat{\mathbf{P}}_2 = \mathbf{P}_2\hat{1} = \mathbf{P}_2$), while the latter employed as the target observable the molecular energy described by the unperturbed molecular Hamiltonian (i.e., $\hat{\mathbf{O}} = \hat{\mathbf{H}}_0$). To show that the monotonic evolution of the target observable $\langle \hat{\mathbf{O}} \rangle_{\psi_t}$ is guaranteed only if $[\hat{\mathbf{O}}, \hat{\mathbf{H}}_0] = 0$, we also compare the results obtained from control calculations in the presence of nonadiabatic couplings (where $[\hat{\mathbf{P}}_2, \hat{\mathbf{H}}_0] \neq 0$ and $[\hat{\mathbf{H}}_0, \hat{\mathbf{H}}_0] = 0$) and in the absence of nonadiabatic couplings (where both target operators $\hat{\mathbf{P}}_2$ and $\hat{\mathbf{H}}_0$ commute with $\hat{\mathbf{H}}_0$). The control calculations were performed by solving the nonlinear time-dependent Schrödinger equation (3.1) with the implicit midpoint algorithm combined with the dynamic Fourier method (Sec. 1.2.5) for a total time $t_f = 256$ a.u. and with a time step $\Delta t = 2^{-3}$ a.u. In addition, intensity parameters $\lambda = 1.430 \times 10^{-2}$ and $\lambda = 1.534 \times 10^{-1}$ were used for the control of excited-state population $P_2(t) := \langle \mathbf{P}_2 \rangle_{\psi_t}$ and molecular energy $E_0(t) := \langle \hat{\mathbf{H}}_0 \rangle_{\psi_t}$, respectively. These parameters were chosen arbitrarily so that the electric fields of the obtained control pulses were similar during the first period and so that their amplitude was not too high, while strong enough to induce a significant increase of the controlled expectation values.

Figure 3.2 shows the excited-state population, molecular energy, and obtained control pulse for the control of either the excited-state population (left panels) or molecular energy (right panels). In the figure, the results obtained in the presence and in the absence of nonadiabatic couplings are also compared for each target. The population and energy control schemes result in similar population dynamics and in

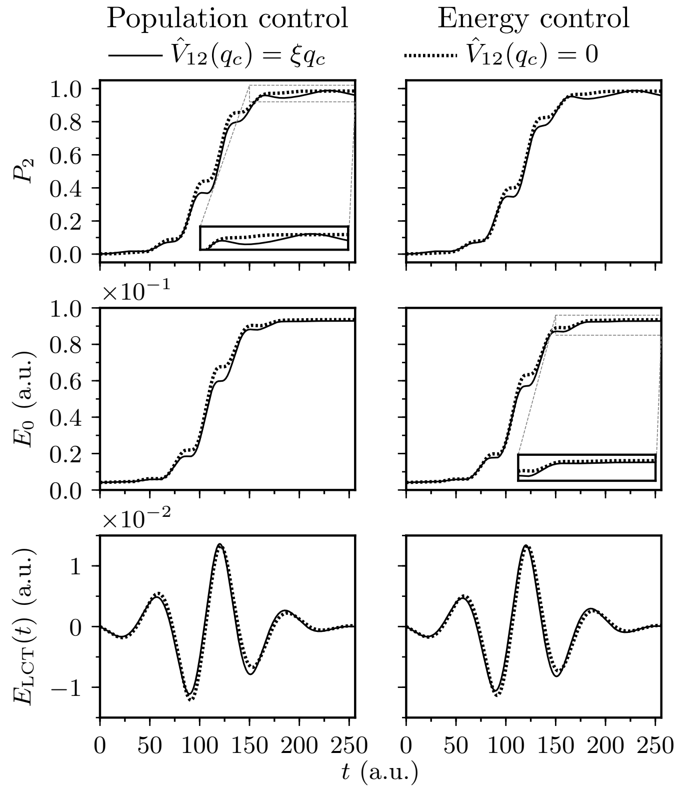

Figure 3.2 – Local control calculations whose goal is increasing either the population $P_2(t)$ of the excited state (left panels, $\lambda = 1.430 \times 10^{-2}$) or the molecular energy $E_0(t)$ (right panels, $\lambda = 1.534 \times 10^{-1}$). As expected, the local control theory applied to these closely related objectives yields very similar results. Top: Excited state population. Middle: Molecular energy. Bottom: Pulse obtained by local control theory.

both schemes, the population of the excited state reaches 0.99 at time t_f. The carrier frequencies of the obtained control pulses are, as expected, similar and correspond to the electronic transition between the two electronic states of the model. As predicted, when controlling the excited-state population $\langle \mathbf{P}_2 \rangle_{\psi_t}$ in the presence of nonadiabatic couplings given by Eq. (3.36), the evolution of the population is not monotonic (see the solid line in the inset of the top left panel of Fig. 3.2) because the control operator does not commute with the molecular Hamiltonian. Compare this with the monotonic increase of the population when the nonadiabatic couplings are zero [dotted line in the same inset; $\hat{V}_{12}(q_c) = \hat{V}_{21}(q_c) = 0$] and the target operator commutes with the molecular Hamiltonian. In contrast, when controlling the molecular energy $\langle \hat{\mathbf{H}}_0 \rangle_{\psi_t}$, its time evolution is always monotonic because the molecular Hamiltonian commutes with itself, whether the nonadiabatic couplings are included or not (see the inset of the middle right-hand panel of Fig. 3.2). Because increasing the population of the excited state has almost the same effect as increasing the molecular energy, very similar dynamics and control pulses are obtained. Yet, the energy and population controls do not always yield similar results. In the retinal model, when performing energy control, no vibrational energy is pumped into the system because the diagonal terms of the electric-dipole moment operator are all zero by construction (hence $\langle[\hat{\boldsymbol{\mu}}, \hat{\mathbf{T}}]\rangle_{\psi_t} = 0$). Consequently, only electronic potential energy is added to the system, and the corresponding control pulse is similar to the one obtained from the population control.

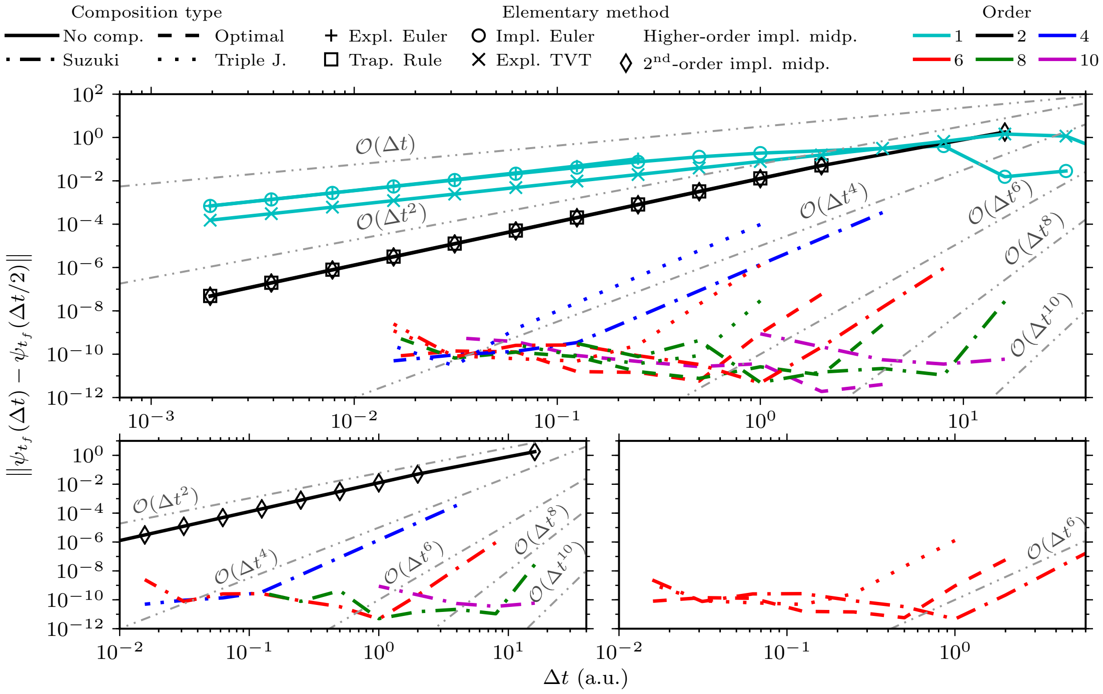

Figure 3.3 – Convergence of the molecular wavefunction at the final time t_f achieved by the local population control in the presence of nonadiabatic couplings. Top: All studied methods, i.e., explicit and implicit Euler methods, approximate explicit TVT split-operator algorithm, trapezoidal rule, implicit midpoint method and its symmetric compositions. Bottom-left: Methods obtained with the Suzuki composition. Bottom-right: Sixth-order methods obtained with different composition schemes.

To verify the orders of convergence predicted in Sec. 3.3.2, we performed convergence analysis of control simulations using various integrators. Simulations with each integrator were repeated with different time steps and the resulting wavefunctions at the final time t_f were compared using Eq. (2.17). Figure 3.3 displays the convergence behavior of both Euler methods, approximate explicit TVT split-operator algorithm, trapezoidal rule, and the proposed implicit midpoint method as well as its symmetric compositions, when controlling the excited state population. Notice that all integrators have their predicted orders of convergence. The approximate explicit TVT split-operator algorithm is, for the reasons mentioned in Sec. 3.3.5, only first-order and not second-order as one might naïvely expect. For the convergence of other simulations, we refer the reader to Figs. B.3–B.5 of Appendix B. Together, these results confirm that both population and energy control follow the predicted order of convergence regardless of the presence of nonadiabatic couplings.

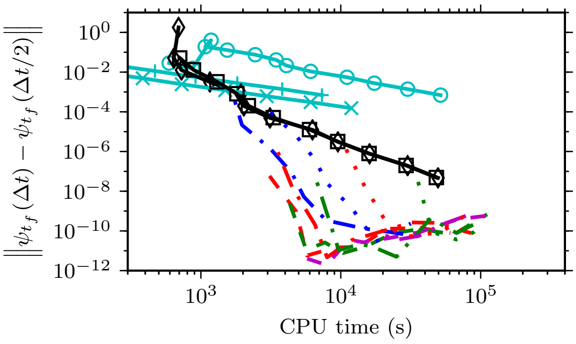

Figure 3.4 – Efficiency of the integrators used for the local population control of retinal in the presence of nonadiabatic couplings. Efficiency is measured by plotting the convergence error as a function of the CPU time. Line labels are the same as in Fig. 3.3.

Because the higher-order methods require more work to perform each step, a higher order of convergence may not guarantee higher efficiency. Therefore, we evaluated the efficiency of each method directly by measuring the CPU time needed to reach a prescribed convergence error. Figure 3.4 shows the convergence error as a function of the CPU time and confirms that, except for very crude calculations, higher-order integrators are more efficient than any of the first- and second-order methods. For example, to reach errors below a rather high threshold of 3×10^{-4}, the fourth-order integrator obtained with the Suzuki composition scheme is already more efficient than any of the first- or second-order algorithms. The efficiency gain increases further when highly accurate results are desired. Indeed, for an error of 10^{-9}, the eighth-order optimal method is 48 times faster than the basic, second-order implicit midpoint method and approximately 400000 times faster than the approximate explicit TVT split-operator algorithm (for which, due to its inefficiency, the speedup had to be estimated by linear extrapolation). High accuracy is hard to achieve with the explicit methods because both the explicit Euler and approximate explicit TVT split-operator algorithms have only first-order convergence. Notice also that the cost of implicit methods is not a monotonous function of the error because the Newton–Raphson method needs more iterations to converge for larger than for smaller time steps. Indeed, for time steps (or errors) larger than a critical value, the CPU time might in fact increase with further increasing time step (or error). The efficiency plots of other control simulations (see Figs. B.6–B.8 of Appendix B) confirm that the increase in efficiency persists regardless of the control target (energy or population) and presence or absence of nonadiabatic couplings.

Figure 3.5 analyzes how the time reversibility and norm conservation depend on the time step. The figure confirms that all proposed integrators are exactly time-reversible and norm-conserving regardless of the time step (the slow increase of the error with decreasing time step is due to the accumulation of numerical roundoff errors because a smaller time steps requires a larger number of steps to reach the same final time t_f). In contrast, the figure shows that an unrealistically small time step would be required for the trapezoidal rule and both Euler methods to conserve norm exactly and for the explicit split-operator algorithm to be exactly time-reversible. Figures B.9–B.11 of Appendix B confirm that neither the chosen control objective nor the nonadiabatic couplings influence the geometric properties of the integrators.

We also checked how the conservation of geometric properties by the integrators depend on time t for a fixed time step. For these simulations, we used a greater final time $t_f = 2048$ a.u. and an intentionally large time step $\Delta t = 2^{-2}$ a.u. The grid was modified to 256 points between $\theta = \pm 3\pi/2$ a.u. and 64 points between $q_c = \pm 9$ a.u., ensuring that the grid representation of the wavefunction at the final time t_f was converged (see Fig. B.2 of Appendix B). Figure 3.6 displays the time evolution of the geometric properties for the elementary integrators (i.e., the trapezoidal rule, implicit midpoint, approximate explicit split-operator, and both Euler methods). The top panel confirms that the implicit midpoint method and the approximate explicit TVT split-operator algorithm conserve the norm exactly (i.e., to machine precision) even though a large time step was used. In contrast, the trapezoidal rule and both Euler methods do not conserve the norm. The second

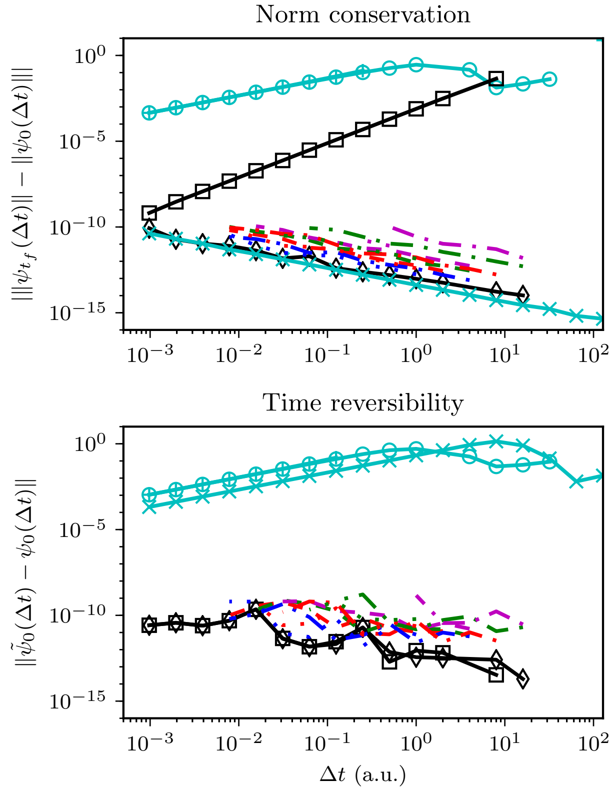

Figure 3.5 – Norm conservation (top) and time reversibility (bottom) of various integrators at the final time t_f as a function of the time step Δt used for the local control of population in the presence of nonadiabatic couplings. Time reversibility is measured by the distance between the initial state ψ_0 and a "forward-backward" propagated state $\tilde{\psi}_0 := \hat{U}(0,t;\psi)\hat{U}(t,0;\psi)\psi_0$ [see Eq. (3.12)] and line labels are the same as in Fig. 3.3.

panel shows that only the trapezoidal rule and the implicit midpoint method are time-reversible. However, due to the nonlinearity of the Schrödinger equation (3.1) and the accumulation of roundoff errors, the time reversibility of these integrators slowly deteriorates as time increases. (For a more detailed analysis of this gradual loss of time reversibility, we refer the reader to Sec. B.4 of Appendix B.) The bottom three panels of Fig. 3.6 confirm that even the implicit midpoint method does not conserve the inner product, distance between two states, and total energy; this is not surprising because, due to nonlinearity, the exact solution does not conserve these properties either. Figures B.12–B.14 of Appendix B also confirm that neither the chosen control objective nor the nonadiabatic couplings influence

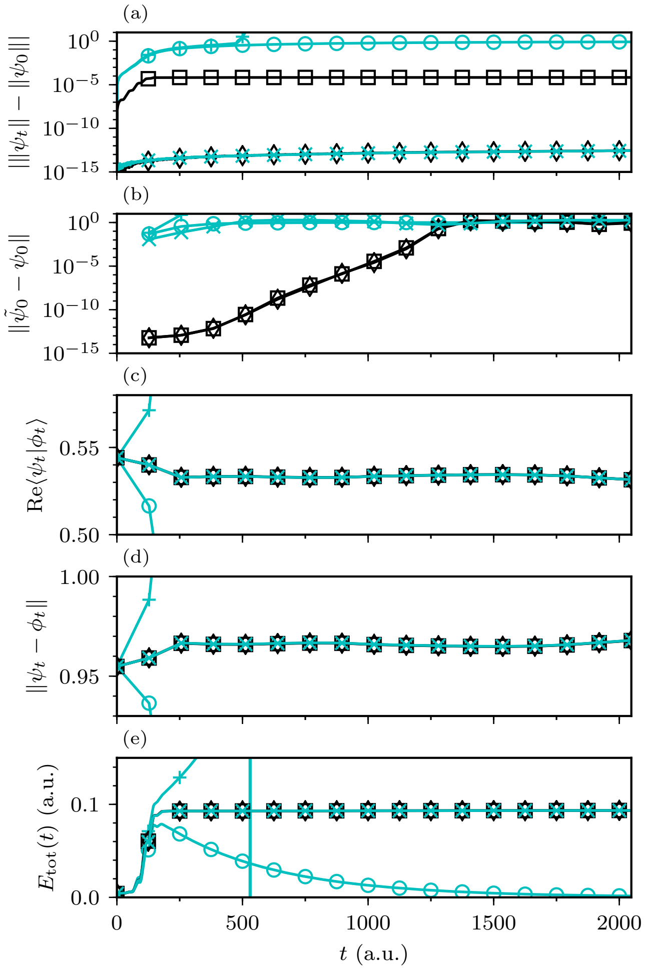

Figure 3.6 – Geometric properties of various integrators used for the local population control in the presence of nonadiabatic couplings. Panel (a) shows that only the implicit midpoint and approximate explicit split-operator methods conserve the norm, while panel (b) demonstrates that only the implicit midpoint method and the trapezoidal rule are time-reversible. (Reversibility is measured as in Fig. 3.5). Bottom three panels show that no method conserves (c) the inner product, (d) distance between two states (which would imply stability), or (e) total energy $E_{\mathrm{tot}}(t) := E_0(t) + \langle \hat{\mathbf{V}}_{\mathrm{LCT}}(\psi_t)\rangle_{\psi_t}$ because even the exact evolution operator does not preserve these properties. State ϕ_0 is ψ_0 displaced along the reaction coordinate, i.e., a two-dimensional Gaussian wavepacket of the form (2.16), with parameters $q_0 = (0.1, 0)$, $p_0 = (0, 0)$, and $\sigma_0 = (0.128, 0)$ a.u. The time step $\Delta t = 2^{-2}$ a.u. was used for all calculations and line labels are the same as in Fig. 3.3. Note that only a few points of the Euler methods are visible in some of the plots because the results of the Euler methods leave the range of these plots very rapidly.

the time evolution of the geometric properties of these integrators.

3.5 Conclusion

We presented high-order time-reversible integrators for the nonlinear time-dependent Schrödinger equation and demonstrated their efficiency and geometric properties on the problem of local control of quantum systems. The basic time-reversible integrator is an adaptation of the implicit midpoint method to the nonlinear Schrödinger equation and is obtained by composing the explicit and implicit Euler methods. It is norm-conserving, symmetric, time-reversible, and of second order of accuracy in the time step. Because it is symmetric, the implicit midpoint method can be composed using symmetric composition methods to obtain integrators of an arbitrary even order of accuracy. These higher-order integrators conserve all the properties of the original second-order method.

In contrast, the explicit TVT split-operator algorithm is generally only an approximate adaptation of the standard second-order TVT split-operator algorithm to the nonlinear Schrödinger equation which results from local control theory. Because this integrator is not implicit, it is only of first order accuracy in the time step and loses time reversibility while still conserving the norm. For instance, the trapezoidal rule, another popular algorithm for solving the Schrödinger equation, remains symmetric and time-reversible, but does not conserve the norm of the wavefunction propagated with a nonlinear Schrödinger equation.

Although we applied the proposed algorithms only to the special case of local control theory, they should also be useful for any nonlinear time-dependent Schrödinger equation if high accuracy, norm conservation, and time reversibility of the solution are desired.

4 An implicit split-operator algorithm for the nonlinear time-dependent Schrödinger equation

We have seen in Chapter 3 that, when applied to certain nonlinear time-dependent Schrödinger equations, the explicit split-operator algorithm loses its time reversibility and second-order accuracy, which makes it very inefficient. Here, we propose to overcome the limitations of the explicit split-operator algorithm by abandoning its explicit nature only. In this regard, we describe a family of high-order implicit split-operator algorithms that are norm-conserving, time-reversible, and very efficient. The geometric properties of the integrators are proven analytically and demonstrated numerically on the local control of a two-dimensional model of retinal. Although they are only applicable to separable Hamiltonians, the implicit split-operator algorithms are, in this setting, more efficient than the integrators based on the implicit midpoint method of Chapter 3.

The content of this Chapter has been adapted from Ref. [167].

4.1 Introduction

To overcome the limitations of the explicit split-operator algorithm applied to general nonlinear time-dependent Schrödinger equations, in Chapter 3 we developed high-order integrators by symmetrically composing the implicit midpoint method. These integrators are applicable to the general nonlinear Schrödinger equation with both separable and nonseparable Hamiltonians and, in contrast to the explicit split-operator algorithm, are efficient, while preserving the geometric properties of the exact solution.

Here, we show that it is not necessary to abandon the split-operator algorithm altogether, but only its explicit nature. In the linear case, the second-order split-operator algorithms are obtained by composing two adjoint first-order split-operator methods, which are both explicit. We show that to achieve a second-order accuracy in the nonlinear case, one of the two adjoint algorithms must be implicit. Although implicit generalizations of the Verlet algorithm exist [88, 91, 168, 169] for classical systems with nonseparable Hamiltonians, to the best of our knowledge no implicit splitting methods were developed for quantum systems with separable but nonlinear Hamiltonians. Therefore, we present an implicit generalization of the second-order split-operator algorithm, which is geometric, applicable to the general nonlinear time-dependent Schrödinger equation, and can be composed with the composition methods [121, 122, 133, 135] of Sec. 2.2.1 to further increase its order of convergence and efficiency.

The remainder of this Chapter is organized as follows: In Sec. 4.2, we present the algorithms, their geometric properties and the procedure employed to perform the implicit propagation required by the implicit split-operator algorithms. In Sec. 4.3, we verify the convergence and the geometric properties of the proposed integrators by performing local control theory on the two-dimensional model of retinal used in Sec. 3.4. Finally, Sec. 4.4 concludes this Chapter.

4.2 Split-operator algorithms for the nonlinear time-dependent Schrödinger equation

In this section, we present the different numerical methods and discuss their geometric properties. Detailed proofs of the geometric properties of the presented numerical methods are shown in Appendix D.1.

4.2.1 Recovery of geometric properties and increasing accuracy by composition

As discussed in Sec. 3.3.5, the explicit TV [Eq. (3.29)] and implicit VT [Eq. (3.30)] split-operator algorithms can be composed together to obtain the implicit TVT algorithm

$$\begin{aligned}\hat{U}_{\mathrm{TVT}}&(t+\Delta t, t; \psi_{t+\Delta t/2})\\ &:= \hat{U}_{\mathrm{TV}}(t+\Delta t, t+\Delta t/2; \psi_{t+\Delta t/2})\\ &\qquad \times \hat{U}_{\mathrm{VT}}(t+\Delta t/2, t; \psi_{t+\Delta t/2})\end{aligned} \tag{4.1}$$

or the implicit VTV algorithm

$$\begin{aligned}\hat{U}_{\mathrm{VTV}}&(t+\Delta t, t; \psi)\\ &:= \hat{U}_{\mathrm{VT}}(t+\Delta t, t+\Delta t/2; \psi_{t+\Delta t})\\ &\qquad \times \hat{U}_{\mathrm{TV}}(t+\Delta t/2, t; \psi_{t}),\end{aligned} \tag{4.2}$$

depending on the order of composition. Both of these integrators are second-order accurate in the time step and geometric because they preserve all the geometric properties of the exact evolution operator, i.e., they are norm-conserving, symmetric, and time-reversible. However, since both rely on the implicit VT split-operator algorithm (3.30), both are implicit methods.

The second-order methods (4.1)–(4.2) are all symmetric and time-reversible regardless of the size of the time step. Therefore, as discussed in Secs. 2.2.1 and 3.3.2, they can be further composed using symmetric composition methods to obtain integrators of arbitrary even orders of convergence.

Note that by "order" we mean the formal order because, as shown by Lubich [170] and Thalhammer [171], who performed rigorous convergence analysis of splitting methods applied to the nonlinear time-dependent Schrödinger equation, the actual order depends on the regularity of the initial state. Because we do not perform this analysis here, we will verify the predicted (formal) order numerically in Sec. 4.3.

4.2.2 Solving the implicit propagation

Both TVT and VTV implicit split-operator algorithms rely on the implicit VT method. Following the procedure described in Sec. 3.3.3, the implicit step of evolution operator $\hat{U}_{VT}$ [Eq. (3.30)] is translated into solving the nonlinear system

$$\hat{U}_{\mathrm{VT}}(t+\Delta t, t; \psi_{t+\Delta t})^{-1}|\psi_{t+\Delta t}\rangle = |\psi_t\rangle. \tag{4.3}$$

This nonlinear system, which we solved employing the Newton–Raphson method, can be written as $f(\psi_{t+\Delta t}) = 0$ with the nonlinear functional

$$\begin{aligned} f(\psi) :&= \hat{U}_{\hat{T}}(\Delta t)[\hat{U}_{\mathrm{VT}}(t+\Delta t, t; \psi)^{-1}\psi - \psi_t] \\ &= \hat{U}_{\hat{T}}(\Delta t)[\hat{U}_{\hat{T}}(\Delta t)^{-1}\hat{U}_{\hat{V}_{\mathrm{tot}}(\psi)}(\Delta t)^{-1}\psi - \psi_t] \\ &= \hat{U}_{\hat{V}_{\mathrm{tot}}(\psi)}(\Delta t)^{-1}\psi - \hat{U}_{\hat{T}}(\Delta t)\psi_t, \end{aligned} \tag{4.4}$$

where we have, for convenience, included a nonzero factor of $\hat{U}_{\hat{T}}(\Delta t)$ into the definition of $f(\psi)$.

As described in Sec. 3.3.3, we employ the solution from the explicit propagation, i.e., the solution obtained using Eq. (3.29), as the initial guess $\psi^{(0)}$. Fortunately, the use of approximations for estimating the Jacobian is, as for the implicit Euler method, avoided because the Jacobian $\hat{J}(\psi)$ of the nonlinear function (4.4) can be obtained analytically:

$$\begin{aligned} \hat{J}(\psi) &= \frac{\delta}{\delta\psi}\left[\hat{U}_{\hat{V}_{\mathrm{tot}}(\psi)}(\Delta t)^{-1}\psi\right] \\ &= \frac{\delta}{\delta\psi}\left[\hat{U}_{\hat{V}_{\mathrm{tot}}(\psi)}(\Delta t)^{-1}\right]\psi + \hat{U}_{\hat{V}_{\mathrm{tot}}(\psi)}(\Delta t)^{-1}\hat{1} \\ &= \frac{i}{\hbar}\Delta t\hat{U}_{\hat{V}_{\mathrm{tot}}(\psi)}(\Delta t)^{-1}\frac{\delta}{\delta\psi}\left[\hat{V}_{\mathrm{LCT}}(\psi)\right]\psi \\ &\qquad + \hat{U}_{\hat{V}_{\mathrm{tot}}(\psi)}(\Delta t)^{-1}\hat{1} \\ &= \hat{U}_{\hat{V}_{\mathrm{tot}}(\psi)}(\Delta t)^{-1}\left[\hat{1} + \frac{i}{\hbar}\Delta t\hat{V}_{\mathrm{LCT}}(\psi)\right], \end{aligned} \tag{4.5}$$

where we employed Eq. (3.28) in the third line.

4.3 Numerical examples

Integrators presented in Sec. 4.2 were tested on a local control simulation in the two-dimensional model describing the *cis-trans* photo-isomerization of retinal (see Fig. 3.1).

In all simulations, we used local control theory for increasing the molecular energy $E_0(t) = \langle\hat{\mathbf{H}}_0\rangle_{\psi_t}$ of the system, which required employing the molecular energy operator $\hat{\mathbf{H}}_0$ as the target observable. First, we reproduced the simulation depicted in the right panel of Fig. 3.2 (the one including the nonadiabatic couplings) using

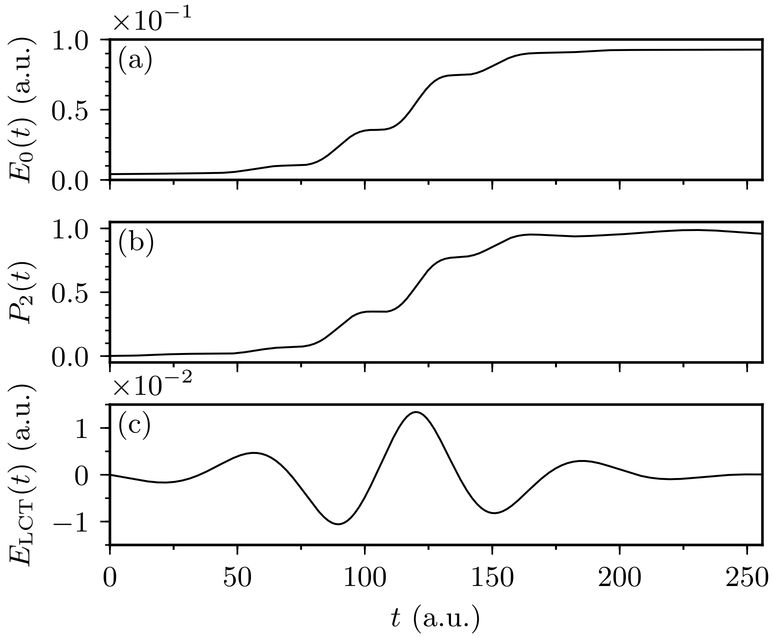

Figure 4.1 – Local control simulation whose goal is increasing the molecular energy $E_0(t)$. (a) Molecular energy. (b) Excited state population. (c) Pulse obtained by local control theory.

the implicit TVT split-operator algorithm instead of the implicit midpoint method. Since we used the same parameters, the results obtained with the implicit TVT split-operator algorithm, which are shown in Fig. 4.1, are thus similar to those depicted in the right panel of Fig. 3.2. Indeed, the results indicate a successful increase in molecular energy [panel (a)] and, as predicted in Sec. 1.1.3, this increase is monotonic because the molecular energy operator commutes with itself. Moreover, because there are no nonzero diagonal elements in the electric dipole moment operator, the control pulse cannot add vibrational energy ($\langle [\hat{\boldsymbol{\mu}}, \hat{\mathbf{T}}] \rangle_{\psi_t} = 0$). Consequently, only the electronic energy of our system is increased, as reflected by the monotonic rise of the excited state population $P_2(t)$ [panel (b)]; this is confirmed by the carrier frequency of the control pulse [panel (c)], which corresponds to an electronic transition between the two states.

To verify the order of convergence of the integrators presented in Sec. 4.2, the same simulation was repeated for each integrator with different time steps, and the errors in the obtained wavefunctions were compared, using Eq. (2.17), at the final time $t_f = 256$ a.u. Figure 4.2 shows the convergence behavior of various integrators, including higher-order integrators obtained by composing the implicit TVT method

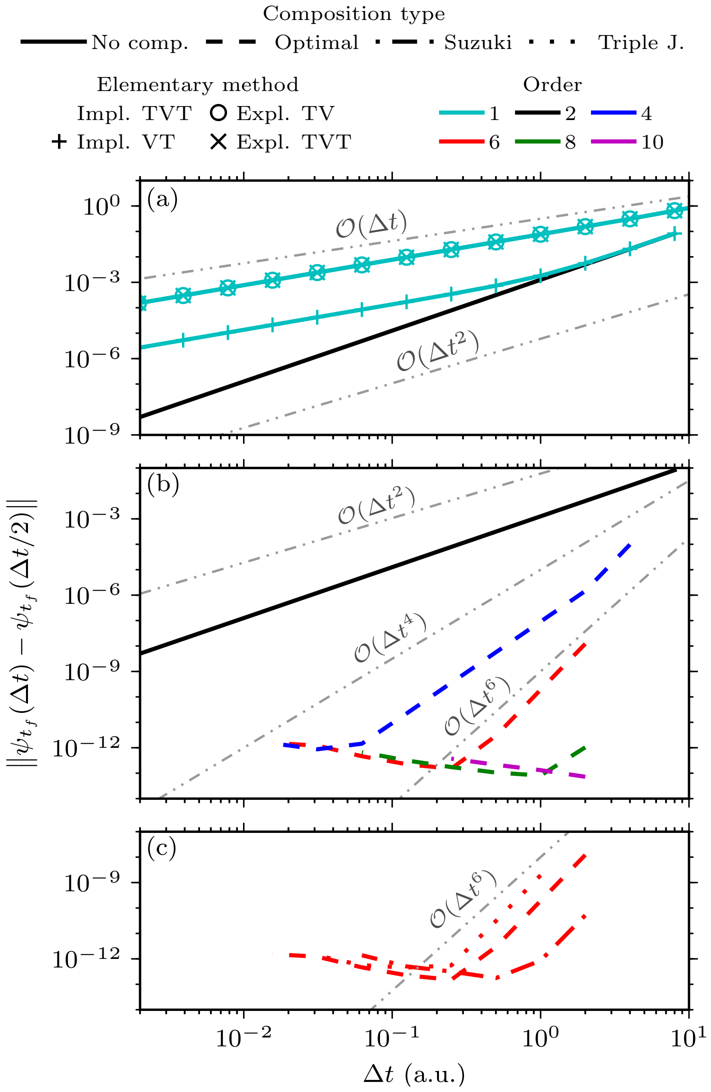

Figure 4.2 – Convergence of the molecular wavefunction at the final time $t_f = 256$ a.u. achieved by the local energy control. (a) First-order and implicit TVT methods. (b) Methods obtained with the optimal composition (Suzuki's fractal is the optimal fourth-order composition scheme [104]). (c) Sixth-order methods obtained with different composition schemes.

with the triple-jump, Suzuki's fractal, and optimal composition schemes (see also Fig. D.1 of Appendix D.2, which displays the convergence results for all studied methods). The results in panel (a) indicate that the implicit TVT method has the expected order of convergence and that it is, for a given time step, more accurate than all first-order methods, including the approximate explicit TVT algorithm. Comparison between different orders of the optimal composition of the implicit

TVT algorithm [panel (b)] shows that, for a given time step, a higher order of composition yields more accurate integrators. Similarly, comparing sixth-order methods obtained with different composition schemes [panel (c)] indicates that, for a given time step, Suzuki's fractal composition is more accurate than both the optimal and triple-jump compositions. Note that after reaching a machine precision plateau, the higher-order integrators show a slight increase in the error with a decreasing time step, which is due to the accumulation of roundoff errors since the number of steps increases for a fixed total time of simulation. Moreover, some results for high-order integrators could not be obtained because they did not converge at large time steps (the difference between the initial guess and the implicit solution was too large for the Newton–Raphson method to converge) and became computationally unaffordable at smaller time steps, when the Newton–Raphson method was converging.

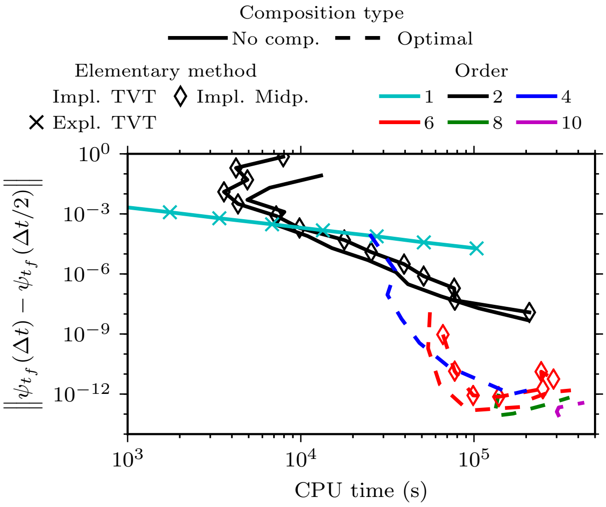

Figure 4.3 – Efficiency of various integrators used for simulating the local energy control of retinal up to the final time $t_f = 256$ a.u.

To check that greater accuracy for a given time step is not detrimental to efficiency, in Fig. 4.3 we plot the dependence of errors of the wavefunctions obtained by various methods on the CPU time (see also Fig. D.2 of Appendix D.2, which displays the efficiency results for all studied methods). Note that the results displayed in Fig. 4.3 should not be compared with the efficiency results of Chapter 3, as they were obtained using a different machine.

Figure 4.3 demonstrates that, if high accuracy is desired, the higher-order integrators are more efficient even though they require performing many substeps at each time step. For example, below an error of 3×10^{-4}, the second-order implicit TVT split-operator algorithm is already more efficient than the approximate explicit TVT split-operator algorithm. Figure 4.3 also shows that the implicit TVT split-operator algorithm is more efficient than the implicit midpoint method, indicating that the implicit split-operator algorithm is the method of choice for separable Hamiltonians and that the implicit midpoint method should only be used when the Hamiltonian is not separable. Indeed, for errors below 7×10^{-4}, the TVT split-operator algorithm is more efficient than the implicit midpoint method. Moreover, the sixth-order composition of the TVT split-operator algorithm is always more efficient than the corresponding composition of the implicit midpoint method, indicating that the improved efficiency of the TVT split-operator algorithm survives when composition methods are employed.

In Fig. 4.4, we checked the preservation of geometric properties by the implicit and approximate explicit TVT methods as a function of time (see Fig. D.3 of Appendix D.2 for a version of this figure which displays the results for all the elementary methods). Note that these results were obtained by employing the same parameters as those used for obtaining Fig. 3.6 (i.e., the same final time, time step, and grid). The results show that while both the implicit and approximate explicit TVT integrators conserve the norm [panel (a)], only the implicit TVT method is time-reversible [panel (b)]. However, due to the nonlinearity of the time-dependent Schrödinger equation and the accumulation of roundoff errors, one observes a gradual loss of time reversibility as the time increases (see Appendix B.4 for a detailed analysis of this loss of time-reversibility). The bottom three panels of Fig. 4.4 (and Fig. D.3 of Appendix D.2) demonstrate that none of the methods conserves the inner product [panel (c)], distance between two states [panel (d)], or total energy [panel (e)], because these properties are not conserved even by the exact nonlinear evolution operator (3.4).

Finally, Fig. 4.5 analyzes the norm conservation [panel (a)] and time reversibility [panel (b)] of various integrators at the final time $t_f = 256$ a.u. as a function of the time step (see Fig. D.4 of Appendix D.2 for a version of this figure with all the studied methods). As expected, all the integrators presented in Sec. 4.2 conserve the norm, regardless of the time step. Whereas the first-order integrators are irreversible (the time reversibility is satisfied only to the first order in the time step), the implicit midpoint, VTV and TVT methods as well as compositions of

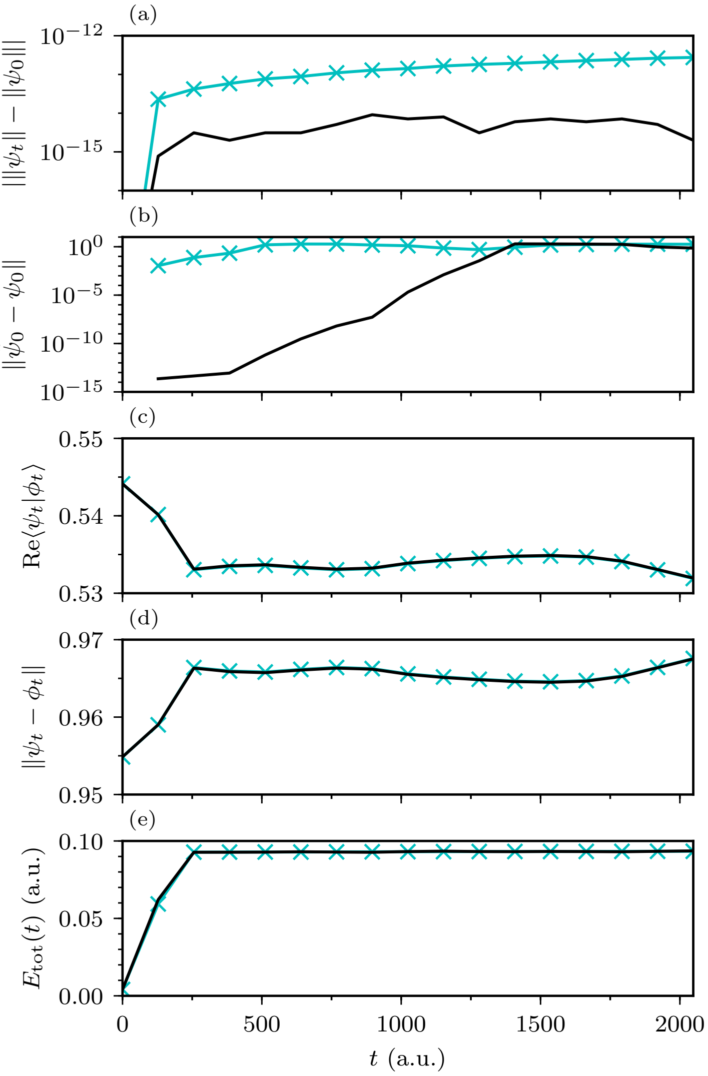

Figure 4.4 – Time dependence of the geometric properties of the implicit and approximate explicit TVT methods used for simulating the local energy control up to the final time $t_f = 2048$ a.u. (a) Norm of the wavefunction. (b) Time reversibility. (c) Inner product. (d) Distance between two states (conservation of this distance would imply stability). (e) Total energy. Time reversibility is measured by the distance between the initial state ψ_0 and a "forward-backward" propagated state $\tilde{\psi}_0$ [see Fig. 3.5 and Eq. (3.12)]. The state ϕ_0 is the same as the one used in Fig. 3.5 and line labels are the same as in Fig. 4.2.

the latter are time-reversible for all time steps.

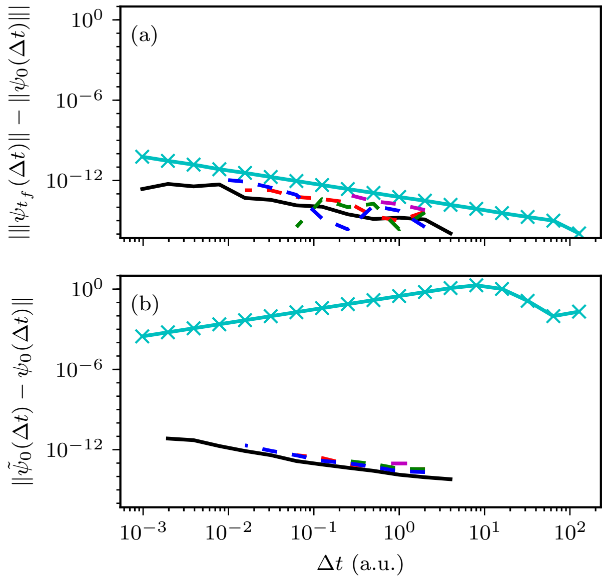

Figure 4.5 – Norm conservation (a) and time reversibility (b) of various integrators at the final time $t_f = 256$ a.u. as a function of the time step Δt used for the local energy control of retinal. Reversibility is measured as in Fig. 4.4 and line labels are the same as in Fig. 4.2.

4.4 Conclusion

We presented high-order integrators for solving the nonlinear time-dependent Schrödinger equation with separable Hamiltonians. In contrast to their first-order explicit versions, the proposed methods, obtained by composing an implicit split-operator algorithm, preserve all geometric properties of the exact solution, i.e., they are symmetric, time-reversible, and norm-conserving. Moreover, the proposed integrators are more efficient than both the explicit split-operator algorithm and the compositions based on the implicit midpoint method.

5 Conclusions and outlook

In this thesis, we employed composition methods to increase the efficiency of standard numerical methods employed for solving linear and nonlinear time-dependent Schrödinger equations.

As stated earlier, the standard split-operator algorithm, which is often used to solve the time evolution of a state driven by a separable Hamiltonian, is only second-order accurate, despite conserving many geometric properties of the exact solution. Using composition methods, we increased its order of convergence to arbitrary even order and provided a strategy to reduce the cost and memory needs of the composed methods. By solving the nonadiabatic dynamics on a one-dimensional model of NaI, we demonstrated that the high-order integrators are very efficient if highly accurate wavefunctions are needed and preserve all the geometric properties of the original second-order split-operator algorithm. Moreover, using a three-dimensional model of pyrazine, we demonstrated that the efficiency of the high-order integrators is retained in higher dimensions.

As for local control theory, this thesis demonstrated that this technique translates into a nonlinear time-dependent Schrödinger equation for which the explicit split-operator algorithm is only first-order accurate and does not preserve the time-reversal symmetry. Indeed, although this algorithm is geometric and second-order accurate for simple nonlinearities, such as the one appearing in the Gross–Pitaevskii equation, it fails to preserve these properties when the nonlinearity is more complicated. Thus, to remedy this lack of generality, we showed that the explicit nature of the split-operator algorithm, which is an appealing property, must be abandoned. To this end, we adapted the implicit midpoint for the nonlinear case and used local control simulations on a two-dimensional model of retinal to demonstrate that despite being implicit, the developed method is geometric and second-order accurate, in contrast to the explicit split-operator algorithm. Additionally, the developed method applies to both separable and nonseparable Hamiltonians, and because it is symmetric, its efficiency can be further increased using composition methods.

Finally, we have seen that to recover the geometric properties of the exact nonlinear evolution operator, it is not necessary to abandon the split-operator algorithm completely, but only its explicit nature. In this regard, we have developed an implicit split-operator algorithm that is geometric, second-order, and applicable to the general nonlinear Hamiltonian. However, the obtained integrator is only applicable in the diabatic representation, for which the Hamiltonian is separable. Even so, in this situation, the developed method is more efficient than the nonlinear integrator based on the implicit midpoint method.

Together, these results provide a general methodology for obtaining efficient high-order integrators. Indeed, employing the composition methods on any symmetric algorithm will lead to numerical methods of an arbitrary even order of convergence that possess the same geometric properties as the original noncomposed method.

Moreover, the accurate solutions obtained from these algorithms are valuable because they can efficiently provide very accurate exact benchmarks, which are helpful, e.g., in endeavors such as identifying the error induced by a novel, more approximate method and defining its range of validity.

For example, one possible application of this work would include employing the same composition methods to solve the dynamics within various semiclassical methods, such as the thawed [29–32] or variational [33, 34] Gaussian approximation. These methods are crude approximations of the exact solution but remain valid for a short time and are suitable for ab-initio dynamics. When employed in this setting, the bottleneck of these methods is the local potential energy information, which is provided by electronic structure calculations. Therefore, one could use the composition methods to eliminate the error from the time propagation entirely and focus only on the accuracy of the approximation. In this way, the composition methods would allow obtaining the exact result (within the approximation) with larger time steps and fewer potential energy evaluations than with the standard second-order Verlet integrator typically used.

Because they apply to any nonlinear time-dependent Schrödinger equation, the developed nonlinear integrators could be employed to solve that equation in any other method where it appears. For example, the equations of motion of the multiconfigurational time-dependent Hartree method are nonlinear and the constant mean field scheme [172, 173], which is often used for the propagation, is only second-order accurate. Thus, by using the nonlinear integrators presented in this thesis, its accuracy and efficiency could be further improved.

To conclude, the results presented in this thesis have broad implications in molecular dynamics. For instance, they help increase the efficiency and accuracy of existing methods and facilitate the development of novel techniques, thus, allowing a better understanding of the molecular nonadiabatic dynamics.

A Supporting information for Chapter 2

A.1 Local error and geometric properties

To simplify many expressions, we set $\hbar = 1$ and denote the increment Δt with ϵ throughout this appendix. The $\hbar$ can be reintroduced by replacing each occurrence of t with $t/\hbar$ (and ϵ with $\epsilon/\hbar$). To analyze geometric properties of various integrators, we will use several well-known identities satisfied by the Hermitian adjoint and inverse operators:

Proposition 1. *Let $\hat{A}$ and $\hat{B}$ be invertible operators on a Hilbert space, and let $\hat{A}^\dagger$ and $\hat{B}^\dagger$ be their Hermitian adjoints. Then both $\hat{A}^\dagger$ and $\hat{A}\hat{B}$ are invertible and the following identities hold:*

$$\begin{aligned} (\hat{A}^\dagger)^{-1} &= (\hat{A}^{-1})^\dagger, && \text{(A.1)} \\ (\hat{A}\hat{B})^{-1} &= \hat{B}^{-1}\hat{A}^{-1}, && \text{(A.2)} \\ (\hat{A}\hat{B})^\dagger &= \hat{B}^\dagger\hat{A}^\dagger, && \text{(A.3)} \\ (\hat{A}^\dagger)^\dagger &= (\hat{A}^{-1})^{-1} = \hat{A}. && \text{(A.4)} \end{aligned}$$

The first identity shows that the Hermitian adjoint and inverse operations are commutative, while the last three properties indicate that these two operations are involutive antiautomorphisms on the group of invertible operators [90, 174].

A.1.1 Local error

The local error of an approximate evolution operator, defined as $\hat{U}_{\text{appr}}(\epsilon) - \hat{U}(\epsilon)$, is typically analyzed by comparing the Taylor expansion of $\hat{U}_{\text{appr}}(\epsilon)$ with the Taylor expansion of the exact evolution operator:

$$\hat{U}(\epsilon) = 1 - i\epsilon(\hat{T} + \hat{V}_0) - \frac{1}{2}\epsilon^2(\hat{T} + \hat{V}_0)^2 + \mathcal{O}(\epsilon^3). \tag{A.5}$$

If the local error is $\mathcal{O}(\epsilon^{n+1})$, the method is said to be of order n because the global error for a finite time $t = P\epsilon$ is $\mathcal{O}(\epsilon^n)$.

The Taylor expansion of the TV algorithm (1.25) is

$$\begin{aligned}\hat{U}_{\text{TV}}(\epsilon) &= \left(1 - i\epsilon\hat{T} - \frac{1}{2!}\epsilon^2\hat{T}^2\right)\left(1 - i\epsilon\hat{V}_0 - \frac{1}{2!}\epsilon^2\hat{V}_0^2\right) + \mathcal{O}(\epsilon^3)\\ &= 1 - i\epsilon(\hat{T} + \hat{V}_0) - \frac{1}{2}\epsilon^2(\hat{T}^2 + 2\hat{T}\hat{V}_0 + \hat{V}_0^2) + \mathcal{O}(\epsilon^3)\\ &= \hat{U}(\epsilon) + \frac{1}{2}\epsilon^2[\hat{V}_0, \hat{T}] + \mathcal{O}(\epsilon^3),\end{aligned} \tag{A.6}$$

so the leading order local error is $\epsilon^2[\hat{V}_0, \hat{T}]/2$. Likewise, for the VT algorithm (1.26),

$$\hat{U}_{\text{VT}}(\epsilon) = \hat{U}(\epsilon) - \frac{1}{2}\epsilon^2[\hat{V}_0, \hat{T}] + \mathcal{O}(\epsilon^3). \tag{A.7}$$

The Taylor expansions of the second-order TVT and VTV algorithms are obtained by composing Taylor expansions (A.6) and (A.7) for time steps $\epsilon/2$:

$$\begin{aligned}\hat{U}_{\text{TVT}}(\epsilon) = \hat{U}_{\text{VTV}}(\epsilon) &= \hat{U}\left(\frac{\epsilon}{2}\right)\hat{U}\left(\frac{\epsilon}{2}\right) + \frac{1}{8}\epsilon^2\left([\hat{V}_0, \hat{T}] - [\hat{V}_0, \hat{T}]\right) + \mathcal{O}(\epsilon^3)\\ &= \hat{U}\left(\epsilon\right) + \mathcal{O}(\epsilon^3),\end{aligned} \tag{A.8}$$

demonstrating that both TVT and VTV are second-order algorithms.

A.1.2 Unitarity, symplecticity, and stability

Both first-order split-operator algorithms are unitary because

$$\begin{aligned}\hat{U}_{\mathrm{TV}}(\epsilon)^{-1} &= e^{i\epsilon\hat{V}_0}e^{i\epsilon\hat{T}} = \hat{U}_{\mathrm{TV}}(\epsilon)^{\dagger},\\ \hat{U}_{\mathrm{VT}}(\epsilon)^{-1} &= e^{i\epsilon\hat{T}}e^{i\epsilon\hat{V}_0} = \hat{U}_{\mathrm{VT}}(\epsilon)^{\dagger}.\end{aligned}$$

Both second-order split-operator algorithms are unitary because they are compositions of unitary first-order algorithms.

Because the symplectic form was defined in Sec. 1.1.1 as the imaginary part of the inner product and because VT, TV, VTV, and TVT algorithms as well as their compositions are unitary, all of them are also symplectic.

Stability follows from unitarity because

$$\|\psi(t+\epsilon) - \phi(t+\epsilon)\| = \|\psi(t) - \phi(t)\| \tag{A.9}$$

for unitary evolution operator $\hat{U}_{\mathrm{appr}}(\epsilon)$. Since all split-operator methods are unitary, all are stable as well.

A.1.3 Commutation of the evolution operator with the Hamiltonian and conservation of energy

Because the kinetic and potential energy operators do not commute, unless $\hat{V}_0 =$ const, the evolution operator of no split-operator algorithm commutes with the Hamiltonian. E.g., for the TV algorithm,

$$[\hat{H}, \hat{U}_{\mathrm{TV}}(\epsilon)] = [\hat{T}+\hat{V}_0, e^{-i\epsilon\hat{T}}e^{-i\epsilon\hat{V}_0}] = e^{-i\epsilon\hat{T}}[\hat{T}, e^{-i\epsilon\hat{V}_0}] + [\hat{V}_0, e^{-i\epsilon\hat{T}}]e^{-i\epsilon\hat{V}_0} \neq 0. \tag{A.10}$$

As a consequence, split-operator algorithms do not conserve energy.

A.1.4 Symmetry and time reversibility

As shown, e.g., in Refs. [88, 91, 104], the adjoint of an evolution operator satisfies the following properties:

$$(\hat{U}(\epsilon)^*)^* = \hat{U}(\epsilon), \tag{A.11}$$

$$(\hat{U}_1(\epsilon)\hat{U}_2(\epsilon))^* = \hat{U}_2(\epsilon)^*\hat{U}_1(\epsilon)^*, \tag{A.12}$$

$$\hat{U}(\epsilon)\hat{U}(\epsilon)^* \text{ is symmetric.} \tag{A.13}$$

Note that the third property gives a simple recipe for developing symmetric methods—by composing an arbitrary method and its adjoint, with both composition coefficients of 1/2.

The first-order VT and TV split-operator algorithms are adjoints of each other because

$$\hat{U}_{\mathrm{TV}}(-\epsilon)^{-1} = e^{-i\epsilon\hat{V}_0}e^{-i\epsilon\hat{T}} = \hat{U}_{\mathrm{VT}}(\epsilon) \tag{A.14}$$

and because of Eq. (A.11). Therefore, neither VT or TV algorithm is symmetric or time-reversible. In contrast, the second-order VTV and TVT algorithms are both symmetric, which follows from Eq. (A.13) applied to the two possible compositions of the VT and TV algorithms with composition coefficients 1/2. As shown, e.g., in Refs. [88, 91, 104], time reversibility follows from symmetry. Therefore, both VTV and TVT algorithms and their symmetric compositions are time-reversible.

A.2 Exponential convergence with grid density

The top panel of Fig. A.1 exhibits the exponential convergence of the molecular wavefunction with the increasing number of grid points for the NaI model in the diabatic basis. The ranges as well as the densities of both the position and momentum grids were increased by a factor of $\sqrt{2}$ for each increase in the number N_{grid} of grid points by a factor of two. Convergence error required comparing wavefunctions on grids with different densities, which was carried out by trigonometric interpolation of the wavefunction on the sparser grid. Increasing N_{grid} reduces the convergence error at time t_f (top panel) because the errors of both the required overlap integral and of the propagation decrease. To compare these two effects, the bottom panel of Fig. A.1 shows the ratio of the purely integration error and

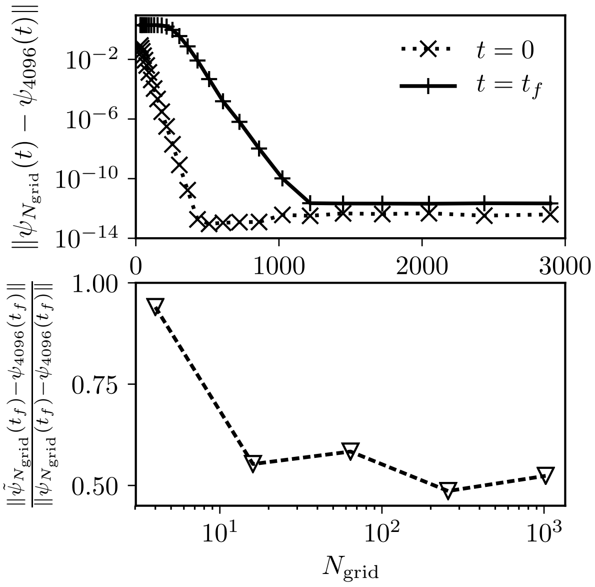

Figure A.1 – Top: Convergence of the initial and final wavepackets with the increasing number of grid points. Bottom: Ratio of the integration error and total convergence error at the final time as a function of the number of grid points. (See Appendix A.2 for details.) The sixth-order optimal composition of the VTV algorithm with time step $\Delta t = t_f/2^7$ was used for the propagation.

the total error. The integration error is defined as $\|\tilde{\psi}_{N_{\rm grid}}(t_f) - \psi_{4096}(t_f)\|$ where $\psi_{4096}(t_f)$ is the wavefunction propagated on the fully converged grid and $\tilde{\psi}_{N_{\rm grid}}(t_f)$ is $\psi_{4096}(t_f)$ represented with $N_{\rm grid}$ grid points. In other words, the representation on a reduced grid is done only after propagation. The panel shows that at the final time, the integration error is approximately one half of the total error. Therefore, the integration and propagation errors due to a finite grid are similar.

B Supporting information for Chapter 3

B.1 Geometric properties of nonlinear numerical integrators

Here, we verify which geometric properties of the exact evolution are preserved by various integrators. The analysis generalizes the analysis from Appendix A of Ref. [104] for the linear to the nonlinear Schrödinger equation. To simplify the proofs, wherever it is not ambiguous, we shall use abbreviated notation $\hat{U}_{\text{appr}}(\psi) := \hat{U}_{\text{appr}}(t + \Delta t, t; \psi)$ for the evolution operator for a single time step and $\epsilon := \Delta t/\hbar$ for the time step divided by Planck's constant.

B.1.1 Norm conservation

In general, the norm is conserved if and only if

$$\hat{U}_{\text{appr}}(\psi)^{\dagger}\hat{U}_{\text{appr}}(\psi) = 1,$$

which follows from a derivation analogous to Eq. (3.8) for the exact operator $\hat{U}(\psi)$. As in the linear case, neither Euler method conserves the norm because

$$\begin{aligned}\hat{U}_{\text{expl}}(\psi_t)^{\dagger}\hat{U}_{\text{expl}}(\psi_t) &= [1 + i\epsilon\hat{H}(\psi_t)][1 - i\epsilon\hat{H}(\psi_t)] \\ &= 1 + \epsilon^2\hat{H}(\psi_t)^2 \neq 1 \qquad \text{(B.1)}\end{aligned}$$

and

$$\begin{aligned}
&\hat{U}_{\mathrm{impl}}(\psi_{t+\Delta t})^{\dagger}\hat{U}_{\mathrm{impl}}(\psi_{t+\Delta t}) \\
&\qquad = [1 - i\epsilon\hat{H}(\psi_{t+\Delta t})]^{-1}[1 + i\epsilon\hat{H}(\psi_{t+\Delta t})]^{-1} \\
&\qquad = [1 + \epsilon^{2}\hat{H}(\psi_{t+\Delta t})^{2}]^{-1} \neq 1.
\end{aligned} \tag{B.2}$$

The trapezoidal rule, norm-conserving in the linear case, loses this property for nonlinear Hamiltonians since

$$\begin{aligned}
&\hat{U}_{\mathrm{trap}}(\psi)^{\dagger}\hat{U}_{\mathrm{trap}}(\psi) \\
&\quad = [1 + i\epsilon\hat{H}(\psi_{t})/2][1 - i\epsilon\hat{H}(\psi_{t+\Delta t})/2]^{-1} \\
&\qquad \times [1 + i\epsilon\hat{H}(\psi_{t+\Delta t})/2]^{-1}[1 - i\epsilon\hat{H}(\psi_{t})/2] \\
&\quad = [1 + i\epsilon\hat{H}(\psi_{t})/2][1 + \epsilon^{2}\hat{H}(\psi_{t+\Delta t})^{2}/4]^{-1} \\
&\qquad \times [1 - i\epsilon\hat{H}(\psi_{t})/2] \\
&\quad \neq 1;
\end{aligned} \tag{B.3}$$

the last nontrivial expression does not reduce to 1 because $\hat{H}(\psi_t) \neq \hat{H}(\psi_{t+\Delta t})$. In contrast, both the implicit midpoint and approximate explicit TVT split-operator algorithms conserve the norm even in the nonlinear setting because

$$\begin{aligned}
&\hat{U}_{\mathrm{mid}}(\psi_{t+\Delta t/2})^{\dagger}\hat{U}_{\mathrm{mid}}(\psi_{t+\Delta t/2}) \\
&\quad = [1 - i\epsilon\hat{H}(\psi_{t+\Delta t/2})/2]^{-1}[1 + i\epsilon\hat{H}(\psi_{t+\Delta t/2})/2] \\
&\qquad \times [1 - i\epsilon\hat{H}(\psi_{t+\Delta t/2})/2][1 + i\epsilon\hat{H}(\psi_{t+\Delta t/2})/2]^{-1} \\
&\quad = 1
\end{aligned} \tag{B.4}$$

(where in the last step we used the commutativity of the middle two factors in the previous expression) and

$$\begin{aligned}
&\hat{U}_{\mathrm{expl\ TVT}}(\psi_{t,\hat{T}\Delta t/2})^{\dagger}\hat{U}_{\mathrm{expl\ TVT}}(\psi_{t,\hat{T}\Delta t/2}) \\
&\quad = e^{i\epsilon\hat{T}/2}e^{i\epsilon\hat{V}_{\mathrm{tot}}(\psi_{t,\hat{T}\Delta t/2})}e^{i\epsilon\hat{T}/2} \\
&\qquad \times e^{-i\epsilon\hat{T}/2}e^{-i\epsilon\hat{V}_{\mathrm{tot}}(\psi_{t,\hat{T}\Delta t/2})}e^{-i\epsilon\hat{T}/2} \\
&\quad = 1.
\end{aligned} \tag{B.5}$$

B.1.2 Symmetry and time reversibility

Neither Euler method is symmetric nor time-reversible because they are adjoints of each other:

$$\begin{aligned}\hat{U}_{\text{expl}}(t+\Delta t, t; \psi_t)^* &= \hat{U}_{\text{expl}}(t, t+\Delta t; \psi_{t+\Delta t})^{-1} \\ &= [1 - i(-\Delta t)\hat{H}(\psi_{t+\Delta t})/\hbar]^{-1} \\ &= \hat{U}_{\text{impl}}(t+\Delta t, t; \psi_{t+\Delta t}). \qquad \text{(B.6)}\end{aligned}$$

The approximate explicit TVT split-operator algorithm is also time-irreversible because forward propagation is not cancelled by backward propagation:

$$\begin{aligned}&\hat{U}_{\text{expl TVT}}(t; t+\Delta t, \psi_{\hat{V}\hat{T}})\hat{U}_{\text{expl TVT}}(t+\Delta t; t, \psi_{t,\hat{T}\Delta t/2}) \\ &\quad = e^{i\epsilon\hat{T}/2} e^{i\epsilon\hat{V}_{\text{tot}}(\psi_{\hat{V}\hat{T}})} e^{i\epsilon\hat{T}/2} \\ &\qquad \times e^{-i\epsilon\hat{T}/2} e^{-i\epsilon\hat{V}_{\text{tot}}(\psi_{t,\hat{T}\Delta t/2})} e^{-i\epsilon\hat{T}/2} \\ &\quad \neq 1, \qquad \text{(B.7)}\end{aligned}$$

where $\psi_{\hat{V}\hat{T}} := e^{i\epsilon\hat{T}/2}\psi_{t+\Delta t} = e^{-i\epsilon\hat{V}_{\text{tot}}(\psi_{t,\hat{T}\Delta t/2})}\psi_{t,\hat{T}\Delta t/2}$ denotes the state obtained after forward propagation of $\psi_{t,\hat{T}\Delta t/2}$ with the potential evolution operator and $\hat{V}_{\text{tot}}(\psi_{\hat{V}\hat{T}}) \neq \hat{V}_{\text{tot}}(\psi_{t,\hat{T}\Delta t/2})$ was used to obtain the last line. It is clear from Eq. (B.7) that if the nonlinear term is as in the Gross-Pitaevskii equation, i.e., if $V_{\text{tot}}(\psi, q) = V_0(q) + C|\psi(q)|^2$ with C a real constant, the approximate explicit TVT split-operator algorithm becomes time-reversible because $\hat{V}_{\text{tot}}(\psi_{\hat{V}\hat{T}}) = \hat{V}_{\text{tot}}(\psi_{t,\hat{T}\Delta t/2})$ in that particular case; the reason is that wavefunctions $\psi_{\hat{V}\hat{T}}(q)$ and $\psi_{t,\hat{T}\Delta t/2}(q)$ in position representation only differ by a position-dependent phase factor. However, the equality $\hat{V}_{\text{tot}}(\psi_{\hat{V}\hat{T}}) = \hat{V}_{\text{tot}}(\psi_{t,\hat{T}\Delta t/2})$ does not hold for other nonlinear Hamiltonians, such as the one in local control theory, which contains a more general nonlinearity.

In contrast, both the implicit midpoint method and trapezoidal rule are always time-reversible because they are symmetric:

$$\begin{aligned}
&\hat{U}_{\mathrm{mid}}(t+\Delta t, t; \psi_{t+\Delta t/2})^{*} = \hat{U}_{\mathrm{mid}}(t, t+\Delta t; \psi_{t+\Delta t/2})^{-1} \\
&\quad = \left\{[1 + i\epsilon\hat{H}(\psi_{t+\Delta t/2})/2][1 - i\epsilon\hat{H}(\psi_{t+\Delta t/2})/2]^{-1}\right\}^{-1} \\
&\quad = [1 - i\epsilon\hat{H}(\psi_{t+\Delta t/2})/2][1 + i\epsilon\hat{H}(\psi_{t+\Delta t/2})/2]^{-1} \\
&\quad = \hat{U}_{\mathrm{mid}}(t+\Delta t, t; \psi_{t+\Delta t/2}),
\end{aligned} \tag{B.8}$$

and

$$\begin{aligned}
&\hat{U}_{\mathrm{trap}}(t+\Delta t, t; \psi)^{*} = \hat{U}_{\mathrm{trap}}(t, t+\Delta t; \psi)^{-1} \\
&\quad = \left\{[1 - i\epsilon\hat{H}(\psi_{t})/2]^{-1}[1 + i\epsilon\hat{H}(\psi_{t+\Delta t})/2]\right\}^{-1} \\
&\quad = [1 + i\epsilon\hat{H}(\psi_{t+\Delta t})]^{-1}[1 - i\epsilon\hat{H}(\psi_{t})/2] \\
&\quad = \hat{U}_{\mathrm{trap}}(t+\Delta t, t; \psi).
\end{aligned} \tag{B.9}$$

B.2 Exponential convergence of the wavefunction with respect to the grid density

Figures B.1 and B.2 show the convergence of the wavefunction with respect to the grid density at the final times $t_f = 256$ a.u. and $t_f = 2048$ a.u., respectively. For both figures, the goal of the calculation was to increase the population of the excited state in the presence of nonadiabatic couplings and the approximate explicit TVT split-operator algorithm was used with a time step $\Delta t = 2^{-1}$ a.u. The grid convergence was obtained by fixing the number of grid points of one of the two dimensions and repeating the calculation with a varying number of grid points for the other dimension. For each increase in the number of points by a factor of $k \approx \sqrt{2}$ in the varying dimension, the position and momentum ranges as well as densities in that dimension were increased by a factor $\sqrt{k} \approx 2^{1/4}$. Then, the error was measured by the distance $\|\psi_{t_f}(N_1, Y) - \psi_{t_f}(\sqrt{2}N_1, Y)\|$ and $\|\psi_{t_f}(X, N_2) - \psi_{t_f}(X, \sqrt{2}N_2)\|$ for the grid convergence of the first and second dimension, respectively, with $\psi_{t_f}(N_1, N_2)$ denoting the wavefunction at the final time t_f, obtained using grids consisting of N_1 and N_2 points in the first and second dimension, respectively. Note also that X and Y are the fixed numbers of grid points of the first and second dimensions, respectively. The comparison of wavefunctions that are represented on different grids was performed by trigonometric interpolation of the wavefunction

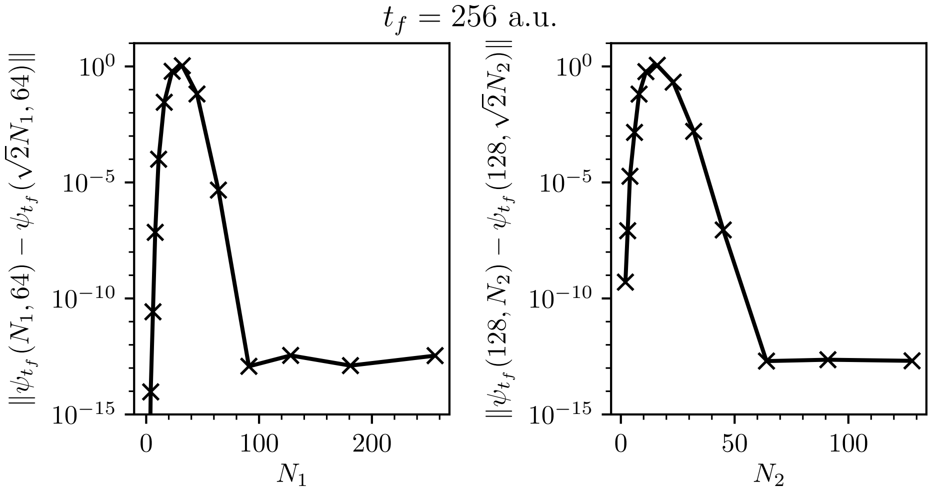

Figure B.1 – Error of the wavefunction at the final time $t_f = 256$ a.u. as a function of the number of grid points. The figure indicates that the numerical grids consisting of $N_1 = 128$ points between $\theta = \pm\pi/2$ a.u. and $N_2 = 64$ points between $q_c = \pm 9.0$ a.u. are converged. All calculations were performed using the approximate explicit TVT split-operator algorithm with time step $\Delta t = 2^{-1}$ a.u.

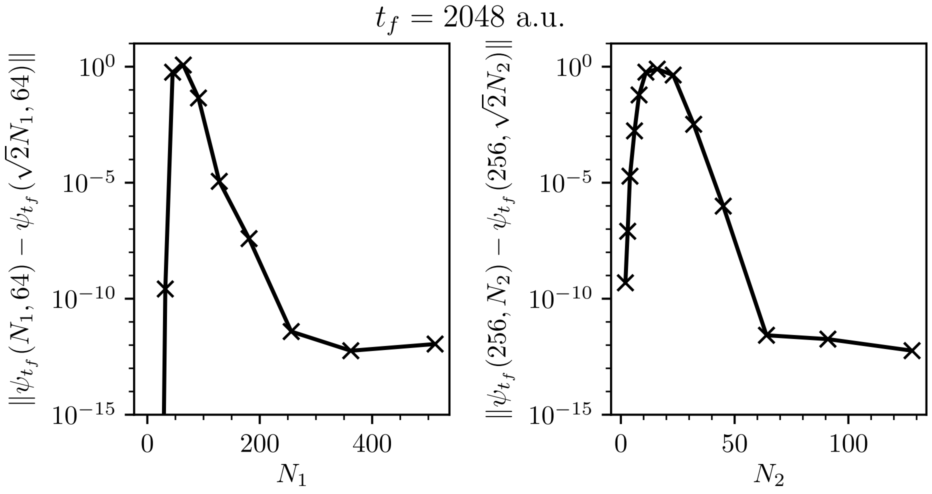

Figure B.2 – Error of the wavefunction at the final time $t_f = 2048$ a.u. as a function of the number of grid points. The figure indicates that the numerical grids consisting of $N_1 = 256$ points between $\theta = \pm 3\pi/2$ a.u. and $N_2 = 64$ points between $q_c = \pm 9.0$ a.u. are converged. All calculations were performed using the approximate explicit TVT split-operator algorithm with time step $\Delta t = 2^{-1}$ a.u.

represented on the sparser grid. In both figures, exponential convergence with respect to the grid density of each dimension is observed.

B.3 Results for the other simulations

We present here the results obtained when controlling the population (in the absence of nonadiabatic couplings) as well as the energy (in the presence and the absence of nonadiabatic couplings). Figures B.3–B.5 show the convergence with respect to the time step Δt of the wavefunction at the final time t_f for the different simulations and Figs. B.6–B.8 show the efficiency of various algorithms. The geometric properties are displayed in Figs. B.9–B.14.

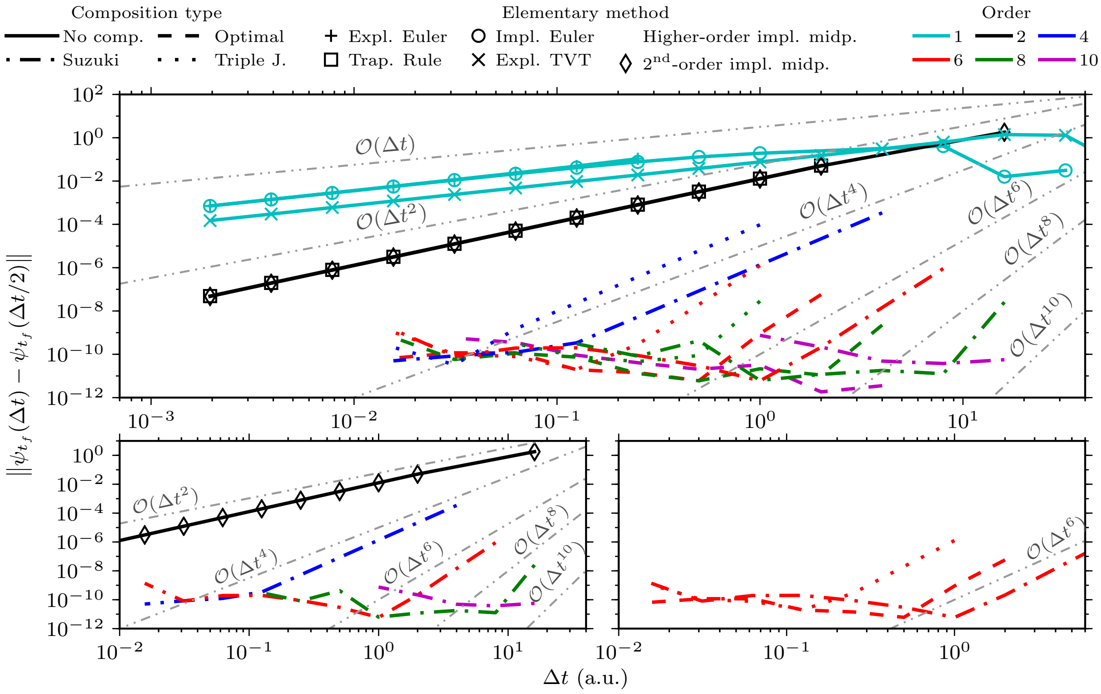

Figure B.3 – Convergence of the molecular wavefunction at the final time t_f achieved by the local population control in the absence of nonadiabatic couplings. Top: All studied methods, i.e., explicit and implicit Euler methods, approximate explicit TVT split-operator algorithm, trapezoidal rule, implicit midpoint method and its symmetric compositions. Bottom-left: Methods obtained with the Suzuki composition. Bottom-right: Sixth-order methods obtained with different composition schemes.

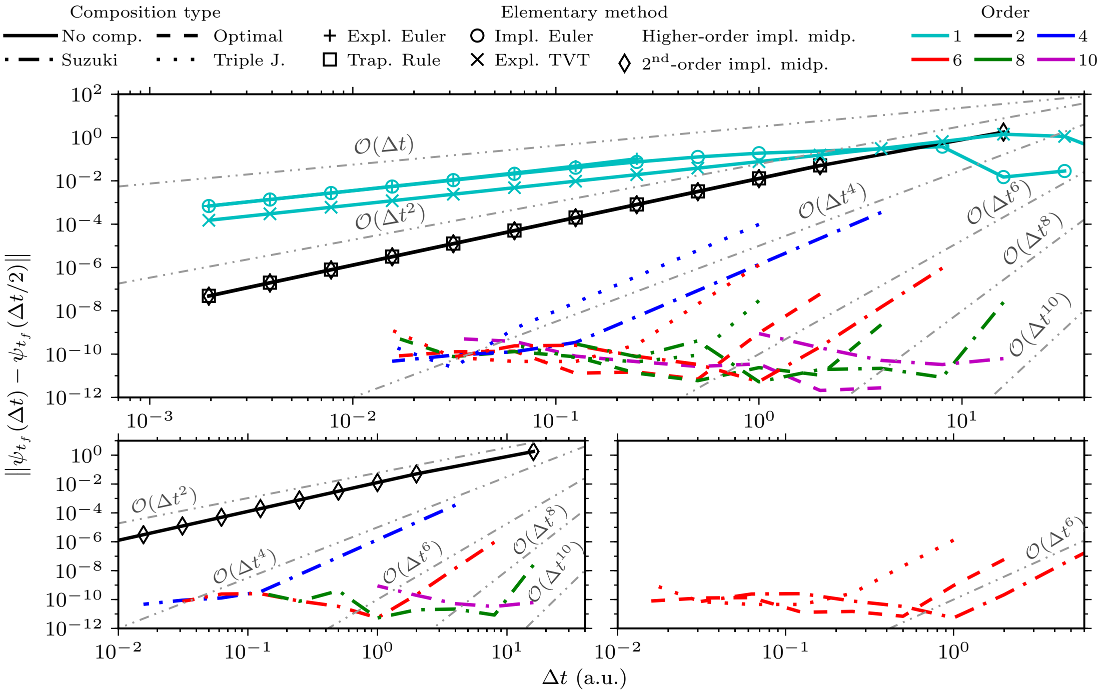

Figure B.4 – Same as Fig. B.3, but for energy control with nonadiabatic couplings.

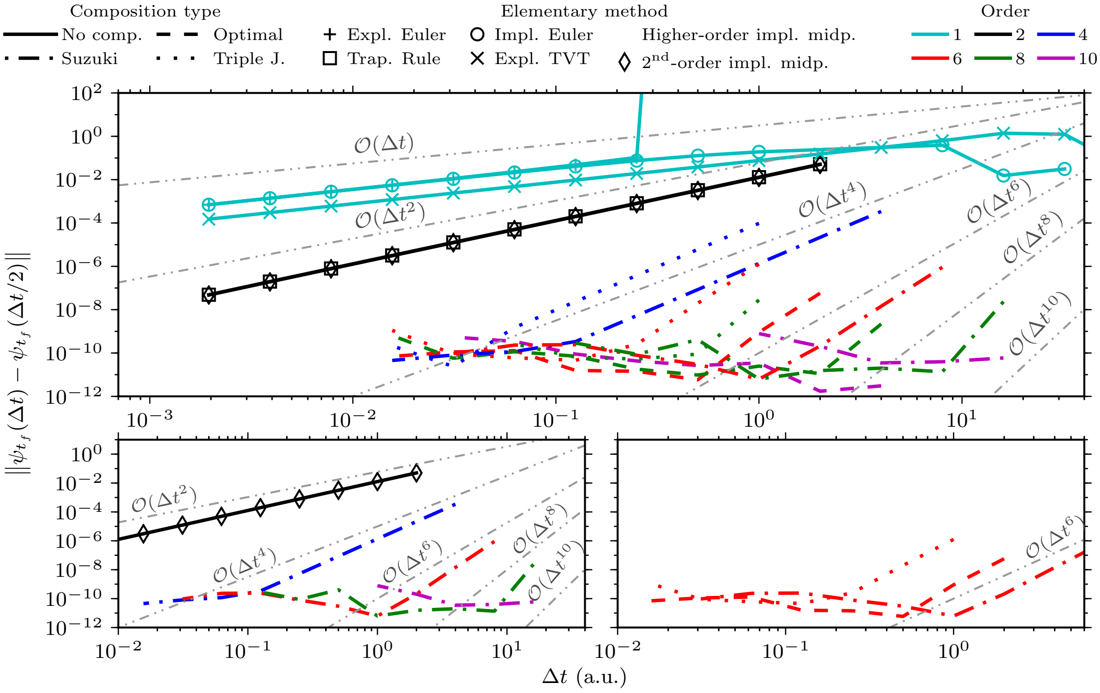

Figure B.5 – Same as Fig. B.3, but for energy control without nonadiabatic couplings.

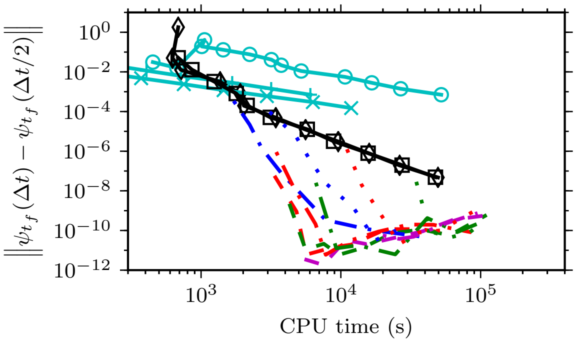

Figure B.6 – Efficiency of the integrators used for the local population control of retinal in the absence of nonadiabatic couplings. Efficiency is measured by plotting the convergence error as a function of the CPU time.

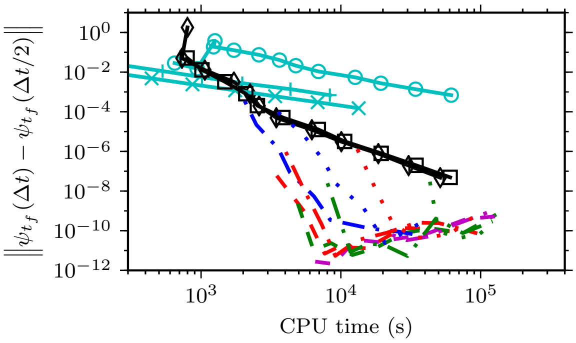

Figure B.7 – Same as Fig. B.6, but for energy control with nonadiabatic couplings.

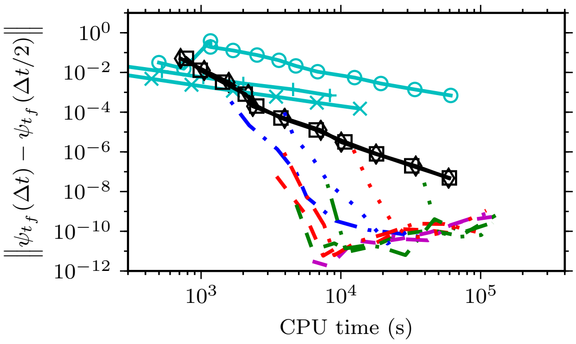

Figure B.8 – Same as Fig. B.6, but for energy control without nonadiabatic couplings.

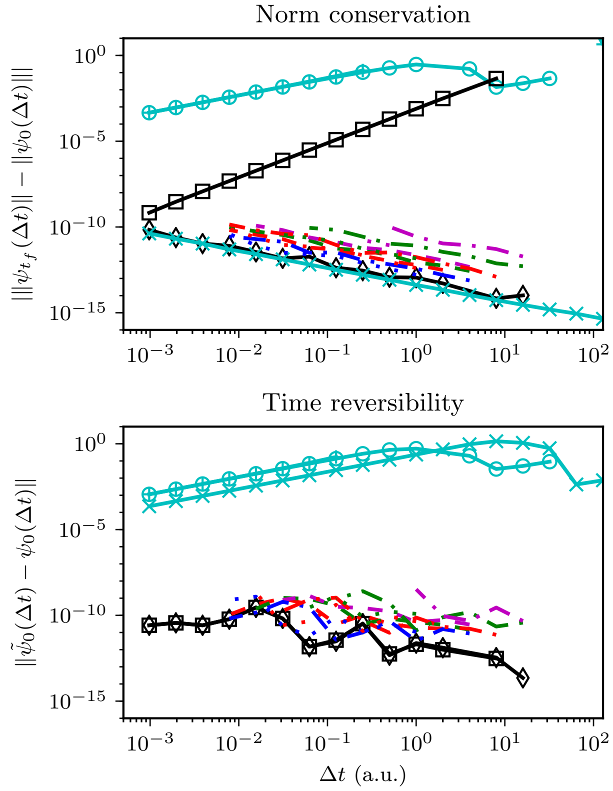

Figure B.9 – Norm conservation (top) and time reversibility (bottom) of various integrators at the final time t_f as a function of the time step Δt used for the local population control in the absence of nonadiabatic couplings. Time reversibility is measured by the distance between the initial state ψ_0 and a "forward-backward" propagated state $\tilde{\psi}_0 := \hat{U}(0, t : \psi)\hat{U}(t, 0; \psi)\psi_0$ [Eq. (3.12)].

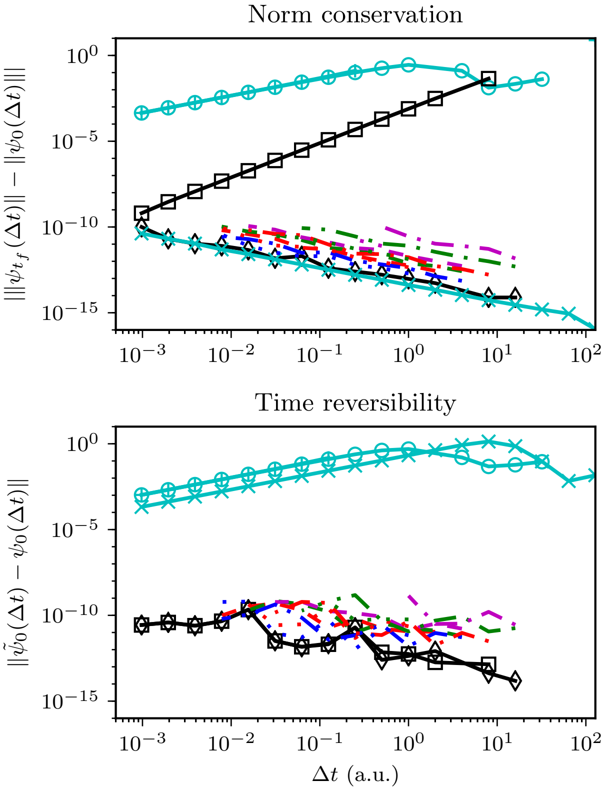

Norm conservation

Time reversibility

Figure B.10 – Same as Fig B.9, but for energy control in the presence of nonadiabatic couplings.

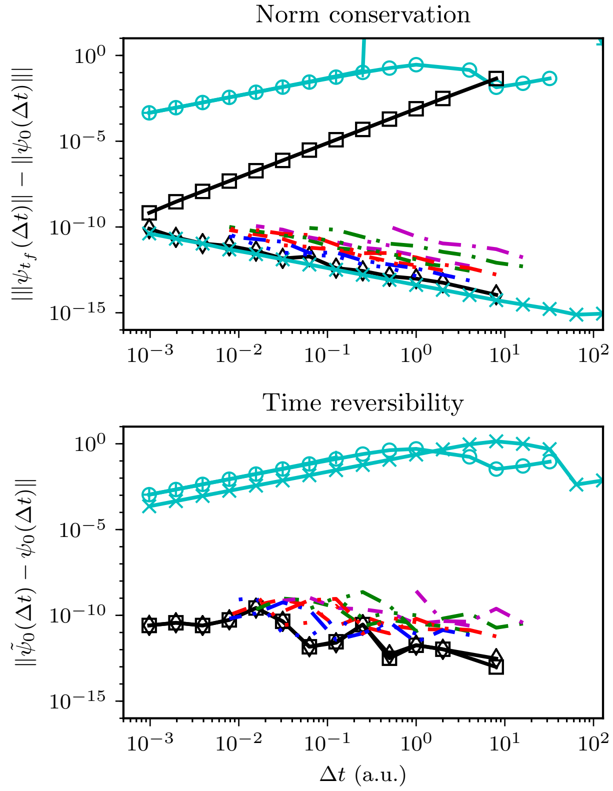

Figure B.11 – Same as Fig B.9, but for energy control in the absence of nonadiabatic couplings.

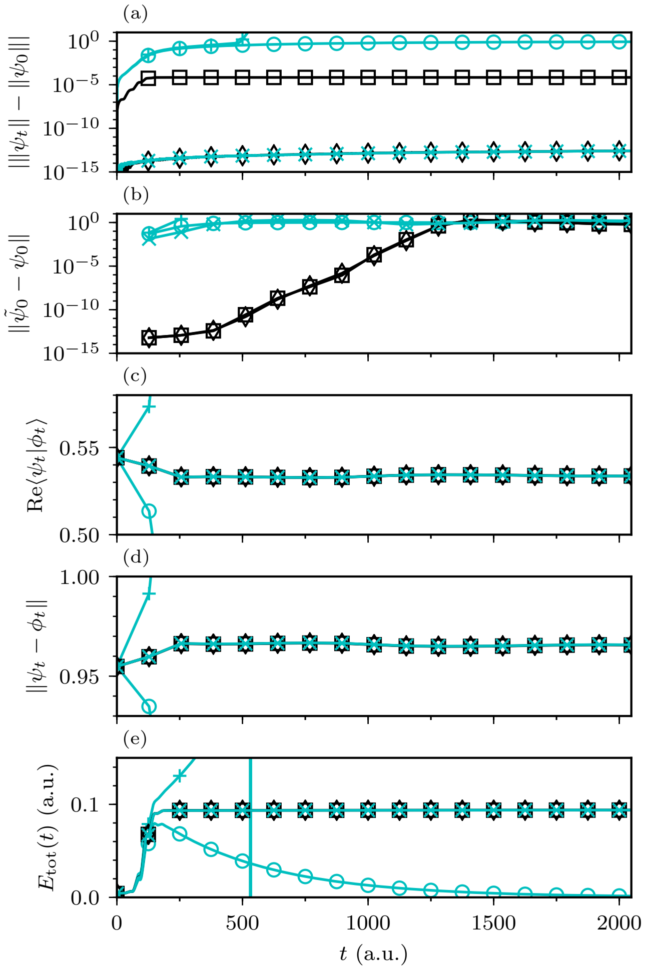

Figure B.12 – Geometric properties of various integrators used for the local population control in the absence of nonadiabatic couplings. Panel (a) shows that only the implicit midpoint and approximate explicit split-operator methods conserve the norm, while panel (b) demonstrates that only the implicit midpoint method and the trapezoidal rule are time-reversible. (Reversibility is measured as in Fig. B.9). Bottom three panels show that no method conserves (c) the inner product, (d) distance between two states (which would imply stability), or (e) total energy $E_{\mathrm{tot}}(t) := E_0(t) + \langle \hat{\mathbf{V}}_{\mathrm{LCT}}(\psi_t)\rangle_{\psi_t}$ because even the exact evolution operator does not preserve these properties. State ϕ_0 is ψ_0 displaced along the reaction coordinate, i.e., a two-dimensional Gaussian wavepacket of the form (2.16), with parameters $q_0 = (0.1, 0)$, $p_0 = (0, 0)$, and $\sigma_0 = (0.128, 0)$ a.u. The time step $\Delta t = 2^{-2}$ a.u. was used for all calculations and line labels are the same as in Fig. B.3. Note that only a few points of the Euler methods are visible in some of the plots because the results of the Euler methods leave the range of these plots very rapidly.

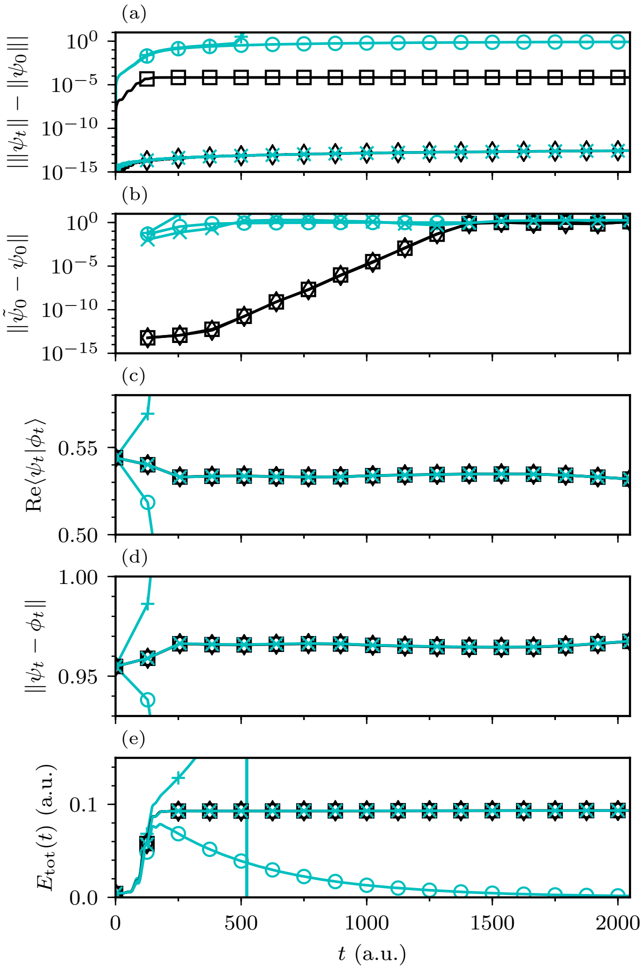

Figure B.13 – Same as Fig. B.12, but for energy control with nonadiabatic couplings.

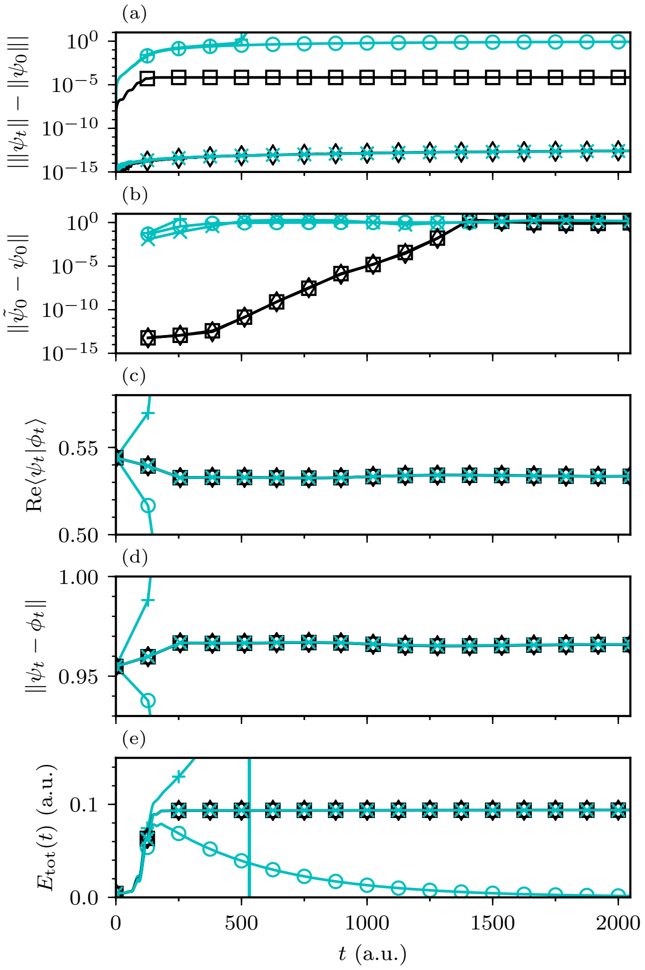

Figure B.14 – Same as Fig. B.12, but for energy control without nonadiabatic couplings.

B.4 Loss of time reversibility due to roundoff errors

Figure B.15 displays, for the population control in the presence of nonadiabatic couplings, the influence of various parameters on the time reversibility of the implicit midpoint method. This figure aims at demonstrating that the loss of time reversibility at longer times is due to the combination of nonlinearity and accumulation of roundoff errors and errors due to the approximate solution of the nonlinear system described by Eq. (3.21) of the main text. Indeed, when using the implicit midpoint method, this nonlinear system is only solved up to a limited accuracy ε (i.e., the nonlinear system is considered solved if $\|f(\psi^{(k+1)})\| \leq \varepsilon$).

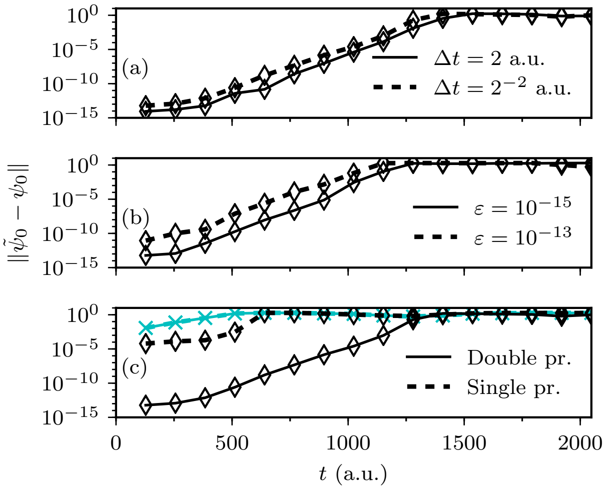

Figure B.15 – Influence of various parameters on the time reversibility of the implicit midpoint method. The three panels show that the time reversibility of the implicit midpoint method deteriorates (a) if the time step Δt is decreased, leading to a faster accumulation of roundoff errors, (b) if the error ε threshold of the nonlinear solver is increased, and (c) if the precision of the floating-point arithmetic is decreased. Note that decreasing the floating-point precision does not have a visible influence on the approximate explicit split-operator algorithm, which is irreversible by construction. Time reversibility is measured as in Fig. B.9.

Panel (a) shows the influence of the time step on the time reversibility of the implicit midpoint method. For this, we propagated the wavefunction to the final time $t_f = 2048$ a.u. with different time steps and kept the same error threshold ε for solving the nonlinear system. We observe that decreasing the time step decreases the time reversibility of the implicit midpoint method. This is due to a faster accumulation of roundoff errors caused by the greater number of steps performed when using a smaller time step.

Panel (b) depicts the influence of the error threshold ε on the time reversibility. Here, we propagated the wavefunction using the implicit midpoint method using the same parameters but only changed the error threshold ε. As expected, a larger error threshold results in a faster loss of time reversibility as the time increases.

Finally, panel (c) shows the influence of the floating-point format precision. We compare the single and double precision floating-point formats for the implicit midpoint method and the approximate explicit TVT split-operator algorithm. The results indicate that decreasing the floating-point format from double to single precision, while keeping other parameters fixed, decreases the time reversibility of the implicit midpoint method while it does not affect the approximate explicit TVT split-operator algorithm. Because the implicit midpoint method is by construction time-reversible, decreasing the floating-point format has the same effect as increasing the threshold ε, namely increasing the roundoff error when solving the nonlinear system, hence decreasing its time reversibility. In contrast, the approximate explicit TVT split-operator algorithm is not affected by the change of precision because it is, by construction, time-irreversible and would remain irreversible even if infinite precision were available.

C The generalized minimal residual method

The generalized minimal residual method is an iterative method for solving linear systems

$$Ax = b, \tag{C.1}$$

such as the one encountered in Eq. (3.25), with $A \equiv J(\psi^{(k)})$, $x \equiv \delta\psi^{(k)}$, and $b \equiv -f(\psi^{(k)})$. Here, we used the restart version of the algorithm. Following Refs. [110] and [109], the algorithm can be summarized in four steps:

1. Initialization
2. Arnoldi's method for constructing an orthonormal basis of the Krylov subspace
3. Forming the solution
4. Restart

Each step is described in more detail below.

C.1 Initialization

The initialization is performed as follows: Choose an initial guess x_0, an error threshold ϵ, a maximal number of iterations m, and compute the initial residue $r_0 = b - Ax_0$, $\beta := \|r_0\|$, and $v_1 := r_0/\beta$.

C.2 Arnoldi's method

Arnoldi's method obtains an orthonormal basis of the Krylov subspace [164, 165]

$$\mathcal{K}_m := \mathrm{span}\{v_1, Av_1, \ldots, A^{m-1}v_1\}.$$

The orthonormal vectors, which span the Krylov subspace, are obtained using the modified Gram-Schmidt process. The algorithm is:

```
1. For $j = 1, 2, \ldots, m$ Do:
2. Compute $w_j := Av_j$
3. For $i = 1, \ldots j$ Do:
4. $h_{ij} := \langle v_i | w_j \rangle$
5. $w_j := w_j - h_{ij} v_i$
6. End Do
7. $h_{j+1,j} = \|w_j\|$. If $h_{j+1,j} = 0$, set $m = j$ and stop
8. $v_{j+1} = w_j / h_{j+1,j}$
9. End Do
```

C.3 Forming the solution

Here, the goal is to find the solution which minimizes the norm of the residue after m iterations of Arnoldi's method. Now that the orthogonal basis is constructed, we know that the solution lies in the affine subspace $x_0 + \mathcal{K}_m$. Thus, any vector x in that space can be written as

$$x = x_0 + V_m y, \tag{C.2}$$

where $V_m := \{v_1, \ldots, v_m\}$ is the matrix constructed from the orthonormal vectors v_j and y is an arbitrary vector of size m. The problem translates to the minimization of the function

$$\begin{aligned}
M(y) &= \|b - A(x_0 + V_m y)\| \\
&= \|r_0 - AV_m y\| \\
&= \|\beta v_1 - V_{m+1}\bar{H}_m y\| \\
&= \|V_{m+1}(\beta e_1 - \bar{H}_m y)\| \\
&= \|(\beta e_1 - \bar{H}_m y)\|,
\end{aligned} \tag{C.3}$$

where $\bar{H}_m = \{h_{ij}\}_{1\leq i\leq m+1, 1\leq j\leq m}$ is the the $(m+1)\times m$ Hessenberg matrix constructed from the elements h_{ij} obtained in Arnoldi's method and where $e_1 = (1, 0, \ldots, 0)^T$ is the first vector in the standard basis of $\mathbb{R}^{m+1}$. The third line of Eq. (C.3) was obtained using $AV_m = V_{m+1}\bar{H}_m$, while the last line follows because the columns of V_{m+1} are orthonormal. This step of the generalized minimal residual algorithm can be summarized as:

1. Construct the Hessenberg matrix $\bar{H}_m$
2. Compute y_m, the vector of dimension m minimizing $M(y)$
3. Compute the solution $x_m = x_0 + V_m y_m$

C.4 Restart

This last step of the generalized minimal residual algorithm determines whether the solution x_m, obtained at the previous step, is sufficiently accurate. If the condition $\|r_m\| := \|b - Ax_m\| \leq \epsilon$ holds, x_m is taken as the solution. If $\|r_m\| > \epsilon$, we set $x_0 = x_m$ and restart the algorithm.

C.5 Practical implementation

In practice, it is difficult to compute the vector y_m minimizing $M(y)$. For this, it is preferable to use the decomposition

$$\bar{R}_m = Q_m \bar{H}_m, \tag{C.4}$$

where Q_m is an $(m+1) \times (m+1)$ orthogonal matrix and $\bar{R}_m$ is an upper triangular matrix of dimension $(m+1) \times m$ with a bottom row consisting only of zeroes, i.e., it can be decomposed as

$$\bar{R}_m = \begin{pmatrix} R_m \\ 0 \end{pmatrix}, \tag{C.5}$$

where R_m is an $m \times m$ upper triangular matrix. Once this factorization is performed, the minimization problem simplifies to

$$y_m = \operatorname{argmin}_y \|\beta e_1 - \bar{H}_m y\| = \operatorname{argmin}_y \|\bar{g}_m - \bar{R}_m y\|, \tag{C.6}$$

where $\bar{g}_m := Q_m \beta \epsilon_1 = (\gamma_1, \ldots, \gamma_{m+1})^T$ and can be decomposed as $\bar{g}_m = (g_m, \gamma_{m+1})^T$. The solution of the minimization problem is now trivially obtained by solving the linear triangular system $R_m y_m = g_m$, which yields

$$y_m = R_m^{-1} g_m. \tag{C.7}$$

Note that it can be proven that the residue after m iterations of the algorithm is given by the last element of $\bar{g}_m$, i.e., $r_m = |\gamma_{m+1}|$ [110].

Instead of constructing $\bar{H}_m$ and computing its decomposition (C.4) after m iterations of Arnoldi's method, both can be performed in an iterative manner, at each iteration j of Arnoldi's method. This makes it possible to obtain $\bar{g}_j$ and therefore to check if $r_j \leq \epsilon$ at each iteration step j, without even solving the minimization problem.

To do so, $\bar{H}_{j+1}$ is obtained by concatenation of $\bar{H}_j$ and the elements obtained in steps 4 and 7 of Arnoldi's method, i.e.,

$$\bar{H}_{j+1} = \begin{pmatrix} & h_{1,j+1} \\ \bar{H}_j & \vdots \\ & h_{j+1,j+1} \\ 0 & h_{j+2,j+1} \end{pmatrix}. \tag{C.8}$$

Then, multiplying $\bar{H}_{j+1}$ on the left by the orthogonal matrix obtained at the previous iteration yields an almost upper triangular matrix

$$\tilde{R}_{j+1} = \begin{pmatrix} Q_j & 0 \\ 0 & 1 \end{pmatrix} \bar{H}_{j+1} = \begin{pmatrix} & r_{1,j+1} \\ R_j & \vdots \\ & r_{j,j+1} \\ 0 & \eta \\ 0 & \nu \end{pmatrix} \tag{C.9}$$

of dimension $(j+2) \times (j+1)$. Note that η and ν denote the arbitrary elements $j+1, j+1$ and $j+2, j+1$ of the matrix $\tilde{R}_{j+1}$. From there, $\bar{R}_{j+1}$, which is upper triangular, is obtained by rotating $\tilde{R}_{j+1}$:

$$\bar{R}_{j+1} = Q_{j+1}\bar{H}_{j+1} = \Omega_j \tilde{R}_{j+1} = \begin{pmatrix} & r_{1,j+1} \\ R_j & \vdots \\ 0 & r_{j+1,j+1} \\ 0 & 0 \end{pmatrix}, \tag{C.10}$$

where

$$\Omega_j = \begin{pmatrix} 1 & & & & \\ & \ddots & & & \\ & & 1 & & \\ & & & c_j^* & s_j^* \\ & & & -s_j & c_j \end{pmatrix} \tag{C.11}$$

is a rotation matrix of dimension $(j+2) \times (j+2)$. The complex coefficients

$$c_j := \frac{\eta}{\sqrt{|\eta|^2 + |\nu|^2}} \quad \text{and} \quad s_j := \frac{\nu}{\sqrt{|\eta|^2 + |\nu|^2}} \tag{C.12}$$

of Ω_j are selected so that multiplying Ω_j with $\tilde{R}_{j+1}$ yields the upper triangular matrix $\bar{R}_{j+1}$. From Eq. (C.10), Q_{j+1} is obtained by applying the rotation matrix Ω_j to Q_j as

$$Q_{j+1} = \Omega_j \begin{pmatrix} Q_j & 0 \\ 0 & 1 \end{pmatrix}. \tag{C.13}$$

D Supporting information for Chapter 4

D.1 Geometric properties of various integrators

Here we demonstrate the geometric properties of the explicit TV and implicit VT, TVT, and VTV algorithms.

D.1.1 Norm conservation

The evolution operator $\hat{U}_{\hat{T}}(\Delta t)$ of the Hermitian kinetic energy operator $\hat{T}$ conserves the norm $\|\psi_t\|$ of the state ψ_t because

$$\begin{aligned}\|\hat{U}_{\hat{T}}(\Delta t)\psi_t\|^2 &= \langle\psi_t|\hat{U}_{\hat{T}}(\Delta t)^\dagger\hat{U}_{\hat{T}}(\Delta t)\psi_t\rangle = \langle\psi_t|\psi_t\rangle \\ &= \|\psi_t\|^2, \end{aligned} \tag{D.1}$$

where we used the relation

$$\hat{U}_{\hat{A}}(\Delta t)^\dagger = (e^{-i\hat{A}\Delta t/\hbar})^\dagger = \hat{U}_{\hat{A}}(\Delta t)^{-1}, \tag{D.2}$$

which holds for any Hermitian operator $\hat{A}$, to obtain the second equality.

For the potential evolution operator, we first assume that while the operator $\hat{V}_{\text{tot}} : \psi \mapsto \hat{V}_{\text{tot}}(\psi)\psi$ is nonlinear, for each ϕ the operator $\hat{V}_{\text{tot}}(\phi) : \psi \mapsto \hat{V}_{\text{tot}}(\phi)\psi$ is linear. Moreover, we assume that $\hat{V}_{\text{tot}}(\phi)$ has real expectation values $\langle\hat{V}_{\text{tot}}(\phi)\rangle_\psi$ in any state ψ, which for a linear operator implies that it is Hermitian. Therefore, the evolution operator $\hat{U}_{\hat{V}_{\text{tot}(\phi)}}(\Delta t)$ conserves, for any ϕ, the norm of the state ψ_t

because

$$\begin{aligned}\|\hat{U}_{\hat{V}_{\mathrm{tot}(\phi)}}(\Delta t)\psi_t\|^2 &= \langle\psi_t|\hat{U}_{\hat{V}_{\mathrm{tot}(\phi)}}(\Delta t)^\dagger\hat{U}_{\hat{V}_{\mathrm{tot}(\phi)}}(\Delta t)\psi_t\rangle \\ &= \langle\psi_t|\psi_t\rangle = \|\psi_t\|^2,\end{aligned} \tag{D.3}$$

where we used Eq. (D.2) to obtain the second equality.

Composing two norm-conserving evolution operators $\hat{U}_{\hat{A}}$ and $\hat{U}_{\hat{B}}$ of Hermitian operators $\hat{A}$ and $\hat{B}$, respectively, yields a norm-conserving integrator $\hat{U}_{\hat{A}\hat{B}}(\Delta t) := \hat{U}_{\hat{A}}(\Delta t)\hat{U}_{\hat{B}}(\Delta t)$. Indeed, we have

$$\begin{aligned}\|\hat{U}_{\hat{A}\hat{B}}(\Delta t)\psi_t\|^2 &= \|\hat{U}_{\hat{A}}(\Delta t)\psi_t'\|^2 = \|\psi_t'\|^2 \\ &= \|\hat{U}_{\hat{B}}(\Delta t)\psi_t\|^2 = \|\psi_t\|^2,\end{aligned} \tag{D.4}$$

where $\psi_t' := \hat{U}_{\hat{B}}(\Delta t)\psi_t$. Therefore, all proposed integrators (including the integrators obtained by symmetric composition of TVT or VTV algorithms) conserve the norm because they are all compositions of the norm-conserving integrators $\hat{U}_{\hat{T}}(\Delta t)$ and $\hat{U}_{\hat{V}_{\mathrm{tot}(\phi)}}(\Delta t)$.

D.1.2 Symmetry and time-reversibility

Neither the explicit TV nor implicit VT method is symmetric because

$$\begin{aligned}\hat{U}_{TV}(t+\Delta t, t; \psi_t)^* &= \hat{U}_{TV}(t, t+\Delta t; \psi_{t+\Delta t})^{-1} \\ &= [\hat{U}_{\hat{T}}(-\Delta t)\hat{U}_{\hat{V}_{\mathrm{tot}(\psi_{t+\Delta t})}}(-\Delta t)]^{-1} \\ &= \hat{U}_{\hat{V}_{\mathrm{tot}(\psi_{t+\Delta t})}}(\Delta t)\hat{U}_{\hat{T}}(\Delta t) \\ &= \hat{U}_{VT}(t+\Delta t, t; \psi_{t+\Delta t}) \\ &\neq \hat{U}_{TV}(t+\Delta t, t; \psi_t)\end{aligned} \tag{D.5}$$

and

$$\begin{aligned}\hat{U}_{VT}(t+\Delta t, t; \psi_{t+\Delta t})^* &= \hat{U}_{VT}(t, t+\Delta t; \psi_t)^{-1}\\ &= [\hat{U}_{\hat{V}_{\mathrm{tot}}(\psi_t)}(-\Delta t)\hat{U}_{\hat{T}}(-\Delta t)]^{-1}\\ &= \hat{U}_{\hat{T}}(\Delta t)\hat{U}_{\hat{V}_{\mathrm{tot}}(\psi_t)}(\Delta t)\\ &= \hat{U}_{TV}(t+\Delta t, t; \psi_t)\\ &\neq \hat{U}_{VT}(t+\Delta t, t; \psi_{t+\Delta t}).\end{aligned} \tag{D.6}$$

As a result, neither the TV nor VT method is time-reversible.

From Eqs. (D.5) and (D.6), we notice that the explicit TV and VT methods are, in fact, adjoints of each other, i.e., $\hat{U}_{TV}^* = \hat{U}_{VT}$ and $\hat{U}_{VT}^* = \hat{U}_{TV}$. In general, the composition of adjoint methods $\hat{U}$ and $\hat{U}^*$, each with a time step $\Delta t/2$, yields symmetric methods $\hat{U}\hat{U}^*$ and $\hat{U}^*\hat{U}$ [88]. Because the implicit TVT and VTV methods are such compositions of adjoint TV and VT methods, both TVT and VTV integrators are symmetric. Applying symmetric composition schemes to these symmetric methods will always yield a symmetric method [88]. Therefore, the proposed high-order integrators are also symmetric and time-reversible.

D.2 Results for all the studied methods

To avoid clutter in the figures of the main text, we showed there only the results of some studied methods. Here, we show the results displayed in Sec.4.3 for all the studied methods. Note that the results of some high-order methods could not be obtained because they did not converge at large time steps (the difference between the initial guess and the implicit solution was too large for the Newton–Raphson method to converge) and became computationally unaffordable at smaller time steps, when the Newton–Raphson method was converging.

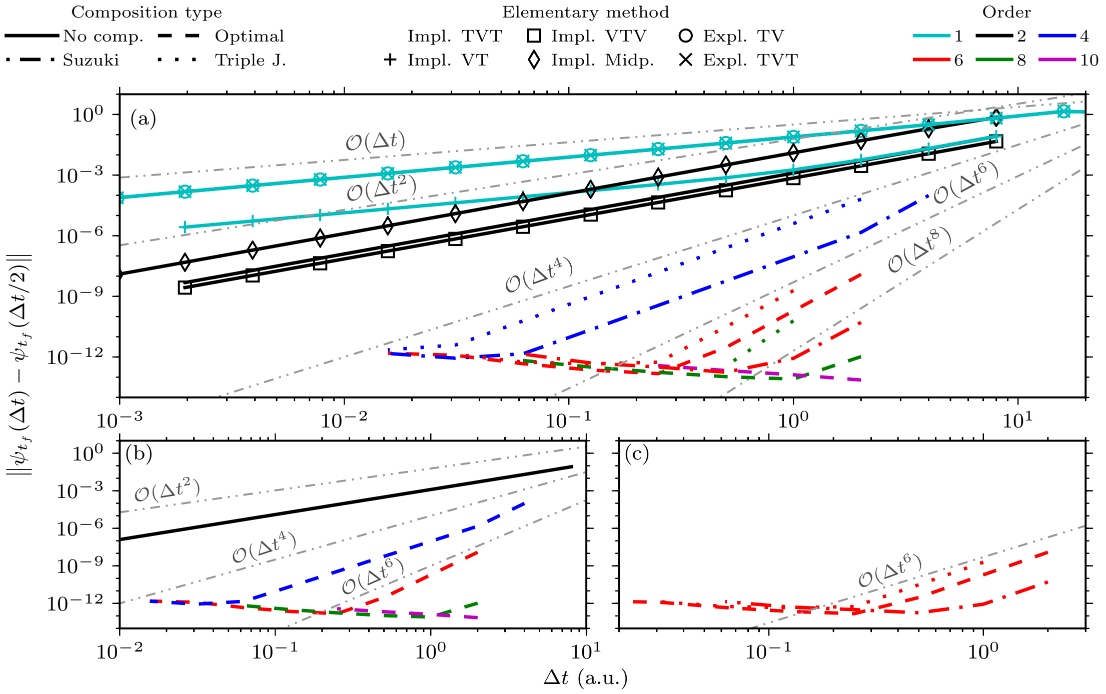

Figure D.1 – Convergence of the molecular wavefunction at the final time $t_f = 256$ a.u. achieved by the local energy control. (a) All studied methods, including symmetric compositions of the TVT split-operator algorithm. (b) Methods obtained with the optimal composition (Suzuki's fractal is the optimal fourth-order composition scheme. (c) Sixth-order methods obtained with different composition schemes.

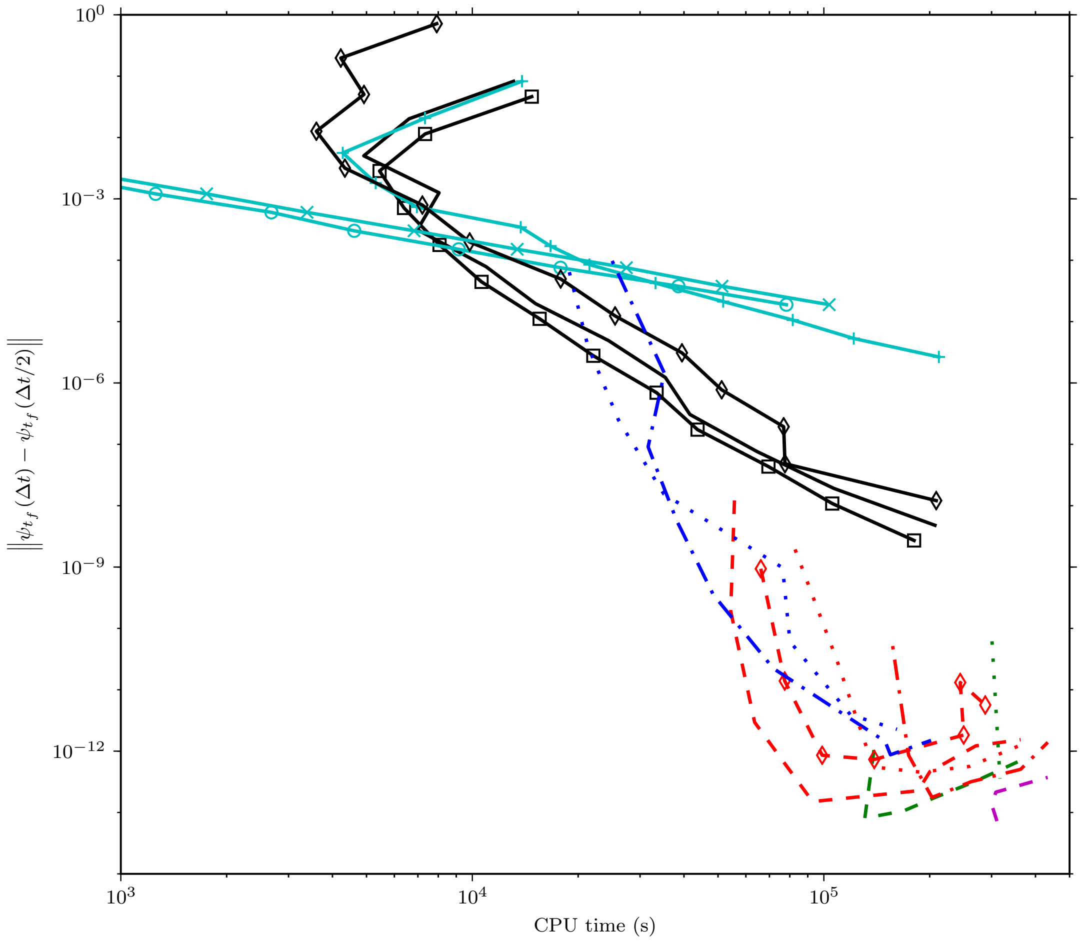

Figure D.2 – Efficiency of various integrators used for simulating the local energy control of retinal up to the final time $t_f = 256$ a.u. Line labels are the same as in Fig. 4.2.

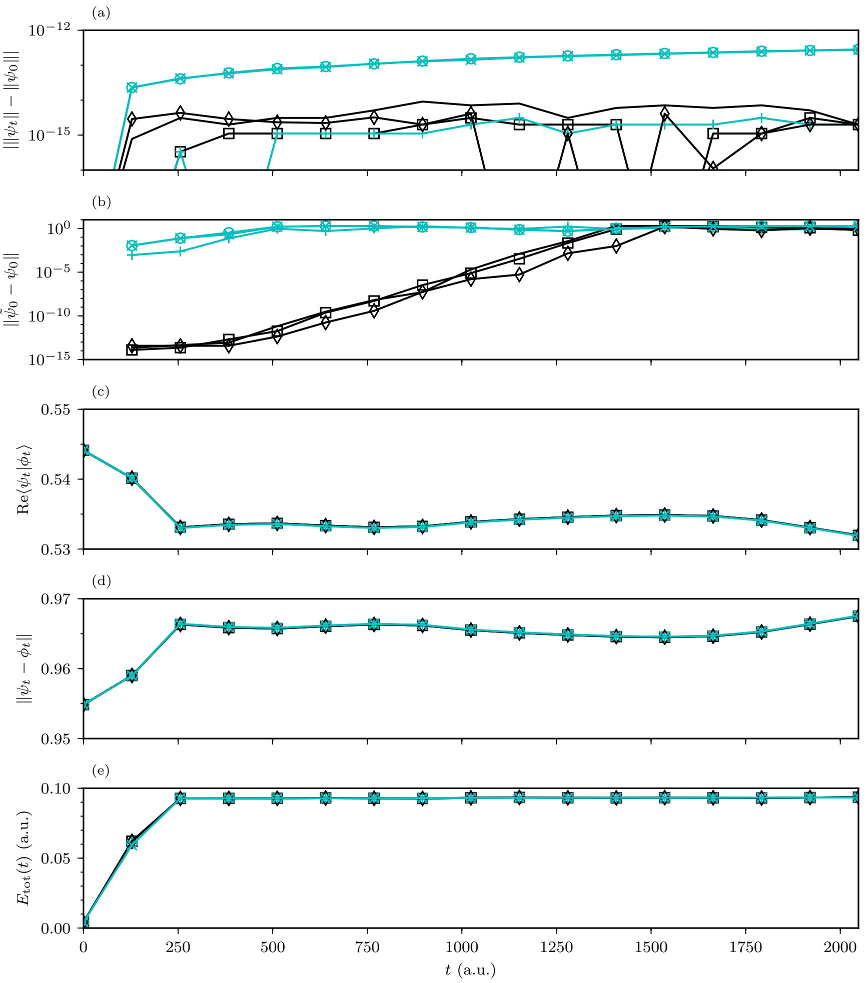

Figure D.3 – Time dependence of the geometric properties of the elementary integrators used for simulating the local energy control up to the final time $t_f = 2048$ a.u. (a) Norm of the wavefunction. (b) Time reversibility. (c) Inner product. (d) Distance between two states (which would imply stability). (e) Total energy. Time reversibility is measured by the distance between the initial state ψ_0 and a “forward-backward” propagated state $\tilde{\psi}_0$ [see Fig. 3.5 and Eq. (3.12)]. The state ϕ_0 is the same as the one used in Fig. 3.5 and line labels are the same as in Fig. 4.2.

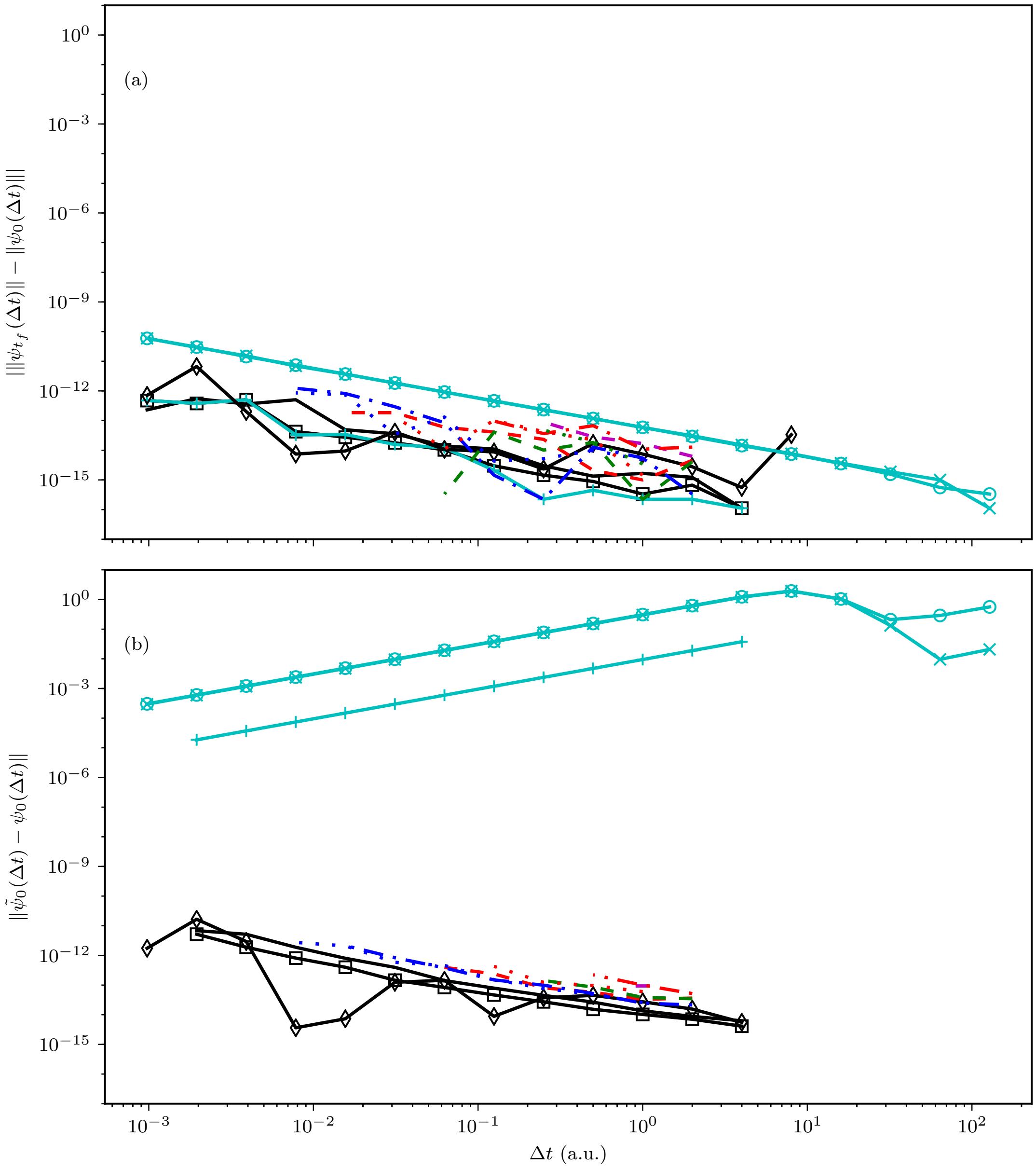

Figure D.4 – Norm conservation (a) and time reversibility (b) of various integrators at the final time $t_f = 256$ a.u. as a function of the time step Δt used for the local energy control of retinal. Reversibility is measured as in Fig. D.3 and line labels are the same as in Fig. 4.2.

Bibliography

[1] M. Born and R. Oppenheimer, Ann. d. Phys. **389**, 457 (1927).

[2] E. J. Heller, *The semiclassical way to dynamics and spectroscopy* (Princeton University Press, Princeton, NJ, 2018).

[3] A. Mokhtari, P. Cong, J. L. Herek, and A. H. Zewail, Nature **348**, 225 (1990).

[4] M. Baer, *Beyond Born-Oppenheimer: Electronic Nonadiabatic Coupling Terms and Conical Intersections*, 1st ed. (Wiley, 2006).

[5] H. Nakamura, *Nonadiabatic Transition: Concepts, Basic Theories and Applications*, 2nd ed. (World Scientific Publishing Company, 2012).

[6] K. Takatsuka, T. Yonehara, K. Hanasaki, and Y. Arasaki, *Chemical Theory Beyond the Born-Oppenheimer Paradigm: Nonadiabatic Electronic and Nuclear Dynamics in Chemical Reactions* (World Scientific, Singapore, 2015).

[7] M. P. Bircher, E. Liberatore, N. J. Browning, S. Brickel, C. Hofmann, A. Patoz, O. T. Unke, T. Zimmermann, M. Chergui, P. Hamm, U. Keller, M. Meuwly, H. J. Woerner, J. Vaníček, and U. Rothlisberger, Struct. Dyn. **4**, 061510 (2017).

[8] V. Engel, H. Metiu, R. Almeida, R. Marcus, and A. H. Zewail, Chem. Phys. Lett. **152**, 1 (1988).

[9] L. R. Khundkar and A. H. Zewail, Annu. Rev. Phys. Chem. **41**, 15 (1990).

[10] H. L. Fragnito, J. Y. Bigot, P. C. Becker, and C. V. Shank, Chem. Phys. Lett. **160**, 101 (1989).

[11] D. Polli, L. Lüer, and G. Cerullo, Rev. Sci. Instr. **78** (2007).

[12] R. M. van der Veen, A. Cannizzo, F. van Mourik, A. Vlček, and M. Chergui, J. Am. Chem. Soc. **133**, 305 (2011).

[13] F. Spzno, M. Haner, and W. Warren, Chem. Phys. Lett. **135**, 97 (1987).

[14] M. M. Wefers and K. A. Nelson, J. Opt. Soc. Am. B **12**, 1343 (1995).

[15] A. Weiner, Prog. Quantum Electron. **19**, 161 (1995).

[16] A. M. Weiner, Rev. Sci. Instr. **71**, 1929 (2000).

[17] T. Brixner and G. Gerber, Opt. Lett. **26**, 557 (2001).

[18] T. Brixner and G. Gerber, ChemPhysChem **4**, 418 (2003).

[19] R. J. Gordon and S. A. Rice, Annu. Rev. Phys. Chem. **48**, 601 (1997), pMID: 15012451.

[20] H. Rabitz, R. de Vivie-Riedle, M. Motzkus, and K. Kompa, Science **288**, 824 (2000).

[21] P. Nuernberger, G. Vogt, T. Brixner, and G. Gerber, Phys. Chem. Chem. Phys. **9**, 2470 (2007).

[22] D. J. Tannor and S. A. Rice, J. Chem. Phys. **83**, 5013 (1985).

[23] D. J. Tannor, R. Kosloff, and S. A. Rice, J. Chem. Phys. **85**, 5805 (1986).

[24] A. P. Peirce, M. A. Dahleh, and H. Rabitz, Phys. Rev. A **37**, 4950 (1988).

[25] R. Kosloff, S. A. Rice, P. Gaspard, S. Tersigni, and D. J. Tannor, Chem. Phys. **139**, 201 (1989).

[26] P. Brumer and M. Shapiro, Annu. Rev. Phys. Chem. **43**, 257 (1992).

[27] R. Kosloff, A. D. Hammerich, and D. Tannor, Phys. Rev. Lett. **69**, 2172 (1992).

[28] D. J. Tannor, *Introduction to Quantum Mechanics: A Time-Dependent Perspective* (University Science Books, Sausalito, 2007).

[29] E. J. Heller, J. Chem. Phys. **62**, 1544 (1975).

[30] M. Wehrle, M. Šulc, and J. Vaníček, J. Chem. Phys. **140**, 244114 (2014).

[31] M. Wehrle, S. Oberli, and J. Vaníček, J. Phys. Chem. A **119**, 5685 (2015).

[32] T. Begušić, A. Patoz, M. Šulc, and J. Vaníček, Chem. Phys. **515**, 152 (2018).

[33] R. D. Coalson and M. Karplus, J. Chem. Phys. **93**, 3919 (1990).

[34] C. Lasser and C. Lubich, Acta Numerica **29**, 229 (2020).

[35] M. Ben-Nun and T. J. Martínez, J. Phys. Chem. A **103**, 10517 (1999).

[36] M. Ben-Nun, J. Quenneville, and T. J. Martínez, J. Phys. Chem. A **104**, 5161 (2000).

[37] M. Ben-Nun and T. J. Martínez, Adv. Chem. Phys. **121**, 439 (2002).

[38] B. F. E. Curchod and T. J. Martínez, Chem. Rev. **118**, 3305 (2018).

[39] D. V. Makhov, C. Symonds, S. Fernandez-Alberti, and D. V. Shalashilin, Chem. Phys. **493**, 200 (2017).

[40] D. V. Shalashilin, J. Chem. Phys. **130**, 244101 (2009).

[41] D. V. Shalashilin, J. Chem. Phys. **132**, 244111 (2010).

[42] G. A. Worth, M. A. Robb, and I. Burghardt, Faraday Discuss. **127**, 307 (2004).

[43] G. W. Richings, I. Polyak, K. E. Spinlove, G. A. Worth, I. Burghardt, and B. Lasorne, Int. Rev. Phys. Chem. **34**, 269 (2015).

[44] G. W. Richings and G. A. Worth, J. Phys. Chem. A **119**, 12457 (2015).

[45] M. F. Herman and E. Kluk, Chem. Phys. **91**, 27 (1984).

[46] W. H. Miller, J. Phys. Chem. A **105**, 2942 (2001).

[47] B. G. Levine and T. J. Martínez, J. Phys. Chem. A **113**, 12815 (2009).

[48] W. J. Glover, T. Mori, M. S. Schuurman, A. E. Boguslavskiy, O. Schalk, A. Stolow, and T. J. Martínez, J. Chem. Phys. **148**, 164303 (2018).

[49] P. Eisenbrandt, M. Ruckenbauer, and I. Burghardt, J. Chem. Phys. **149**, 174102 (2018).

[50] A. Patoz, T. Begušić, and J. Vaníček, J. Phys. Chem. Lett. **9**, 2367 (2018).

[51] I. Burghardt, K. Giri, and G. A. Worth, J. Chem. Phys. **129**, 174104 (2008).

[52] D. O. Harris, G. G. Engerholm, and W. D. Gwinn, J. Chem. Phys. **43**, 1515 (1965).

[53] J. C. Light, I. P. Hamilton, and J. V. Lill, J. Chem. Phys. **82**, 1400 (1985).

[54] R. G. Littlejohn, M. Cargo, T. Carrington, K. A. Mitchell, and B. Poirier, J. Chem. Phys. **116**, 8691 (2002).

[55] H.-D. Meyer, U. Manthe, and L. S. Cederbaum, Chem. Phys. Lett. **165**, 73 (1990).

[56] G. A. Worth, H.-D. Meyer, H. Köppel, L. S. Cederbaum, and I. Burghardt, Int. Rev. Phys. Chem. **27**, 569 (2008).

[57] H. Wang and M. Thoss, J. Chem. Phys. **119**, 1289 (2003).

[58] U. Manthe, H.-D. Meyer, and L. S. Cederbaum, J. Chem. Phys. **97**, 3199 (1992).

[59] U. Manthe and A. D. Hammerich, Chem. Phys. Lett. **211**, 7 (1993).

[60] K. Giri, E. Chapman, C. S. Sanz, and G. Worth, J. Chem. Phys. **135**, 044311 (2011).

[61] G. Worth, H.-D. Meyer, and L. Cederbaum, Chem. Phys. Lett. **299**, 451 (1999).

[62] A. Raab, G. A. Worth, H.-D. Meyer, and L. S. Cederbaum, J. Chem. Phys. **110**, 936 (1999).

[63] B. Brüggemann, P. Persson, H.-D. Meyer, and V. May, Chem. Phys. **347**, 152 (2008).

[64] H. Tamura, I. Burghardt, and M. Tsukada, J. Phys. Chem. C **115**, 10205 (2011).

[65] H. Tamura and I. Burghardt, J. Am. Chem. Soc. **135**, 16364 (2013).

[66] M. Polkehn, P. Eisenbrandt, H. Tamura, and I. Burghardt, Int. J. Quant. Chem. **118**, e25502 (2017).

[67] M. D. Feit, J. A. Fleck, Jr., and A. Steiger, J. Comp. Phys. **47**, 412 (1982).

[68] D. Kosloff and R. Kosloff, J. Comp. Phys. **52**, 35 (1983).

[69] R. Kosloff and D. Kosloff, J. Chem. Phys. **79**, 1823 (1983).

[70] R. Kosloff, J. Phys. Chem. **92**, 2087 (1988).

[71] C. Leforestier, R. H. Bisseling, C. Cerjan, M. D. Feit, R. Friesner, A. Guldberg, A. Hammerich, G. Jolicard, W. Karrlein, H.-D. Meyer, N. Lipkin, O. Roncero, and R. Kosloff, J. Comp. Phys. **94**, 59 (1991).

[72] A. Askar and A. S. Cakmak, J. Chem. Phys. **68**, 2794 (1978).

[73] C. Lanczos, J. Res. Nat. Bur. Stand. **45**, 255 (1950).

[74] T. J. Park and J. C. Light, J. Chem. Phys. **85**, 5870 (1986).

[75] A. I. Kuleff, J. Breidbach, and L. S. Cederbaum, J. Chem. Phys. **123**, 044111 (2005).

[76] H. Tal-Ezer and R. Kosloff, J. Chem. Phys. **81**, 3967 (1984).

[77] A. Luntz and J. Harris, Surf. Sci. **258**, 397 (1991).

[78] M. R. Hand and S. Holloway, J. Chem. Phys. **91**, 7209 (1989).

[79] U. Nielsen, D. Halstead, S. Holloway, and J. K. No/rskov, J. Chem. Phys. **93**, 2879 (1990).

[80] S. Chelkowski, T. Zuo, O. Atabek, and A. D. Bandrauk, Phys. Rev. A **52**, 2977 (1995).

[81] A. D. Bandrauk, S. Chelkowski, P. B. Corkum, J. Manz, and G. L. Yudin, JPB **42**, 134001 (2009).

[82] K.-J. Yuan and A. D. Bandrauk, Struct. Dyn. **2**, 014101 (2015).

[83] V. Vallet, Z. Lan, S. Mahapatra, A. L. Sobolewski, and W. Domcke, J. Chem. Phys. **123**, 144307 (2005).

[84] A. Tehlar and H. J. Wörner, Mol. Phys. **111**, 2057 (2013).

[85] M. Jacon, O. Atabek, and C. Leforestier, J. Chem. Phys. **91**, 1585 (1989).

[86] T. Baumert, V. Engel, C. Meier, and G. Gerber, Chem. Phys. Lett. **200**, 488 (1992).

[87] C. Nicole, M. A. Bouchène, C. Meier, S. Magnier, E. Schreiber, and B. Girard, J. Chem. Phys. **111**, 7857 (1999).

[88] E. Hairer, C. Lubich, and G. Wanner, *Geometric Numerical Integration: Structure-Preserving Algorithms for Ordinary Differential Equations* (Springer Berlin Heidelberg New York, 2006).

[89] C. Lubich, *From Quantum to Classical Molecular Dynamics: Reduced Models and Numerical Analysis*, 12th ed. (European Mathematical Society, Zürich, 2008).

[90] P. R. Halmos, *Finite dimensional vector spaces* (Princeton University Press, 1942).

[91] B. Leimkuhler and S. Reich, *Simulating Hamiltonian Dynamics* (Cambridge University Press, 2004).

[92] J. Auslander, N. Bhatia, and P. Seibert, Bol. Soc. Mat. Mex. **9**, 55 (1964).

[93] N. P. Bhatia and G. P. Szegö, *Dynamical systems: stability theory and applications*, Vol. 35 (Springer, 2006).

[94] G. C. Schatz and M. A. Ratner, *Quantum Mechanics in Chemistry* (Dover Publications, 2002).

[95] Y. Ohtsuki, H. Kono, and Y. Fujimura, J. Chem. Phys. **109**, 9318 (1998).

[96] L. Bomble, A. Chenel, C. Meier, and M. Desouter-Lecomte, J. Chem. Phys. **134**, 204112 (2011).

[97] P. Marquetand, S. Gräfe, D. Scheidel, and V. Engel, J. Chem. Phys. **124**, 054325 (2006).

[98] V. Engel, C. Meier, and D. J. Tannor, Adv. Chem. Phys. **141**, 29 (2009).

[99] P. Marquetand and V. Engel, Chem. Phys. Lett. **426**, 263 (2006).

[100] P. Marquetand and V. Engel, J. Chem. Phys. **127**, 084115 (2007).

[101] S. Vranckx, J. Loreau, N. Vaeck, C. Meier, and M. Desouter-Lecomte, J. Chem. Phys. **143**, 164309 (2015).

[102] M. Yamaki, K. Hoki, Y. Ohtsuki, H. Kono, and Y. Fujimura, J. Am. Chem. Soc. **127**, 7300 (2005).

[103] P. Vindel-Zandbergen, C. Meier, and I. R. Sola, Chem. Phys. **478**, 97 (2016).

[104] S. Choi and J. Vaníček, J. Chem. Phys. **150**, 204112 (2019).

[105] H. F. Trotter, Proc. Amer. Math. Soc. **10**, 545 (1959).

[106] J. Crank and P. Nicolson, Math. Proc. Camb. Phil. Soc. **43**, 50 (1947).

[107] E. A. McCullough, Jr. and R. E. Wyatt, J. Chem. Phys. **54**, 3578 (1971).

[108] W. H. Press, S. A. Teukolsky, W. T. Vetterling, and B. P. Flannery, *Numerical Recipes, The art of scientific computing*, 3rd ed. (Cambridge University Press, 2007).

[109] Y. Saad and M. H. Schultz, SIAM J. Sci. Comp. **7**, 856 (1986).

[110] Y. Saad, *Iterative Methods for Sparse Linear Systems*, 2nd ed. (SIAM, 2003).

[111] G. Strang, SIAM J. Num. Analysis **5**, 506 (1968).

[112] J. Roulet, S. Choi, and J. Vaníček, J. Chem. Phys. **150**, 204113 (2019).

[113] G. A. Worth and L. S. Cederbaum, Annu. Rev. Phys. Chem. **55**, 127 (2004).

[114] W. Domcke and D. R. Yarkony, Annu. Rev. Phys. Chem. **63**, 325 (2012).

[115] C. A. Mead and D. G. Truhlar, J. Chem. Phys. **77**, 6090 (1982).

[116] G. Granucci, M. Persico, and A. Toniolo, J. Chem. Phys. **114**, 10608 (2001).

[117] H. Nakamura and D. G. Truhlar, J. Chem. Phys. **117**, 5576 (2002).

[118] M. Baer, Phys. Rep. **358**, 75 (2002).

[119] H. Köppel, W. Domcke, and L. S. Cederbaum, Adv. Chem. Phys. **57**, 59 (1984).

[120] E. Forest and R. D. Ruth, Physica D **43**, 105 (1990).

[121] M. Suzuki, Phys. Lett. A **146**, 319 (1990).

[122] H. Yoshida, Phys. Lett. A **150**, 262 (1990).

[123] A. D. Bandrauk and H. Shen, Chem. Phys. Lett. **176**, 428 (1991).

[124] A. D. Bandrauk, E. Dehghanian, and H. Lu, Chem. Phys. Lett. **419**, 346 (2006).

[125] T. Prosen and I. Pižorn, J. Phys. A **39**, 5957 (2006).

[126] H. De Raedt, Comput. Phys. Rep. **7**, 1 (1987).

[127] M. Suzuki, Phys. Lett. A **201**, 425 (1995).

[128] S. A. Chin and C. R. Chen, J. Chem. Phys. **117**, 1409 (2002).

[129] R. I. McLachlan, SIAM J. Sci. Comp. **16**, 151 (1995).

[130] M. Wehrle, M. Šulc, and J. Vaníček, Chimia **65**, 334 (2011).

[131] V. Engel and H. Metiu, J. Chem. Phys. **90**, 6116 (1989).

[132] G. Stock, C. Woywod, W. Domcke, T. Swinney, and B. S. Hudson, J. Chem. Phys. **103**, 6851 (1995).

[133] W. Kahan and R.-C. Li, Math. Comput. **66**, 1089 (1997).

[134] M. Creutz and A. Gocksch, Phys. Rev. Lett. **63**, 9 (1989).

[135] M. Sofroniou and G. Spaletta, Optim. Method Softw. **20**, 597 (2005).

[136] M. Frigo and S. G. Johnson, Proc. IEEE **93**, 216 (2005).

[137] G. H. Golub and C. F. Van Loan, *Matrix Computations*, 3rd ed. (The Johns Hopkins University Press, 1996).

[138] R. B. Sidje, ACM Trans. Math. Softw. **24**, 130 (1998).

[139] E. Anderson, Z. Bai, C. Bischof, S. Blackford, J. Demmel, J. Dongarra, J. Du Croz, A. Greenbaum, S. Hammarling, A. McKenney, and D. Sorensen, *LAPACK Users' Guide*, 3rd ed. (Society for Industrial and Applied Mathematics, 1999).

[140] C. Woywod, W. Domcke, A. L. Sobolewski, and H.-J. Werner, J. Chem. Phys. **100**, 1400 (1994).

[141] J. Roulet and J. Vaníček, J. Chem. Phys. **154**, 154106 (2021).

[142] P. A. M. Dirac, Math. Proc. Camb. Phil. Soc. **26**, 376–385 (1930).

[143] J. Frenkel, *Wave mechanics* (Clarendon Press, Oxford, 1934).

[144] J. Broeckhove, L. Lathouwers, E. Kesteloot, and P. V. Leuven, Chem. Phys. Lett. **149**, 547 (1988).

[145] M. Beck, A. Jäckle, G. Worth, and H.-D. Meyer, Phys. Rep. **324**, 1 (2000).

[146] I. Burghardt, K. Giri, and G. A. Worth, J. Chem. Phys. **129**, 174104 (2008).

[147] T. Begušić and J. Vaníček, J. Chem. Phys. **153**, 024105 (2020).

[148] G. A. Hagedorn, Commun. Math. Phys. **71**, 77 (1980).

[149] E. Faou, V. Gradinaru, and C. Lubich, SIAM J. Sci. Comp. **31**, 3027 (2009).

[150] T. Begušić, M. Cordova, and J. Vaníček, J. Chem. Phys. **150**, 154117 (2019).

[151] A. Prlj, T. Begušić, Z. T. Zhang, G. C. Fish, M. Wehrle, T. Zimmermann, S. Choi, J. Roulet, J.-E. Moser, and J. Vaníček, J. Chem. Theory Comput. **16**, 2617 (2020).

[152] M. H. Anderson, J. R. Ensher, M. R. Matthews, C. E. Wieman, and E. A. Cornell, Science **269**, 198 (1995).

[153] F. Dalfovo, S. Giorgini, L. P. Pitaevskii, and S. Stringari, Rev. Mod. Phys. **71**, 463 (1999).

[154] E. P. Gross, Il Nuovo Cimento (1955-1965) **20**, 454–477 (1961).

[155] L. P. Pitaevskii, Sov. Phys. JETP **13**, 451 (1961).

[156] R. Carles, Ann. Henri Poincaré **3**, 757 (2002).

[157] R. Carles, P. A. Markowich, and C. Sparber, Nonlinearity **21**, 2569 (2008).

[158] A. Minguzzi, S. Succi, F. Toschi, M. Tosi, and P. Vignolo, Phys. Rep. **395**, 223 (2004).

[159] W. Bao, D. Jaksch, and P. A. Markowich, J. Comp. Phys. **187**, 318 (2003).

[160] Q. Chang, E. Jia, and W. Sun, J. Comp. Phys. **148**, 397 (1999).

[161] X. Antoine, W. Bao, and C. Besse, Comp. Phys. Comm. **184**, 2621 (2013).

[162] S. Hahn and G. Stock, J. Phys. Chem. B **104**, 1146 (2000).

[163] W. H. Press, S. A. Teukolsky, W. T. Vetterling, and B. P. Flannery, *Numerical recipes in C* (Cambridge University Press, Cambridge, UK, 1992).

[164] W. E. Arnoldi, Quart. Appl. Math **9**, 17 (1951).

[165] Y. Saad, Linear Algebra Appl. **34**, 269 (1980).

[166] K. B. Petersen and M. S. Pedersen, "The matrix cookbook," (2012).

[167] J. Roulet and J. Vaníček, The Journal of Chemical Physics **154**, 154106 (2021).

[168] R. De Vogelaere, "Methods of integration which preserve the contact transformation property of the hamilton equations," (1956), Report No. 4, Department of Mathematics, University of Notre Dame.

[169] E. Hairer, C. Lubich, and G. Wanner, Acta Numerica **12**, 399 (2003).

[170] C. Lubich, Math. Comput. **77**, 2141 (2008).

[171] M. Thalhammer, SIAM J. Num. Analysis **50**, 3231 (2012).

[172] M. Beck and H.-D. Meyer, Z. Phys. D **42**, 113 (1997).

[173] M. Beck, A. Jäckle, G. Worth, and H.-D. Meyer, Phys. Rep. **324**, 1 (2000).

[174] P. R. Halmos, *Introduction to Hilbert space and the theory of spectral multiplicity* (Chelsea, 1951).

Julien Roulet

Rte de Saint-Cergue 54 – 1260 – Nyon
☎ +41 79 850 27 74 • ✉ julien.roulet@epfl.ch
🖱 orcid.org/0000-0001-5539-0032 • in julien-roulet

Graduate student in Theoretical Chemistry at the Laboratory of Theoretical Physical Chemistry. Passionate about physics, chemistry, and data science.

Education

○ **Ecole Polytechnique Fédérale de Lausanne (EPFL)** — **Lausanne**
Ph.D. in Theoretical Chemistry — *2017–*

- Nonadiabatic quantum dynamics, quantum control and calculation of spectra
- Leading students in various computational chemistry projects in the field of nonadiabatic quantum dynamics
- Principal teaching assistant for numerical methods in chemistry and chemical kinetics courses
- Involved in the correction and grading of exams

○ **Ecole Polytechnique Fédérale de Lausanne (EPFL)** — **Lausanne**
M.Sc. in Molecular and Biological Chemistry — *2015–2017*

- Physical chemistry
- Computational chemistry
- Biological chemistry and biophysics

○ **Ecole Polytechnique Fédérale de Lausanne (EPFL)** — **Lausanne**
B.Sc. in Chemistry and Chemical Engineering — *2011–2014*

- Biotechnology
- Computational chemistry
- Biological chemistry and biophysics

○ **Gymnase Auguste Piccard** — **Lausanne**
Federal maturity in Biology and Chemistry — *2008–2011*

Publications

[1] Tomislav Begušić, Julien Roulet, and Jiří Vaníček. On-the-fly ab initio semiclassical evaluation of time-resolved electronic spectra. *The Journal of Chemical Physics*, 149(24):244115, 2018.

[2] Julien Roulet, Seonghoon Choi, and Jiří Vaníček. Efficient geometric integrators for nonadiabatic quantum dynamics. II. The diabatic representation. *The Journal of Chemical Physics*, 150(20):204113, 2019.

[3] Antonio Prlj, Tomislav Begušić, Zhan Tong Zhang, George Cameron Fish, Marius Wehrle, Tomáš Zimmermann, Seonghoon Choi, Julien Roulet, Jacques-Edouard

Moser, and Jiří Vaníček. Semiclassical Approach to Photophysics Beyond Kasha's Rule and Vibronic Spectroscopy Beyond the Condon Approximation. The Case of Azulene. *Journal of Chemical Theory and Computation*, 16(4):2617–2626, 2020.

[4] Julien Roulet and Jiří Vaníček. Time-reversible and norm-conserving high-order integrators for the nonlinear time-dependent schrödinger equation: Application to local control theory. *The Journal of Chemical Physics*, 154(15):154106, 2021.

[5] Julien Roulet and Jiří Vaníček. An implicit split-operator algorithm for the nonlinear time-dependent schrödinger equation. *The Journal of Chemical Physics*, 155(20):204109, 2021.

Experience

- **Ecole Polytechnique Fédérale de Lausanne (EPFL)** **Lausanne**
  Intern at the Laboratory of Theoretical Physical Chemistry, Lausanne *August 2016*

  I developed a Fortran program for interpolating short laser pulses.
- **Swiss Armed Forces** **Aarau/Birmensdorf**
  Infantryman *2014–2015*

  I fully completed my military duty as a soldier in the infantry.
- **Ecole Polytechnique Fédérale de Lausanne (EPFL)** **Lausanne**
  Teaching assistant *2012–2014*

  Assistant in general chemistry, programming, and general physics courses for microengineering, physics, chemistry and electrical engineering students during several semesters.

Technical and personal skills

- **Programming Languages:** C, Fortran, Matlab, Mathematica, LaTeX, Python, Bash.
- **Software Skills:** MS Office suite, Amber, Gaussian, GAMESS, Gnuplot, Vi.
- **Languages:** French, English (C1), German (B2).

Interests and extra-curricular activity

- Running, hiking and sports in general.